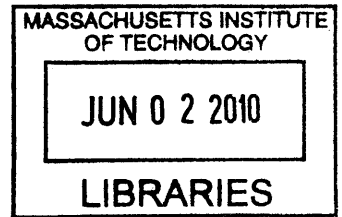


Semiconductor Nanocrystals: Synthesis, Mechanisms of Formation, and Applications in Biology

by

Peter M. Allen

B.S. Chemistry
University of California Santa Barbara, 2006



Submitted to the Department of Chemistry
in Partial Fulfillment of the Requirements for the Degree of

Doctor of Philosophy

ARCHIVES

at the

MASSACHUSETTS INSTITUTE OF TECHNOLOGY

April 29, 2010

[June 2010]

© Massachusetts Institute of Technology, All Rights Reserved

Author _____

Handwritten signature of Peter M. Allen in black ink.

Department of Chemistry
April 29, 2010

Certified by _____

Handwritten signature of Mouni G. Bawendi in black ink.

Mouni G. Bawendi
Professor of Chemistry
Thesis Supervisor

Accepted by _____

Handwritten signature of Robert W. Field in black ink.


Robert W. Field
Chairman, Department Committee of Graduate Students

This doctoral thesis has been examined by a committee of the Department of Chemistry as follows:



Professor Daniel G. Nocera
Thesis Chairman

Professor Mounji G. Bawendi
Thesis Supervisor



Professor Christopher C. Cummins
Thesis Committee Member

Semiconductor Nanocrystals: Synthesis, Mechanisms of Formation, and Applications in Biology

by

Peter M. Allen

Submitted to the Department of Chemistry
on April 29, 2010 in Partial Fulfillment of the
Requirements for the Degree of
Doctor of Philosophy

Abstract

The primary focus of this thesis is the synthesis and applications of semiconductor nanocrystals, or quantum dots (QDs). Novel synthetic routes to ternary I-III-VI QDs are presented, and we report the first highly luminescent Cu-In-Se QDs spanning the red to near-infrared region. The synthetic method is modular and is extended to Ag-In-Se, Cu-In-Zn-S, and Ag-In-Zn-S QDs, luminescent from the blue to near-infrared. The development of new core-shell InAs(ZnCdS) QDs is discussed in the context of making highly fluorescent, stable biological probes in the near-infrared region. Applications in biological systems from cellular labeling to sentinel lymph node mapping are demonstrated. In addition, we present new methods for doping InAs QDs in order to control carrier type through the introduction of acceptor defects such as cadmium. The synthesis and characterization of n and p type InAs QDs is discussed.

In order to understand the differences in size distributions with current III-V QD synthetic procedures and II-VI and IV-VI QD syntheses we have explored the molecular mechanisms that lead to the formation of InP and InAs QDs. We find that current III-V QD syntheses result in the depletion of molecular precursors immediately following nucleation, preventing growth from molecular precursors, thus failing to meet the a key criterion for a monodisperse colloidal synthesis in the Dinegar and LaMer model. In the conclusion of this thesis, we explore the electrically controlled solution-liquid-solid (EC-SLS) synthesis of InP nanowires. Using the EC-SLS method, we are able to controllably place n type InP nanowires into field effect transistor geometries.

Thesis Supervisor: Mounji G. Bawendi
Title: Lester Wolfe Professor of Chemistry

Preface

Parts of this thesis have appeared in previously published manuscripts. Copyright approval has been obtained for any reproduced figures or text as indicated below.

Chapter 2

Reproduced with permission from *Journal of the American Chemical Society*, **2008**, 130, 9240-9241. Copyright 2008 American Chemical Society.

Chapter 3

Reproduced with permission from *Journal of the American Chemical Society*, **2010**, 132, 470-471. Copyright 2009 American Chemical Society.

Chapter 5

P.M. Allen, B.J. Walker, and M.G. Bawendi, "Mechanistic Insights into the Formation of InP Quantum Dots" *Angewandte Chemie International Edition*, **2010**, 49, 760-762. Copyright Wiley-VCH Verlag GmbH & Co. Reproduced with permission.

Chapter 6

Reproduced with permission from *ACS Nano*, **2009**, 3, 3260-3265. Copyright 2009 American Chemical Society.

Table of Contents

Chapter 1. Introduction to Semiconductor Nanocrystals	16
1.1 Colloidal Semiconductor Nanocrystals, or Quantum Dots	17
1.2 Historical Perspectives on Quantum Dot Synthesis	18
1.3 Monodisperse Quantum Dots.....	21
1.3.1 Synthesis of Colloidal Quantum Dots.....	21
1.3.2 Physics of Finite Semiconductors.....	23
1.3.3 Optical Properties of Quantum Dots.....	25
1.3.4 Quantum Dot Core-Shell Structures	26
1.4 Applications of Quantum Dots	28
1.4.1 Quantum Dots in Biology.....	28
1.5 Thesis Overview	29
1.6 References.....	32
Chapter 2. Ternary I-III-VI Quantum Dots.....	37
2.1 Introduction.....	37
2.2 Cu-In-Se Quantum Dots.....	39
2.2.1 Synthesis.....	39
2.2.2 Elemental Composition and TEM	41
2.2.3 Wide Angle X-Ray Scattering	43
2.2.4 Temperature Dependent Photoluminescence.....	45
2.3 AgInSe ₂ Quantum Dots.....	47
2.3.1 Synthesis.....	47
2.3.2 Characterization.....	47
2.4 Cu-In-Zn-S and Ag-In-Zn-S Quantum Dots	49
2.5 Conclusions.....	51
2.6 Procedures.....	52
2.7 References.....	55
Chapter 3. InAs(ZnCdS) Quantum Dots for Biological Imaging in the Near-Infrared....	58
3.1 Introduction.....	58
3.2 InAs(ZnCdS) Quantum Dots	60
3.2.1 Synthesis.....	60
3.2.2 Ligand Exchange	62

3.2.3	Characterization.....	64
3.3	Biological Imaging.....	66
3.3.1	Cellular Labeling.....	66
3.3.2	Multi-photon Biological Imaging.....	68
3.4	Conclusions.....	70
3.5	Procedures.....	71
3.6	References.....	76
Chapter 4.	Control of Carrier Type in InAs Quantum Dots	79
4.1	Introduction.....	79
4.2	Cd Doped InAs Quantum Dots	83
4.2.1	Synthesis of InAs QDs.....	83
4.2.2	Synthesis of Cd:InAs QDs.....	85
4.2.3	Optical Properties	85
4.2.4	Field Effect Transistors.....	87
4.3	p-n Hetero-junction Quantum Dot Device.....	89
4.4	Implications for Quantum Dot Devices	91
4.5	Methods.....	92
4.6	References.....	93
Chapter 5.	Mechanistic Insights into the Formation of InP Quantum Dots	96
5.1	Introduction.....	96
5.2	Mechanistic Studies	98
5.2.1	Proposed Mechanism.....	98
5.2.2	¹ H NMR Studies for Literature Reports.....	98
5.2.3	¹ H NMR Molecular Precursor Evolution.....	100
5.2.4	Eyring Analysis	104
5.2.5	Kinetic Analysis.....	106
5.3	Implications for III-V synthetic developments	106
5.4	Procedures.....	108
5.5	References.....	110
Chapter 6.	Electrically Controlling and Monitoring InP Nanowire Growth.....	113
6.1	Introduction.....	113
6.2	InP Nanowires.....	115
6.2.1	Experimental Setup.....	115
6.2.2	Characterization of InP Nanowires.....	117

6.2.3	Monitoring of InP Nanowire Growth	119
6.2.4	Field Effect Transistors.....	123
6.3	Conclusions.....	125
6.4	Procedures.....	126
6.5	References.....	127

Figure Captions

Figure 1-1. Schematic of a colloidal quantum dot.	18
Figure 1-2. Typical reaction setup for the synthesis of colloidal quantum dots.	21
Figure 1-3. Reaction coordinate of a monodisperse colloidal quantum dot synthesis.	23
Figure 1-4. Band structures of bulk and finite semiconductors.	25
Figure 1-5. Ensemble absorption spectra of (left) CdSe QDs ^[17] and (right) InP QDs. ^[42]	26
Figure 1-6. Schematic of core-shell quantum dots.....	28
Figure 1-7. Ligand exchange of QDs with a poly(amino-PEG)-PIL polymer.....	29
Figure 2-1. Binary and ternary semiconductor band gaps.	36
Figure 2-2. Absorbance and PL of Cu-In-Se QDs.....	38
Figure 2-3. PL series and TEM of Cu-In-Se QDs.....	38
Figure 2-4. Graph showing the ratio of In/Cu precursors in growth solution.....	39
Figure 2-5. TEM and corresponding histograms of Cu-In-Se QDs:.....	40
Figure 2-6. WAXS of Cu-In-Se QDs.....	42
Figure 2-7. Predicted stoichiometries of “ordered defect compounds” (ODC).....	42
Figure 2-8. Temperature dependent PL of Cu-In-Se QDs.	44
Figure 2-9. Absorbance and PL of AgInSe ₂ QDs.	46
Figure 2-10. WAXS of 3 nm and 6 nm AgInSe ₂ QDs.	46
Figure 2-11. Emission spectra of Cu-In-Zn-S QDs and Ag-In-Zn-S QDs.....	48
Figure 3-2. Absorbance and PL of InAs(ZnCdS) QDs.....	59
Figure 3-3. Quantum Yields during InAs(ZnCdS) shell growth.....	59
Figure 3-4. Schematic of ligand exchange.....	61
Figure 3-5. Absorbance and PL of InAs(Zn _{0.7} Cd _{0.3} S) QDs.	61
Figure 3-6. TEM and GFC of poly(PEG12)-PIL InAs(ZnCdS) QDs.	63
Figure 3-7. WDS and TEM of InAs(ZnCdS) QDs.	63
Figure 3-8. Cellular labeling.....	65
Figure 3-9. In vivo vasculature imaging.....	67
Figure 4-1. Schematic for donor and acceptor doping.....	78
Figure 4-2. TEM of 4 nm InAs QDs.....	80
Figure 4-3. Growth of InAs QDs with multiple injections from InCl ₃ and (Me ₃ Si) ₃ As.	82
Figure 4-4. Growth of InAs QDs with multiple injections from In(MA) ₃ and (Me ₃ Si) ₃ As.....	82
Figure 4-5. Schematic for doping InAs QDs with Cd.....	84
Figure 4-6. Absorbance spectra of InAs QDs with Cd(OA) ₂ as a function of temperature.....	84

Figure 4-8. InAs (Orange) and PbS (Green) heterostructure device.....	88
Figure 5-1. Proposed mechanistic pathway for amine-inhibited InP synthesis	95
Figure 5-2. ¹ H NMR spectra	97
Figure 5-3. Time-resolved ¹ H NMR spectra at 40 °C	99
Figure 5-4. ¹ H-decoupled ³¹ P spectrum for the InP reaction mixture after 30 min at 25 °C.	101
Figure 5-5. ¹ H NMR concentration of complex 2 during synthesis at 40 °C.	101
Figure 5-6. Eyring plot for amine-based synthesis of colloidal InP QDs.	103
Figure 5-7. ¹ H NMR integration of all identifiable TMS-containing species.	105
Figure 5-8. Evolution of TMS-MA concentration vs. time	105
Figure 6-1. Solution-liquid-solid synthesis of InP nanowires.....	112
Figure 6-2. Experimental Setup.	112
Figure 6-3. InP nanowire growth as a function of bias voltage.	116
Figure 6-4. InP nanowire characterization.	117
Figure 6-5. Current sensing across the electrode gap during the InP nanowire growth.	118
Figure 6-6. Conductivity as a function of bias voltage during growth.	120
Figure 6-7. InP nanowire mats grown in a field effect transistor geometry.....	123

Chapter 1. Introduction to Semiconductor Nanocrystals

The synthesis of colloidal quantum dots (QDs) is an elegant interplay between molecular inorganic chemistry and solid state semiconductor materials chemistry. The use of solution based synthetic chemistry to manipulate small inorganic crystals is a powerful approach in the control of size, shape, and composition of nano-structures in a ‘bottom up’ fashion. Colloidal growth of nano-structures has produced nanocrystals, nanorods, cubes, prisms, and composed of metals, oxides, and semiconductors.^[1-3] As a result, colloidal semiconductor nanocrystals have grown into a scientific field of study spanning chemistry, physics, biology, and engineering, with applications ranging from light emitting diodes, biological imaging agents, photovoltaics, and photo detectors.^[4-6] However, significant challenges remain in the synthesis of colloidal QDs composed of group III-V and I-III-VI semiconductors. In this thesis, we will explore the molecular mechanisms of current III-V QD syntheses, and explore new synthetic routes to highly functional III-V and I-III-VI QD materials.^[7-9]

Traditionally, the fabrication of semiconductor materials utilizes single crystal growth substrates and ultra high vacuum (UHV) conditions. These methods can be used for the growth of epitaxial quantum dots, through the Stranski-Krastanov method, but the resulting material is trapped within a solid state matrix.^[10-13] Our ability to move from UHV conditions to solution in the synthesis of high quality semiconductor nanocrystals is due to the small crystalline size and high surface area inherent to nanocrystals. As a result, impurities migrate to the QD surface producing nearly defect free semiconductor crystals, grown in relatively impure conditions when compared to traditional semiconductor processing methods.^[14-16] Thus, we are able to operate in a unique crystalline size range well suited for the solution based synthesis of nanocrystals.^[17]

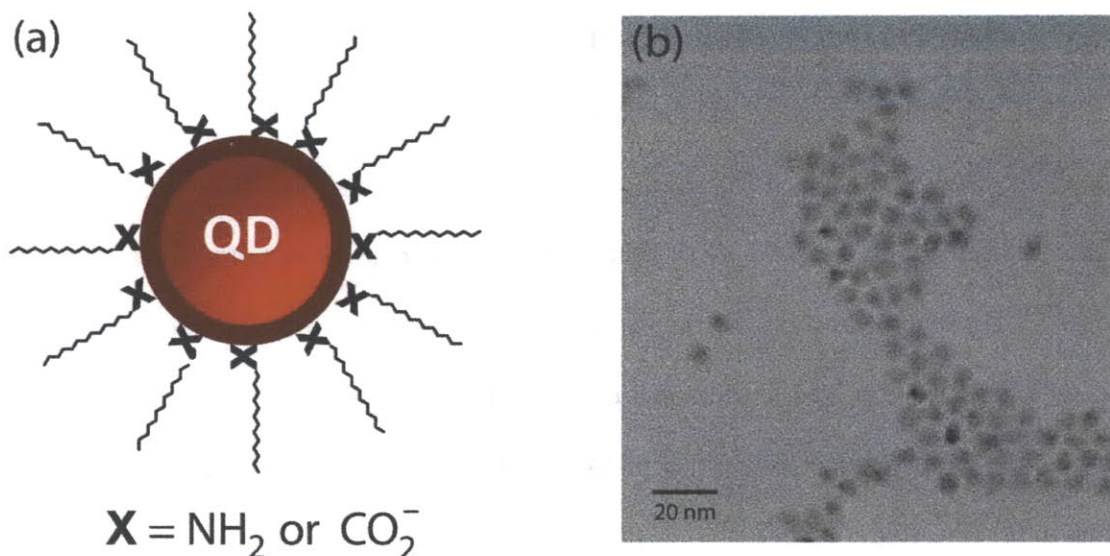


Figure 1-1. Schematic of a colloidal quantum dot. (a) Capping ligands can be varied, in this schematic the use of carboxylate and primary amines are depicted. (b) Transmission electron microscopy of CdSe(ZnCdS) QDs.

1.1 Colloidal Semiconductor Nanocrystals, or Quantum Dots

Colloidal QDs are composed of a small inorganic semiconductor core (1-10 nm) and are coated with a layer of organic passivating ligands (Figure 1-1). As grown, the QDs are typically soluble in non-polar organic solvents, and post-synthetic surface modifications can allow for the transfer of QDs into the water phase or onto solid state substrates. The science and engineering of colloidal QDs is driven by advances in the synthesis of QDs, as an increasing degree of control over shape, size, and composition has enabled a wide range of fundamental studies and applications of QD materials. Currently, the material of choice for visible applications are II-VI CdSe QDs and for infrared applications the IV-VI lead chalcogenide QDs dominate. The exploration of synthetic routes to colloidal QDs composed of different semiconductor materials offers the potential for the discovery of new properties and applications of QD materials.

1.2 Historical Perspectives on Quantum Dot Synthesis

The inclusion of nano to micron sized semiconductor materials into glasses has been explored since the 1930s, when Rocksby observed that the inclusion of CdSe in glass matrices changes the hue of glasses and these materials have been used as color filters for several decades.^[18] However, it was not until the 1980s that the size dependent behavior of semiconductors was observed in semiconductor embedded glasses. Ekimov and coworkers first observed the size dependent properties of ionic nanocrystals, in a glass matrix, at the Loffe Institute in St. Petersburg, Russia.^[19-21]

In 1939, at the University of Sofia, Stranski and Krastanov (SK) developed crystal growth models for the formation of 3-D islands when epitaxial crystals are grown on lattice strained heterogeneous substrates.^[10, 11] The work by Stranski and Krastanov formed the basis for SK grown quantum dots, however exploiting SK growth for uniform quantum dot materials remained a significant challenge for decades following their crystal growth observations. Success has been primarily found in SK grown InAs, GaAs, and AlGaAs.^[22-24] SK grown quantum dots are fundamentally limited by the selection of appropriately lattice mismatched semiconductor materials and the resulting material is trapped within a solid matrix.^[25]

The discovery of size dependent behavior in *colloidal* CdS nanocrystals was first observed by Louis Brus in 1983, through the measurement of size dependent redox potentials.^[26] This discovery was termed ‘accidental’ by Brus, as his motivation for using colloidal particles was to simply enhance the surface area of semiconductors in order to observe redox reactions of organic molecules at photoexcited semiconductor surfaces.^[27] The use of wet chemical routes to fabricate semiconductors, in this case colloidal quantum dots, was met with skepticism by some condensed matter physicists. Indeed, at Bell Labs in the 1980s some physicists claimed that

“colloidal particle research was a waste of time, the quality of semiconductor material that could be produced in a flask could never rival what was produced in a vacuum chamber.”^[28]

Synthetic routes to CdSe QDs using organometallic reagents were pioneered by Michael Steigerwald at Bell labs later in the 1980s. The CdSe QDs were initially grown in inverse micelles at low temperatures with moderate size distributions.^[29] The introduction of high boiling point coordinating solvents occurred in 1989 utilizing a mixture of tributyl phosphine (TBP) and tributyl phosphine oxide (TBPO).^[30] Initially, pure TBP was found to produce relatively monodisperse CdSe nanocrystals upon annealing of CdSe clusters, however these results could not be reproduced with different TBP batches. Upon analysis by ³¹P NMR, the batch of ‘pure’ TBP had significantly oxidized to TBPO. As a result, mixtures of TBP and TBPO became the surfactant of choice for QD growth in the late 1980s and early 1990s.

From 1990 onwards, Chris Murray, David Norris, and Mounji Bawendi pursued the synthesis of CdSe QDs with narrow size distributions at MIT. A decision to move from a TBP and TBPO mixture to trioctylphosphine (TOP) and trioctylphosphine oxide (TOPO) was made out of budgetary considerations, as TOP and TOPO were cheaper reagents. Fortunately, the higher boiling points of TOP and TOPO proved to be extremely advantageous in the synthesis of highly crystalline QDs. Inspired by the use of Me₃P chalcogenide sources in bulk semiconductor growth, TOPSe was utilized as the selenium source for colloidal CdSe synthesis. The organometallic reagent dimethyl cadmium was introduced as a reactive cadmium source, as earlier synthetic routes were limited by the formation of small semiconductor clusters. This research effort culminated in 1993 with the publication of a synthetic method for CdSe nanocrystals ranging from 2-10 nm in diameter with narrow size distributions (Figure 1-2).^[17] This synthetic achievement has enabled the widespread study and application of colloidal QDs.

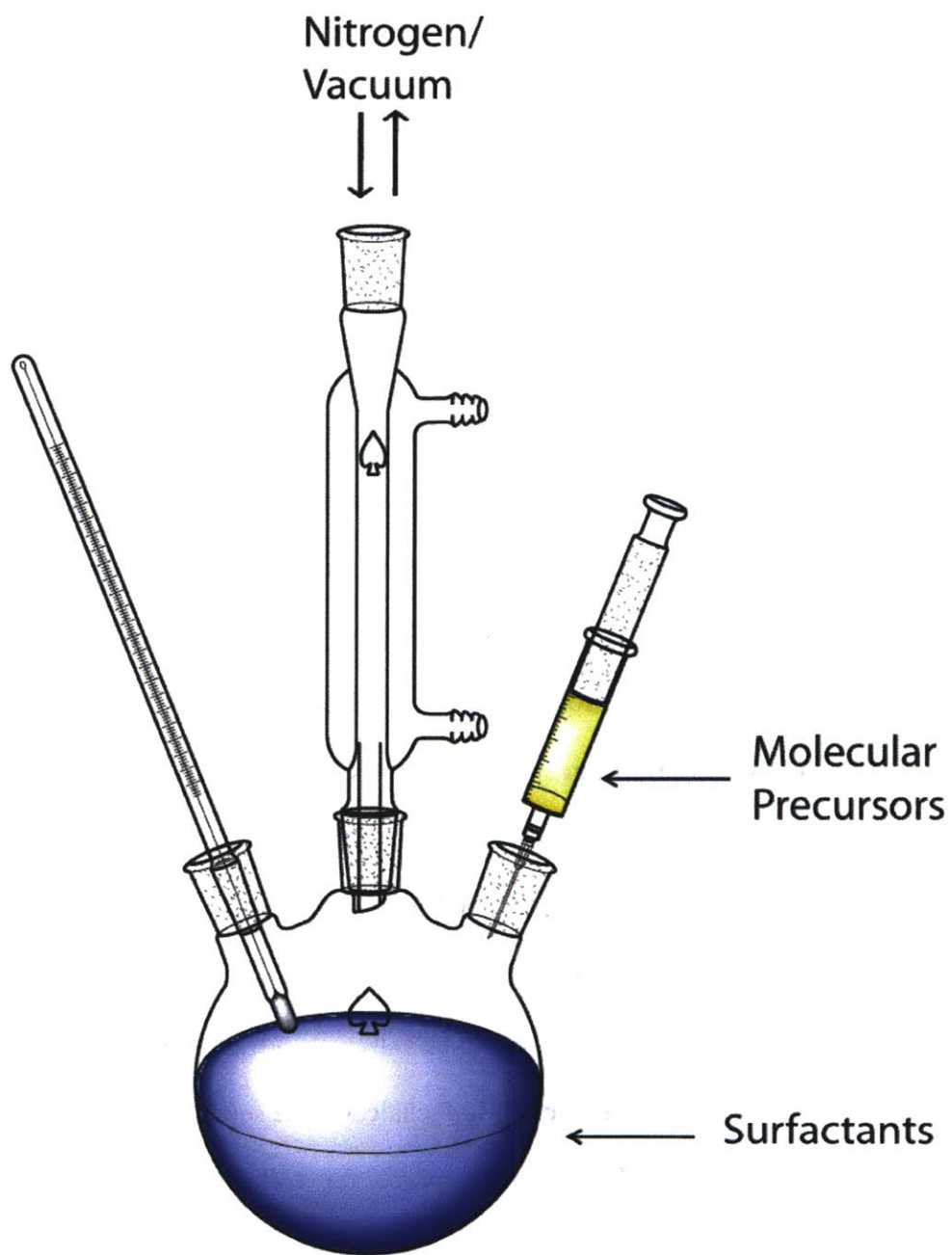


Figure 1-2. Typical reaction setup for the synthesis of colloidal quantum dots.

1.3 Monodisperse Quantum Dots

1.3.1 Synthesis of Colloidal Quantum Dots

The development of solution based syntheses for colloidal quantum dots has been largely inspired by work done on sulfur colloids by Dinegar and Lamer.^[31] In a simplified view of the synthesis of monodisperse colloids, two general events should occur: (1) the nucleation of colloids followed by (2) growth of these nuclei from molecular precursors (Figure 1-3). The controllable nucleation and growth of narrow size distribution QDs was first demonstrated 1993.^[17] However, the synthesis was largely treated as a ‘black box’ and an understanding of the molecular mechanisms involved in the formation of monodisperse CdSe QDs was not thoroughly probed for over well over a decade following the 1993 CdSe synthetic breakthrough. Mechanistic investigations in 2006 and 2007 by ³¹P NMR confirmed that the reaction coordinate depicted in Figure 1-3 was in fact fulfilled for the synthesis of CdSe and PbSe QDs.^[32, 33]

A considerable amount of progress in the controllable synthesis and mechanistic understanding of II-VI and IV-VI QDs has driven the field of colloidal semiconductor nanocrystals for the past two decades. However, serious challenges remain in extending the synthesis of monodisperse QDs to III-V semiconductors, or to more complex ternary formulations such as I-III-VI semiconductors.^[34, 35] A molecular understanding of III-V QD synthesis had remained unexplored in the colloidal QD community, and Chapter 5 seeks to understand the current challenges in the synthesis of III-V QDs. We have found that the reaction coordinate depicted in Figure 1-3 is not currently met for III-V syntheses, due to depletion of molecular precursors following nucleation, indicating that new synthetic routes to III-V QDs must be developed in order to produce narrow size distributions of III-V QDs.

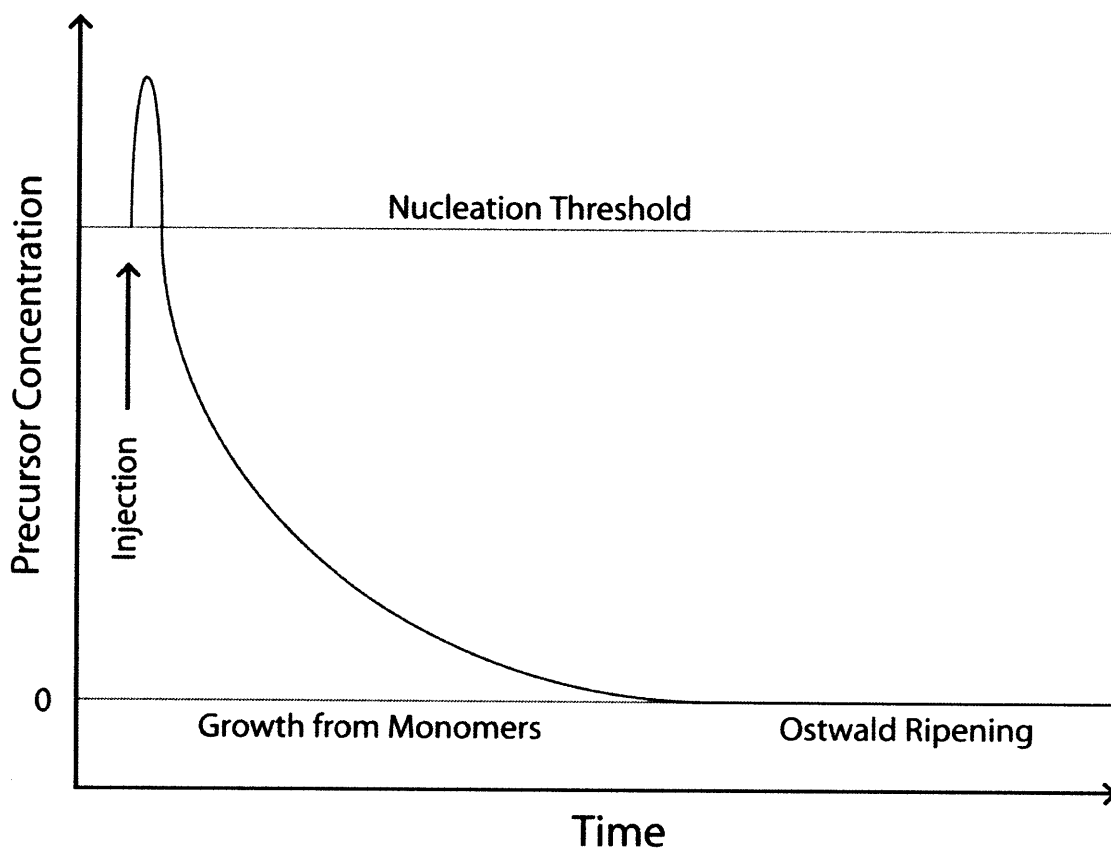


Figure 1-3. Reaction coordinate of a monodisperse colloidal quantum dot synthesis.

1.3.2 Physics of Finite Semiconductors

Quantum dots are particularly interesting as they enable the study of semiconductors on small length scales. In a direct-gap bulk semiconductor, a photon of energy greater than the bandgap promotes an electron to the conduction band, creating an electron hole pair (Figure 1-4.a).^[36] However, if the semiconductor becomes finite in size, approaching the natural length scale of its electron hole pair, the quantization of energy states is observed (Figure 1-4.b). The transition from a continuum of states in a bulk semiconductor, to discrete states in a finite semiconductor, can be understood as the result of a decrease in the density of states due to the finite number of repeating unit cells in three dimensions. As a result, the optical properties of a finite semiconductor material differ significantly from a bulk semiconductor material. The observed size dependent properties arise from confinement of the carriers in a 3-D potential well.

The natural length of an electron hole pair in a semiconductor is often referred to as the Bohr exciton radius, which is inversely related to the effective mass of the carriers. As a result, nanocrystals composed of different semiconductors exhibit different degrees of quantum confinement. Narrow bandgap semiconductors have light carriers, such as InAs which has a large Bohr radius of 36 nm and the optical properties of InAs can be tuned from the visible to mid-infrared. Wider bandgap semiconductors have heavier carriers, such as CdSe which has a Bohr exciton radius of 6 nm and can be tuned in the visible region. The above discussion of how to predict the degree of quantum confinement in a semiconductor nanocrystal is based on the effective masses of the carriers in the bulk material and is the effective mass approximation.^[37] Extensive experimental and theoretical work has been completed to understand the underlying physics of confinement in CdSe QDs, however a similarly detailed analysis of the electronic structure of other QDs, such as InP, have been limited by sample quality.^[38, 39]

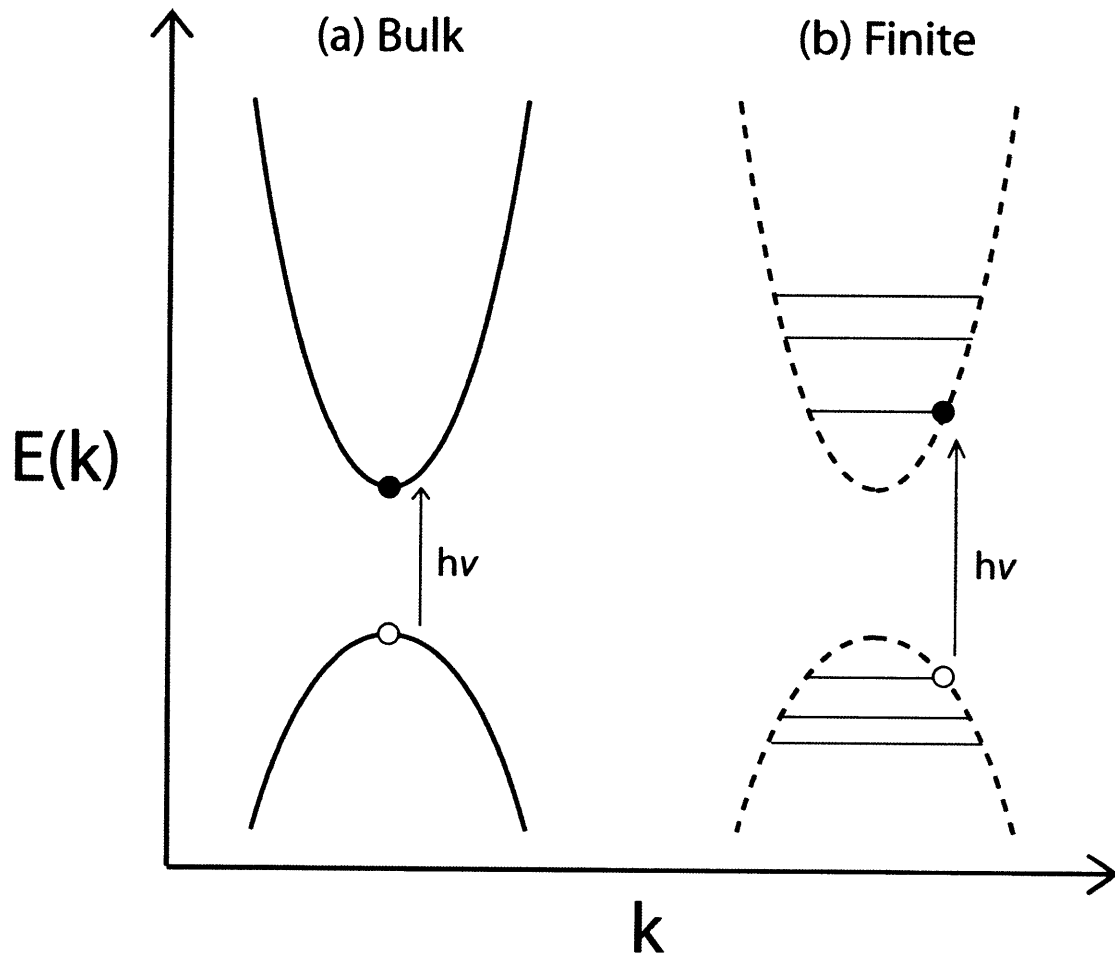


Figure 1-4. Band structures of bulk and finite semiconductors. (a) Continuum of states in a bulk direct-gap band structure and (b) discrete states appear in crystals of a finite size due to the quantization of states.

1.3.3 Optical Properties of Quantum Dots

Quantum dots are characterized by a continuous absorption to the blue of the band edge, and narrow tunable emission at the band edge. The ability to observe discrete ‘molecular-like’ transitions and narrow band edge emission in an ensemble of QDs is the result of extremely narrow size distributions attained in the synthesis of chalcogenide based QDs. The synthesis of QDs with narrow size distributions is essential for the exploitation of QD optical properties, from basic spectroscopy to applications in LEDs and biology.^[40, 41]

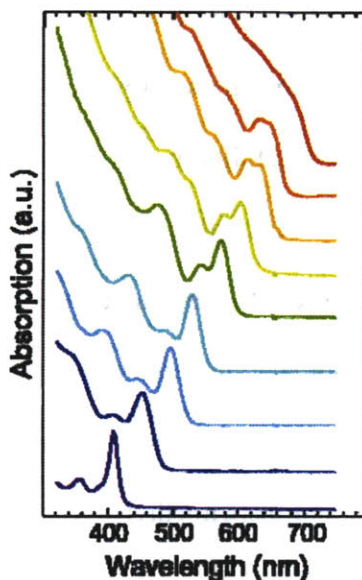


Figure 1-5. Ensemble absorption spectra of CdSe QDs (Chris Murray, MIT Thesis, 1995).

As discussed in previous sections, quantum confinement of nanocrystals creates discrete electronic transitions. The positions of these transitions depend strongly on particle size, and as a result the ensemble absorption features depend strongly on particle size distributions. In Figure 1-5 the discrete transitions can be easily observed in an ensemble of CdSe QDs with narrow size distributions.^[42] In the case of InP nanocrystals, only broad absorption features near the band edge can be resolved due to relatively broad size distributions in the ensemble measurements.^[43]

1.3.4 Quantum Dot Core-Shell Structures

In order to increase the photo-stability and quantum yields of QDs, a wider bandgap material is typically grown over the core material.^[44-51] The shell material serves to isolate the exciton from non-radiative relaxation via surface states. The development of core-shell QDs has enabled the applications of QDs in light emitting applications, with particular success in biological imaging and LEDs.^[52, 53]

Synthetic considerations in the design of core-shell materials include lattice parameters and band gap offsets to create Type I or Type II materials (Figure 1-6.a) Reduction of lattice mismatch between core and shell materials provides robust QDs amenable to surface modifications.^[54] In order to enable stability under ambient conditions, shell materials are primarily composed of sulfide based materials. In addition, band gap offsets can be used to control the degree of confinement in order to tune radiative wavelengths and lifetimes.^[55-57]

The growth of a semiconductor shell material over a QD core (Figure 1-6.b) is commonly achieved by two synthetic routes. The simultaneous addition of highly reactive precursors, such as diethyl zinc, dimethyl cadmium, and bis(trimethylsilyl) sulfide to a solution containing CdSe cores was developed in the mid 1990s.^[44, 46, 51] These syntheses are conducted at lower temperatures than QD core growth, in order to prevent the nucleation of CdS or ZnS QDs. An alternative method is inspired by atomic layer deposition, and utilizes less reactive reagents such as cadmium or zinc carboxylates and elemental sulfur. This method was termed ‘successive ion layer adsorption and reaction’ (SILAR).^[45, 47] The SILAR method utilizes the alternating injection of precursors followed by a high temperature annealing step. This synthetic route has been used to produce thick shell CdSe(CdS) QDs, which exhibit suppressed blinking characteristics.^[58, 59]

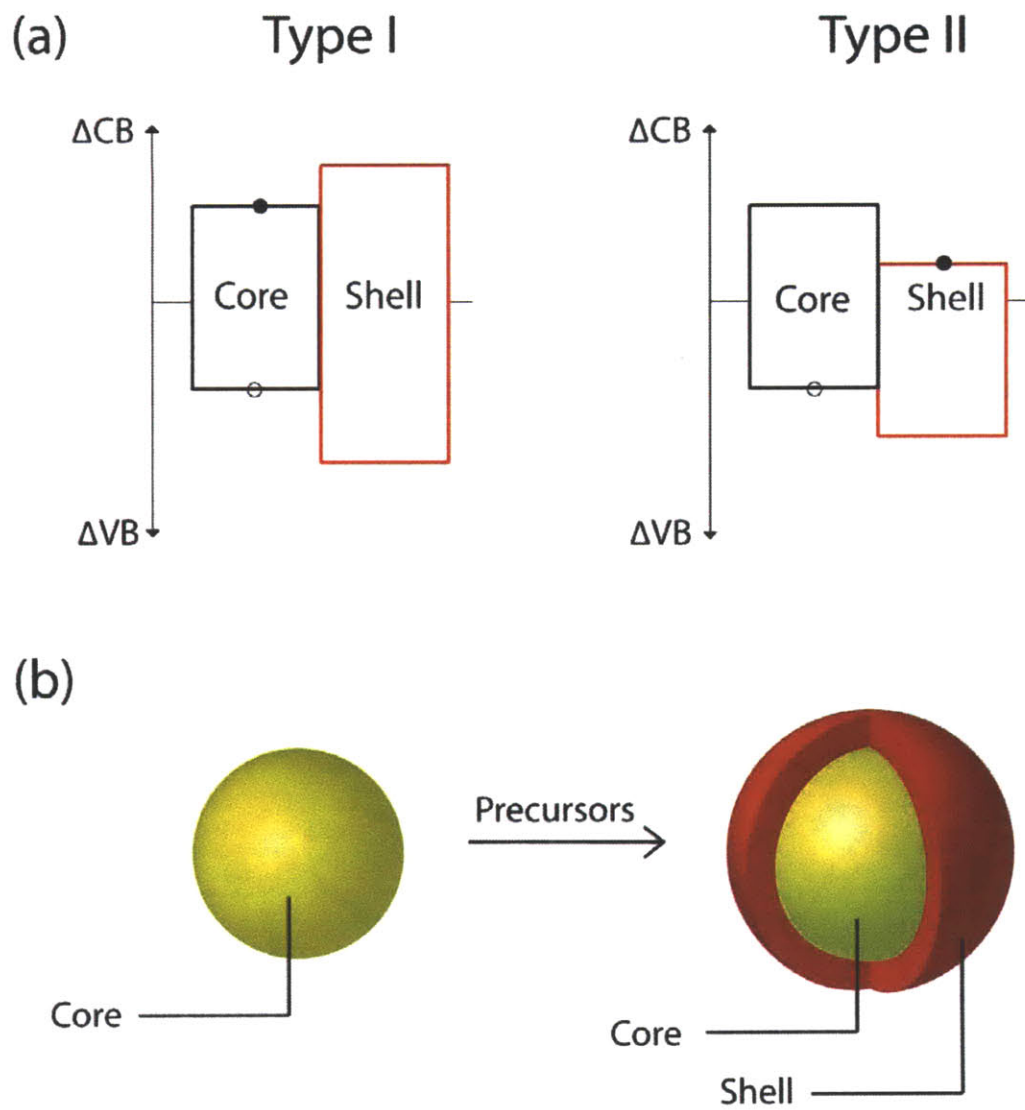


Figure 1-6. Schematic of core-shell quantum dots. (a) Band offsets for Type I and Type II core-shell materials. (b) schematic of core-shell growth.

1.4 Applications of Quantum Dots

1.4.1 Quantum Dots in Biology

The optical properties of QDs make them particularly well suited for use as luminescent biological probes. The large two-photon absorption cross section of QDs make them attractive for multi-photon microscopy.^[41, 60] In addition, the ability to develop bright probes emissive in the near-infrared (NIR) region is exceedingly interesting for in vivo biological imaging, such as sentinel lymph node mapping or tumor targeting.^[61, 62]

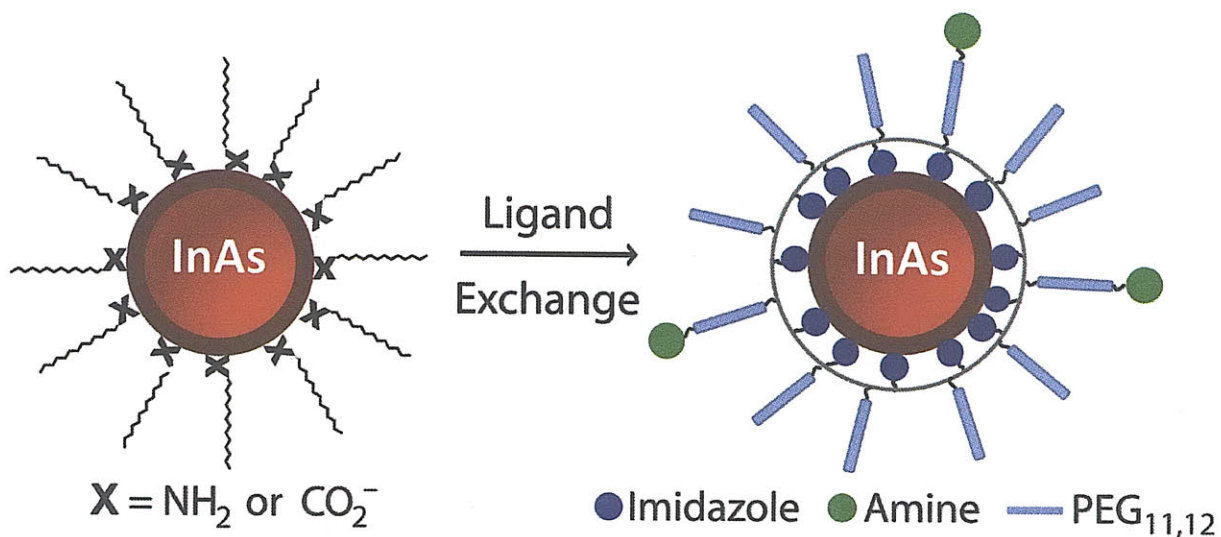


Figure 1-7. Ligand exchange of QDs with a poly(amino-PEG)-PIL polymer.

As synthesized, QDs are typically soluble in non-polar organic solvents such as hexanes or toluene. There are several routes to transferring the QDs to the water phase. An amphiphilic polymer or phospholipids can be used to encapsulate the QDs while retaining the native capping ligands, however these methods significantly increase the hydrodynamic diameter (HD).^[63-66] In order to produce more compact water soluble QDs, a ligand exchange procedure can be utilized (Figure 1-7). A 'ligand exchange' displaces the native hydrophobic capping ligands with hydrophilic capping ligands to impart water solubility. Previous ligands have included a

phosphine oxide polymer, monothiol, and dihydrolipoic acid derivatives which produced QDs with HDs from 5-15 nm, however these systems were plagued with colloidal instability.^[54, 67-70] Recently, there have been major developments in the synthesis of imidazole based polymeric ligands, coined poly-imidazole ligands (PIL). The PIL based ligand architecture produces highly stable and compact (hydrodynamic diameter ~10 nm), non-sticky QDs that are amenable to functionalization via terminal amine groups for specific labeling.^[71]

The ligand exchange process is harsh on the QD surface and as a result, only high quality lattice matched core-shell materials can withstand the process. The growth of high quality shells on NIR InAs QDs is presented in Chapter 3 to enable ligand exchange on III-V QDs, while retaining reasonably high quantum yields.

1.5 Thesis Overview

The theme of this thesis is the pursuit of new synthetic methods, and the understanding of the molecular mechanisms, involved in the synthesis of binary III-V and ternary I-III-VI QD materials. The ultimate goal of the exploration of new materials is to discover new material properties and enable the application of QDs across a wide range of technologies. The ability to controllably synthesize any semiconductor material, from II-VI, III-V, IV-VI, IV, to I-III-VI semiconductors would greatly expand the materials toolbox available to scientists and engineers in the QD field, and enable the tailoring of material compositions and properties to specific application needs.

The experimental work of this thesis begins in Chapter 2 with an exploration of the synthesis of group I-III-VI QDs. These materials range from Cu-In-S, Ag-In-S, Cu-Zn-In-S, Ag-In-Se, to Cu-In-Se QDs emitting from the blue to near-infrared regions. However, precise

control over size distributions and shell growth has yet to be obtained. In my early stages as a graduate student I was eager to take on the most complex of QD formulations from ternary to quaternary materials – however, it became clear that significant synthetic challenges remained even for simple binary systems such as III-V QDs. My desire to develop III-V materials and see them applied to relevant real world systems led to the work in Chapter 3.

The primary contribution of Chapter 3 is the design of robust shell materials for InAs QDs emitting in the NIR region. Although there has been previous work on core-shell InAs QDs, each synthetic method suffered from a lack of long term stability, or poor stability during ligand exchange. Drawing from the extensive experience the Bawendi lab has with core-shell CdSe QDs, we were able to develop compact and bright InAs(ZnCdS) QDs that have performed well in biological systems. Seeing the synthesis of a material go from a round bottom flask to *in vivo* work with Massachusetts General Hospital has been one of the highlights of my thesis work.

During my work on InAs QDs, a conversation with Scott Geyer led to the work in Chapter 4. I had noticed at high temperatures, in the presence of cadmium carboxylates, that InAs QDs would begin to lose their first absorption feature. With Scott's insight into the ability for Cd to act as an acceptor in bulk and nanowire InAs, we set to exploring the possibility that we were doping InAs QDs with cadmium. Indeed, we were able to controllably synthesize 'p' and 'n' type InAs QDs. The ultimate dream of this work is the fabrication of a true p-n nanocrystal homo-junction device.

Chapter 5 is an exploration of the molecular mechanisms in current III-V QD syntheses, and outlines the current shortcomings in the synthetic approaches to InP and InAs QDs. When comparing single dot measurements on III-V QDs to II-VI CdSe QDs, it became clear that the broad features observed in ensemble optical properties for InP and InAs is the result of a

moderately broad size distribution, and not a fundamental limitation. Our work found that a critical criteria for monodisperse colloid formation, growth from molecular precursors, is not met due to the extreme reactivity of the tris(trimethylsilyl) phosphine and arsine precursors.

The mechanistic work on InP and InAs QDs led to the clear conclusion that new, less reactive, pnictide sources must be found. Chapter 6 outlines a detour taken into the nanowire world during the exploration of new phosphorus precursors. Frustrated by a lack of progress on developing new InP QD synthetic methods, the development of the electrically controlled solution-liquid-solid (EC-SLS) synthesis of nanowires by August Dorn and Cliff Wong caught my eye. We were able to use some of my precursor explorations to develop a new synthesis for InP nanowires in solution that was compatible with the electrically controlled process.

In summary, this thesis explores the synthesis of novel QD core materials, QD core-shell materials, doped QD materials, EC-SLS InP nanowires, and investigations into the molecular mechanisms involved in the formation of III-V QDs.

1.6 References

- [1] D. J. Milliron, S. M. Hughes, Y. Cui, L. Manna, J. Li, L.-W. Wang, A. Paul Alivisatos, *Nature* **2004**, *430*, 190.
- [2] V. F. Puntès, K. M. Krishnan, A. P. Alivisatos, *Science* **2001**, *291*, 2115.
- [3] P. Jongnam, J. Jin, K. Soon Gu, J. Youngjin, H. Taeghwan, *Angew. Chem.* **2007**, *46*, 4630.
- [4] S. Coe, W.-K. Woo, M. Bawendi, V. Bulovic, *Nature* **2002**, *420*, 800.
- [5] S. A. McDonald, G. Konstantatos, S. Zhang, P. W. Cyr, E. J. D. Klem, L. Levina, E. H. Sargent, *Nat Mater* **2005**, *4*, 138.
- [6] M. Bruchez, Jr., M. Moronne, P. Gin, S. Weiss, A. P. Alivisatos, *Science* **1998**, *281*, 2013.
- [7] P. M. Allen, B. J. Walker, M. G. Bawendi, *Angewandte Chemie International Edition* **2010**, *49*, 760.
- [8] P. M. Allen, W. Liu, V. P. Chauhan, J. Lee, A. Y. Ting, D. Fukumura, R. K. Jain, M. G. Bawendi, *Journal of the American Chemical Society* **2009**, *132*, 470.
- [9] P. M. Allen, M. G. Bawendi, *Journal of the American Chemical Society* **2008**, *130*, 9240.
- [10] V. L. Tassev, D. F. Bliss, *Journal of Crystal Growth* **2008**, *310*, 4209.
- [11] I. Stranski, L. Krastanov, *Akad. Wiss. Lit. Mainz* **1939**, *146*, 792.
- [12] C. h. Chiu, Z. Huang, C. T. Poh, *Physical Review Letters* **2004**, *93*, 136105.
- [13] B. A. Joyce, D. D. Vvedensky, *Materials Science and Engineering: R: Reports* **2004**, *46*, 127.
- [14] G. M. Dalpian, J. R. Chelikowsky, *Physical Review Letters* **2006**, *96*, 226802.
- [15] M. H. Du, S. C. Erwin, A. L. Efros, D. J. Norris, *Physical Review Letters* **2008**, *100*, 179702.
- [16] D. J. Norris, A. L. Efros, S. C. Erwin, *Science* **2008**, *319*, 1776.
- [17] C. B. Murray, D. J. Norris, M. G. Bawendi, *J. Am. Chem. Soc.* **1993**, *115*, 8706.
- [18] H. P. Rocksby, *J. Soc. Glass Technol.* **1932**, *16*, 171.
- [19] A. I. Ekimov, V. A. Onushchenko, A. Tsekhomskii, *Fizika i Khimiya Stekla* **1980**, *6*, 511.

- [20] A. I. Ekimov, V. A. Onushchenko, *Pis'ma v Zhurnal Eksperimental'noi i Teoreticheskoi Fizika* **1981**, 363.
- [21] A. Ekimov, *Journal of Luminescence* **1996**, 70, 1.
- [22] L. Goldstein, F. Glas, J. Y. Marzin, M. N. Charasse, G. Le Roux, *Applied Physics Letters* **1985**, 47, 1099.
- [23] D. Leonard, M. Krishnamurthy, C. M. Reaves, S. P. Denbaars, P. M. Petroff, *Applied Physics Letters* **1993**, 63, 3203.
- [24] M. A. Reed, J. N. Randall, R. J. Aggarwal, R. J. Matyi, T. M. Moore, A. E. Wetsel, *Physical Review Letters* **1988**, 60, 535.
- [25] P. Bhattacharya, S. Ghosh, A. D. Stiff-Roberts, *Annual Reviews of Materials Research* **2004**, 34, 1.
- [26] R. Rossetti, S. Nakahara, L. E. Brus, *The Journal of Chemical Physics* **1983**, 79, 1086.
- [27] T. Davis, *PNAS* **2005**, 102, 1277.
- [28] A. P. Alivisatos, *ACS Nano* **2008**, 2, 1514.
- [29] M. L. Steigerwald, A. P. Alivisatos, J. M. Gibson, T. D. Harris, R. Kortan, A. J. Muller, A. M. Thayer, T. M. Duncan, D. C. Douglass, L. E. Brus, *Journal of the American Chemical Society* **1988**, 110, 3046.
- [30] M. G. Bawendi, A. R. Kortan, M. L. Steigerwald, L. E. Brus, *The Journal of Chemical Physics* **1989**, 91, 7282.
- [31] V. K. LaMer, R. H. Dinegar, *J. Am. Chem. Soc.* **1950**, 72, 4847.
- [32] H. Liu, J. S. Owen, A. P. Alivisatos, *J. Am. Chem. Soc.* **2007**, 129, 305.
- [33] J. S. Steckel, B. K. H. Yen, D. C. Oertel, M. G. Bawendi, *J. Am. Chem. Soc.* **2006**, 128, 13032.
- [34] D. Battaglia, X. Peng, *Nano Letters* **2002**, 2, 1027.
- [35] H. Nakamura, W. Kato, M. Uehara, K. Nose, T. Omata, S. Otsuka-Yao-Matsuo, M. Miyazaki, H. Maeda, *Chem. Mater.* **2006**, 18, 3330.
- [36] J. I. Pankove, *Optical Processes in Semiconductors*, Dover, New York, **1971**.
- [37] L. E. Brus, *J. Chem. Phys.* **1984**, 80, 4403.
- [38] A. A. Guzelian, U. Banin, A. V. Kadavanich, X. Peng, A. P. Alivisatos, *Appl. Phys. Lett.* **1996**, 69, 1432.

- [39] D. J. Norris, MIT **1995**.
- [40] S. S. Jonathan, S. Preston, C.-S. Seth, P. Z. John, E. H. Jonathan, A. Polina, K. Lee-Ann, B. Vladimir, G. B. Mounji, *Angewandte Chemie International Edition* **2006**, *45*, 5796.
- [41] M. Stroh, J. P. Zimmer, D. G. Duda, T. S. Levchenko, K. S. Cohen, E. B. Brown, D. T. Scadden, V. P. Torchilin, M. G. Bawendi, D. Fukumura, R. K. Jain, *Nat. Med.* **2005**, *11*, 678.
- [42] C. B. Murray, MIT (Cambridge), **1995**.
- [43] S. Adam, D. V. Talapin, H. Borchert, A. Lobo, C. McGinley, A. R. B. d. Castro, M. Haase, H. Weller, T. Moller, *Journal of Chemical Physics* **2005**, *123*, 084706.
- [44] B. O. Dabbousi, J. Rodriguez-Viejo, F. V. Mikulec, J. R. Heine, H. Mattoussi, R. Ober, K. F. Jensen, M. G. Bawendi, *J. Phys. Chem. B* **1997**, *101*, 9463.
- [45] R. Xie, U. Kolb, J. Li, T. Basche, A. Mews, *Journal of the American Chemical Society* **2005**, *127*, 7480.
- [46] X. Peng, M. C. Schlamp, A. V. Kadavanich, A. P. Alivisatos, *Journal of the American Chemical Society* **1997**, *119*, 7019.
- [47] J. J. Li, Y. A. Wang, W. Guo, J. C. Keay, T. D. Mishima, M. B. Johnson, X. Peng, *Journal of the American Chemical Society* **2003**, *125*, 12567.
- [48] A. Aharoni, T. Mokari, I. Popov, U. Banin, *J. Am. Chem. Soc.* **2005**, *128*, 257.
- [49] Cao, U. Banin, *J. Am. Chem. Soc.* **2000**, *122*, 9692.
- [50] L. Li, P. Reiss, *J. Am. Chem. Soc.* **2008**, *130*, 11588.
- [51] M. A. Hines, P. Guyot-Sionnest, *The Journal of Physical Chemistry* **1996**, *100*, 468.
- [52] P. O. Anikeeva, J. E. Halpert, M. G. Bawendi, V. Bulovic, *Nano Letters* **2009**, *9*, 2532.
- [53] W. Liu, A. B. Greytak, J. Lee, C. R. Wong, J. Park, L. F. Marshall, W. Jiang, P. N. Curtin, A. Y. Ting, D. G. Nocera, D. Fukumura, R. K. Jain, M. G. Bawendi, *Journal of the American Chemical Society* **2009**, *132*, 472.
- [54] W. Liu, H. S. Choi, J. P. Zimmer, E. Tanaka, J. V. Frangioni, M. G. Bawendi, *J. Am. Chem. Soc.* **2007**, *129*, 14530.
- [55] S. Kim, B. Fisher, H.-J. Eisler, M. Bawendi, *Journal of the American Chemical Society* **2003**, *125*, 11466.
- [56] D. V. Talapin, J. H. Nelson, E. V. Shevchenko, S. Aloni, B. Sadtler, A. P. Alivisatos, *Nano Letters* **2007**, *7*, 2951.

- [57] R. Xie, X. Peng, *Angew. Chem.* **2008**, *47*, 7677.
- [58] B. Mahler, P. Spinicelli, S. Buil, X. Quelin, J.-P. Hermier, B. Dubertret, *Nat Mater* **2008**, *7*, 659.
- [59] Y. Chen, J. Vela, H. Htoon, J. L. Casson, D. J. Werder, D. A. Bussian, V. I. Klimov, J. A. Hollingsworth, *Journal of the American Chemical Society* **2008**, *130*, 5026.
- [60] E. B. Brown, R. B. Campbell, Y. Tsuzuki, L. Xu, D. Carmeliet, D. Fukumura, R. K. Jain, *Nat. Med.* **2001**, *7*, 864.
- [61] S. Kim, Y. T. Lim, E. G. Soltesz, A. M. De Grand, J. Lee, A. Nakayama, J. A. Parker, T. Mihaljevic, R. G. Laurence, D. M. Dor, L. H. Cohn, M. G. Bawendi, J. V. Frangioni, *Nat Biotech* **2004**, *22*, 93.
- [62] H. S. Choi, W. Liu, F. Liu, K. Nasr, P. Misra, M. G. Bawendi, J. V. Frangioni, *Nat Nano*, *5*, 42.
- [63] P. T. Snee, R. C. Somers, G. Nair, J. P. Zimmer, M. G. Bawendi, D. G. Nocera, *Journal of the American Chemical Society* **2006**, *128*, 13320.
- [64] Y. Chen, R. Thakar, P. T. Snee, *Journal of the American Chemical Society* **2008**, *130*, 3744.
- [65] B. Dubertret, P. Skourides, D. J. Norris, V. Noireaux, A. H. Brivanlou, A. Libchaber, *Science* **2002**, *298*, 1759.
- [66] M. Dahan, S. Levi, C. Luccardini, P. Rostaing, B. Riveau, A. Triller, *Science* **2003**, *302*, 442.
- [67] S.-W. Kim, S. Kim, J. B. Tracy, A. Jasanoff, M. G. Bawendi, *Journal of the American Chemical Society* **2005**, *127*, 4556.
- [68] W. Liu, M. Howarth, A. B. Greytak, Y. Zheng, D. G. Nocera, A. Y. Ting, M. G. Bawendi, *Journal of the American Chemical Society* **2008**, *130*, 1274.
- [69] H. T. Uyeda, I. L. Medintz, J. K. Jaiswal, S. M. Simon, H. Mattoussi, *Journal of the American Chemical Society* **2005**, *127*, 3870.
- [70] J. Aldana, Y. A. Wang, X. Peng, *Journal of the American Chemical Society* **2001**, *123*, 8844.
- [71] W. Liu, A. B. Greytak, J. Lee, C. R. Wong, J. Park, L. F. Marshall, W. Jiang, P. N. Curtin, A. Y. Ting, D. G. Nocera, D. Fukumura, R. K. Jain, M. G. Bawendi, *Journal of the American Chemical Society* **2009**.

Chapter 2. Ternary I-III-VI Quantum Dots

2.1 Introduction

In this chapter we explore the synthesis of various ternary and quaternary quantum dots (QDs). By expanding from binary semiconductors such as II-VI (CdSe), IV-VI (PbSe), or III-V (InAs), to ternary I-III-VI semiconductors it is possible to significantly expand our choice of QD material composition (Figure 2-1).^[1-3] We will focus on the synthesis and characterization of a series of copper indium selenide (CIS) QDs of various stoichiometries exhibiting photoluminescence (PL) from the red to near infrared (NIR). In addition, we have demonstrated the modularity of our synthetic method by extending it to the synthesis of AgInSe₂, Ag-In-Zn-S, and Cu-In-Zn-S QDs which are luminescent from the blue to NIR. Ternary I-III-VI QDs could find widespread technological applications in areas ranging from photovoltaic cells to biological imaging agents.^[4, 5]

In bulk CIS semiconductors, band edge PL is rarely observed at room temperature due to fast non-radiative relaxation promoted by defect sites.^[6] In addition, previous work on CIS QDs has not reported PL.^[7-9] In the area of sulfide based I-III-VI QD systems, the incorporation of zinc has been necessary in order to enhance quantum yields (QYs) and tune emission properties.^[10, 11] Here, we present selenium based I-III-VI ternary semiconductor systems and also explore sulfide based I-III-VI semiconductors with the incorporation of zinc.

Previous CIS QD synthetic work has utilized single source precursors.^[8] However, this methodology was not amenable to the facile introduction of capping ligands, preventing adequate size control and surface passivation. Other reports have utilized CuCl, InCl₃, and tri-n-

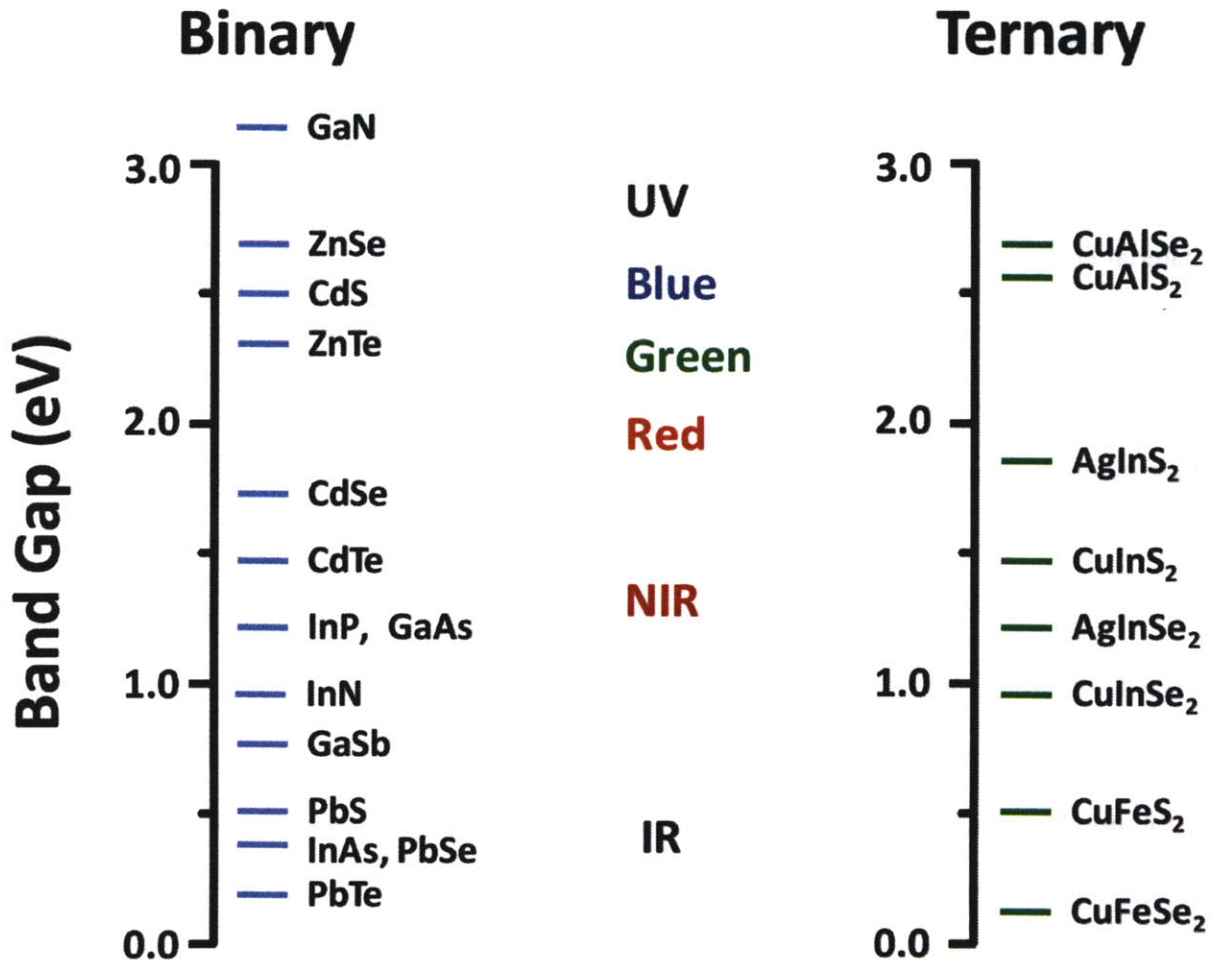


Figure 2-1. Binary and ternary semiconductor band gaps.

octylphosphine selenide (TOPSe) to synthesize CIS QDs, but did not produce QDs with distinct absorption features.^{7,9} In our synthetic approach, we have selected bis(trimethylsilyl) selenide $[(\text{Me}_3\text{Si})_2\text{Se}]$ and bis(trimethylsilyl) sulfide $[(\text{Me}_3\text{Si})_2\text{S}]$, as the chalcogenide precursors. The choice of copper precursors was limited by the tendency of Cu(I) to disproportionate in solution.^[12] Previous reports have demonstrated the copper and indium halides to be stable sources of Cu(I) and In(III). A combination of metal halides and a chalcogenide silane precursor was selected in order to exploit a metathetical dehalosilylation reaction scheme, obviating the need to generate elemental copper and indium in solution.^[13] Using this synthetic approach we demonstrate the synthesis of Cu-In-Se, AgInSe₂, Ag-In-Zn-S, and Cu-In-Zn-S QDs.

2.2 Cu-In-Se Quantum Dots

2.2.1 Synthesis

The solvent system is based on a combination of tri-n-octylphosphine (TOP) and oleyl amine (OA), which are used as a coordinating solvent. The metal halides can be readily dispersed in TOP or OA to form homogeneous solutions. In a typical synthesis, a solution of metal halides in TOP and OA was heated to 280–360 °C followed by the swift injection of a solution of $(\text{Me}_3\text{Si})_2\text{Se}$ in TOP and subsequent growth at temperatures ranging from 200–280 °C.

The CuI and InI₃ precursors produced QDs of composition CuIn₅Se₈, with PL in the red and NIR (Figure 2-2.a). In the case of the CuCl and InCl₃ precursors it was possible to tune the composition of the prepared QDs from CuIn_{1.5}Se₃ to CuIn_{2.3}Se₄ (Figure 2-2.b) by varying the reaction temperature. This synthetic method produced a size series of CIS QDs of various stoichiometries luminescent from the red to NIR (Figure 2-3).

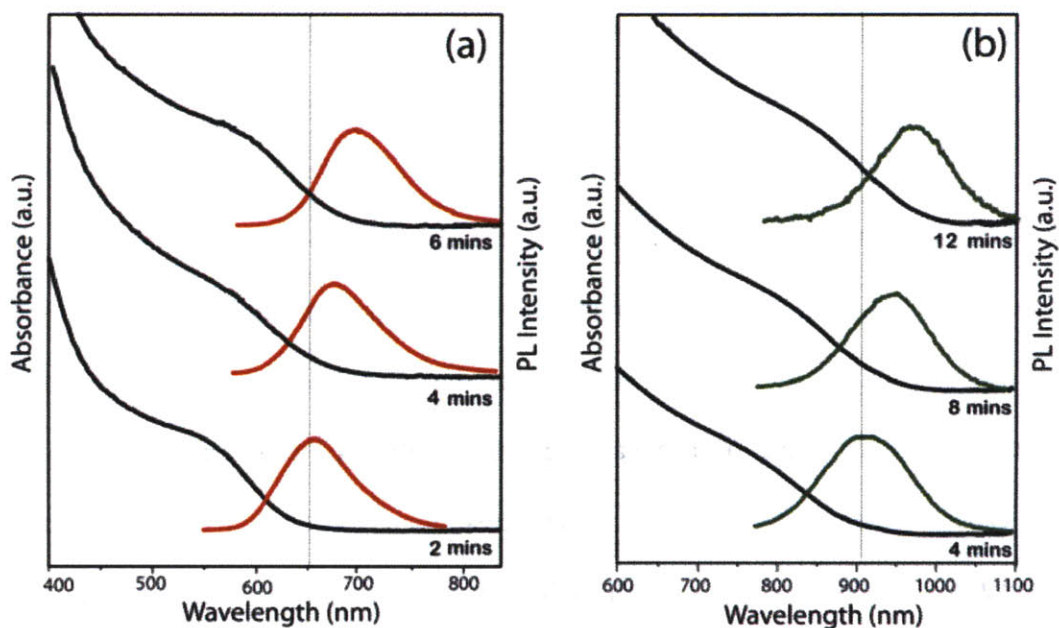


Figure 2-2. Absorbance and PL of Cu-In-Se QDs. Absorbance and corresponding PL of QD growth: (a) CuIn_5Se_8 QDs grown from 650–700nm with injection at 280 °C and growth at 210 °C from CuI and InI_3 precursors and (b) growth of $\text{CuIn}_{2.3}\text{Se}_4$ QDs from 900–975 nm with identical conditions as in (a) from CuCl and InCl_3 precursors.

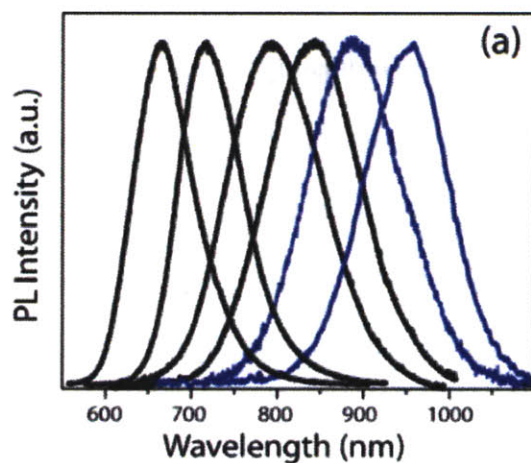


Figure 2-3. PL series and TEM of Cu-In-Se QDs. (a) PL spanning from the red to the NIR (650–975 nm) composed of CuIn_5Se_8 QDs ranging from ~2.0–3.5 nm mean diameter (black) and $\text{CuIn}_{2.3}\text{Se}_4$ QDs from ~3.0–3.5 nm mean diameter (blue).

The homogeneous and controllable growth of Cu-In-Se QDs was found to be strongly dependent on the ratio of Cu:In introduced in the reaction mixture. When using the iodide precursors, a Cu:In ratios of 1:1 produced bimodal distributions of Cu-In-Se. However, by adjusting the Cu:In ratios to 1:5 the growth of the homogeneous sample in Figure 2-2.a was obtained. When using the chloride based precursors, a 1:1 ratio of Cu:In was found to produce homogeneous size distributions of $\text{CuIn}_{2.3}\text{Se}_4$ QDs.

2.2.2 Elemental Composition and TEM

The elemental compositions of the QDs resulting from the reaction of the iodide and chloride precursors with $(\text{Me}_3\text{Si})_2\text{Se}$ were found to be independent of the reaction conditions (Figure 2-4). At constant growth temperatures, the final QD elemental composition was dictated by the choice of halide starting materials.

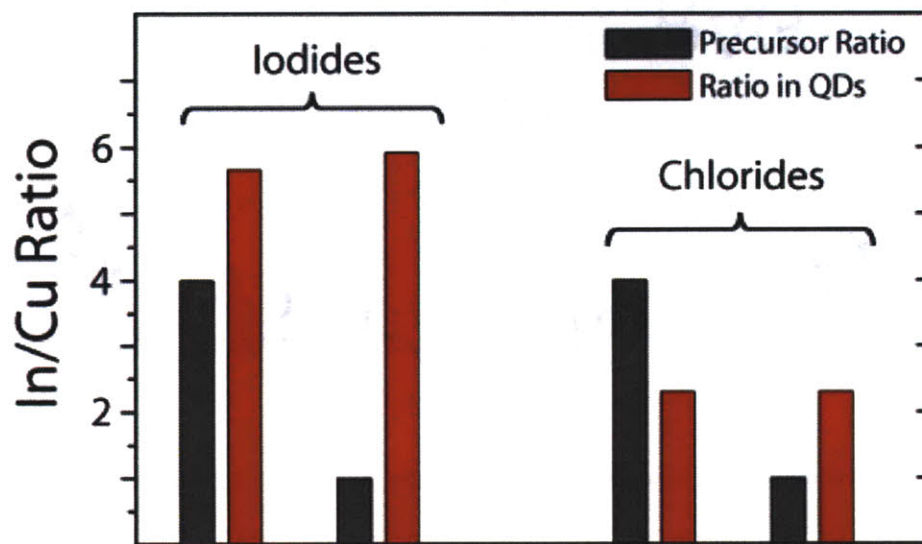


Figure 2-4. Graph showing the ratio of In/Cu precursors in growth solution and the resulting ratio of In/Cu in the produced QDs. The iodide and chloride precursors were examined at different ratios in growth solution. The final QD elemental compositions were found to be independent of the ratios of In/Cu precursors in growth solution.

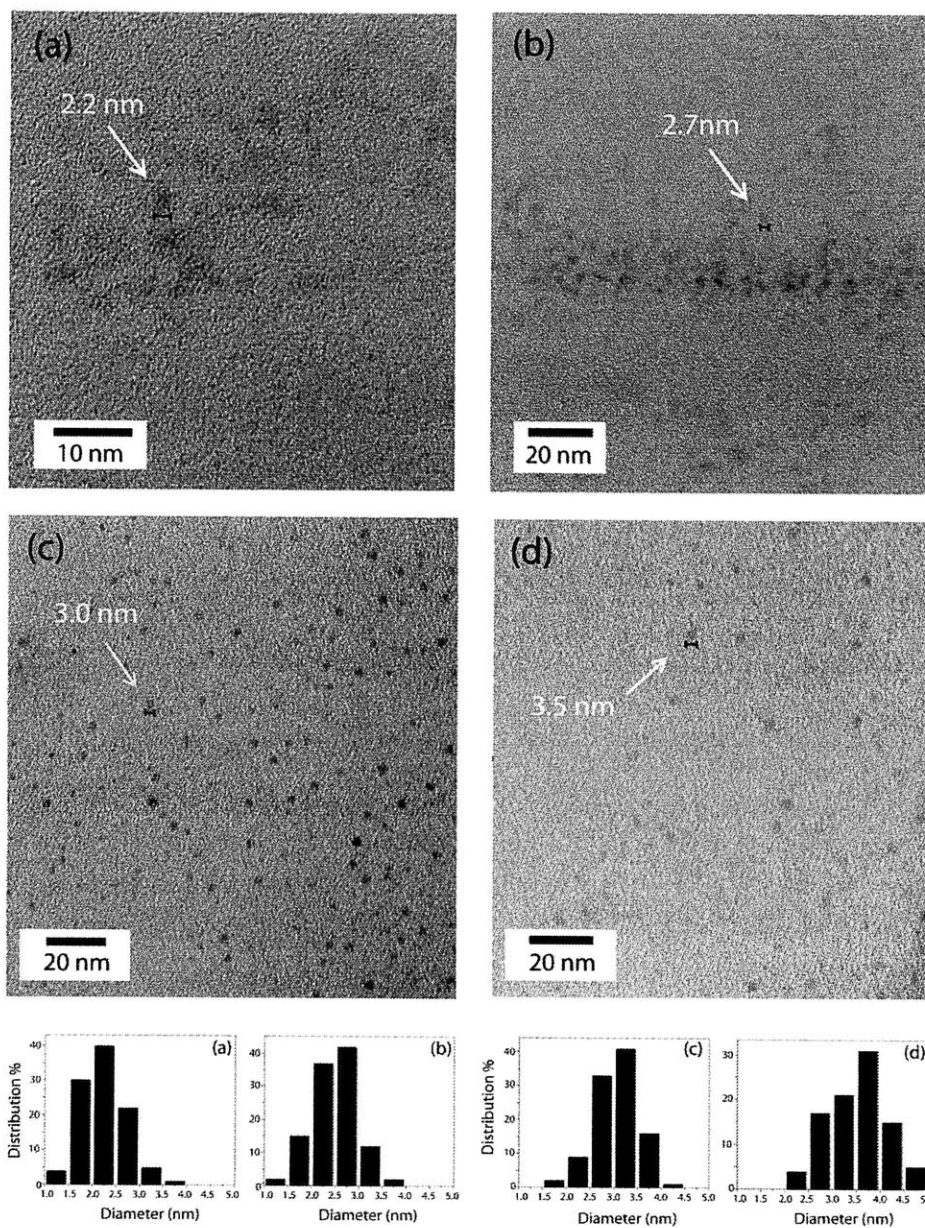


Figure 2-5. TEM and corresponding histograms of Cu-In-Se QDs: (a) TEM of ~ 2.2 nm mean diameter CuIn_5Se_8 QDs collected on a JEOL 2011 microscope, (b) TEM of ~ 2.7 nm mean diameter CuIn_5Se_8 QDs, (c) TEM of ~ 3.0 nm mean diameter $\text{CuIn}_{2.3}\text{Se}_4$ QDs, and (d) TEM of ~ 3.5 nm mean diameter $\text{CuIn}_{2.3}\text{Se}_4$ QDs collected on a JEOL 200CX microscope. Arrows indicate QDs with diameters equal to the mean diameter of the population of QDs, reference bars placed below the QDs are to scale with the labeled value.

Transmission electron microscopy (TEM) indicates the QDs are spherical in nature with an approximately 15–20% rms deviation in size from the mean QD diameter (Figure 2-5). The sizes determined by TEM measurements are in agreement with those obtained by Scherer analysis, suggesting the crystalline coherence length extends over the entire QD. It should be noted that at small QD sizes <2.5 nm, accurate sizing is complicated by poor TEM contrast.

2.2.3 Wide Angle X-Ray Scattering

Bulk and thin film CIS exist primarily in either a tetragonal chalcopyrite phase or a high temperature cubic sphalerite phase.^[14] The observed wide angle X-ray scattering (WAXS) and elemental compositions of the CIS QDs were found to be well described by an ordered vacancy chalcopyrite (OVC) structure. Analysis of 6 nm $\text{CuIn}_{1.5}\text{Se}_3$ QDs WAXS data began by creating a chalcopyrite model unit cell using experimentally determined copper, indium, and selenium site occupancies. Copper vacancies (V_{Cu}) were initially placed exclusively on the copper site, resulting in the calculated pattern in Figure 2-6.a. However, the calculated intensities for the (211) and (101) reflections in this model structure exceed the observed WAXS intensities. The indium atoms were then allowed to migrate onto the copper site (In_{Cu}) until the calculated pattern was in agreement with the observed pattern (Figure 2-6.b). A structural model containing In_{Cu} and $2V_{\text{Cu}}$ defect pairs is in agreement with an ordered vacancy chalcopyrite (OVC) phase. The elemental compositions of all the CIS QDs are consistent with the predicted stoichiometries for ordered vacancy CIS compounds (Figure 2-7).^[15] An alternative cubic sphalerite model unit cell does not adequately describe the observed WAXS pattern (Figure 2-6.c). Similar WAXS analysis for smaller CIS QDs was complicated by the inability to adequately resolve the (211) reflection due to increased peak broadening.

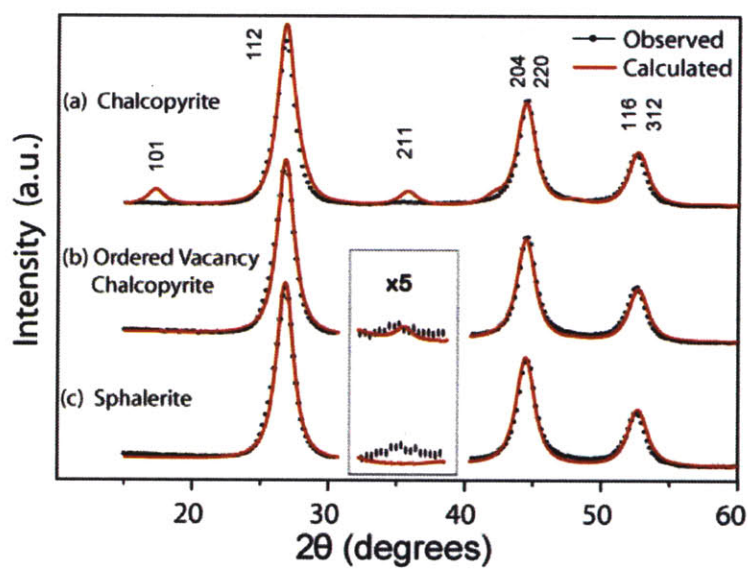


Figure 2-6. WAXS of Cu-In-Se QDs. Comparison of experimental WAXS to calculated patterns for model unit cells of $\text{CuIn}_{1.5}\text{Se}_3$ QDs (6 nm diameter). (a) The calculated pattern for a chalcopyrite phase where the calculated intensity of the (211) and (101) reflections exceed the observed intensity, (b) is the calculated pattern for an ordered vacancy chalcopyrite phase in agreement with the observed WAXS pattern, and (c) is a calculated cubic sphalerite phase that lacks the (211) reflection.

Ordered Defect Compound (Normalized to Cu)			QD Composition (Normalized to Cu)		
Cu	In	Se	Cu	In	Se
1	5	8	1	5.63	8.89
1	3	5	-	-	-
1	2.33	4	1	2.33	4.11
1	2	3.5	-	-	-
1	1.8	3.2	-	-	-
1	1.67	3	-	-	-
1	1.57	2.86	1	1.57	2.95

Figure 2-7. Predicted stoichiometries of “ordered defect compounds” (ODC) compared with the experimentally determined stoichiometries in CIS QDs.² Predicted compound stoichiometries were determined by repeating one defect unit consisting of an In_{Cu} atom and two V_{Cu} atoms for every (n) units of CuInSe_2 .

The assignment of $\text{CuIn}_{1.5}\text{Se}_3$ and $\text{CuIn}_{2.3}\text{Se}_4$ QDs as chalcopyrite compounds is in agreement with the previously reported chalcopyrite phases of bulk CuInSe_2 and CuIn_3Se_5 .^[16] As for CuIn_5Se_8 , only a metastable chalcopyrite phase has been reported in the bulk. Over the crystalline coherence lengths in this work (2–6 nm) chalcopyrite CIS QDs were observed over a large range of stoichiometries.

2.2.4 Temperature Dependent Photoluminescence

The observation of PL from CIS QDs (QYs up to 25% and decreasing significantly with increasing size) may arise due to the strong confinement of the exciton within the QD. Radiative pathways in the CIS QDs appear to remain competitive even in the presence of structural defects, which are known to promote the non-radiative relaxation in bulk CIS.⁶ In addition, QYs of the AgInSe_2 QDs reached 15%.

The broad PL (~100 nm fwhm) observed in the CIS QDs arises at least in part, if not fully, from a distribution of QD sizes. It is also possible that a distribution of near band edge trap states, known to arise from shallow donor acceptor pairs created by defects and vacancies, contributes to the broad PL.¹⁷ In order to distinguish between defect based emission, and band edge emission, temperature dependent PL measurements were carried out. The Cu-In-Se were embedded into a glassy polymer matrix and pressed between sapphire substrates. This homogeneous film was then placed into a cryostat for temperature dependent measurements.

The PL was found to blue shift with decreasing temperature (Figure 2-8). A blue shifting in PL has been observed for band edge emission in bulk Cu-In-Se semiconductors.^[6] The temperature dependent PL measurements strongly indicate the PL is band edge in nature, and not the result of emission from donor or acceptor defects.

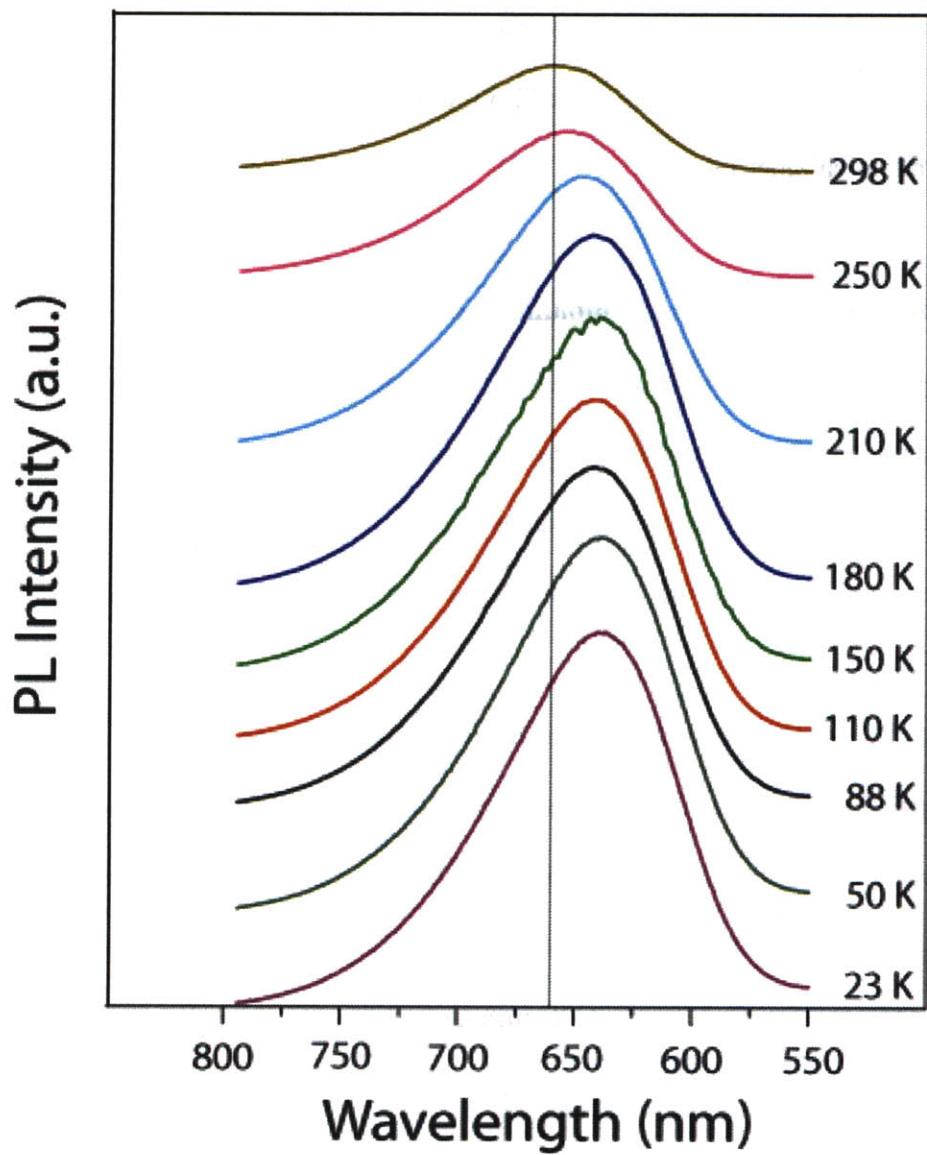


Figure 2-8. Temperature dependent PL of CuIn_5Se_8 QDs.

2.3 AgInSe₂ Quantum Dots

2.3.1 Synthesis

The generality of this synthetic approach was demonstrated by replacing the former metal halide precursors with AgI and InI₃, which successfully synthesized AgInSe₂ QDs with luminescence from orange to red (Figure 2-9). The QDs were observed to have PL efficiencies of 15-20%. Larger AgInSe₂ QDs could be grown with the use of AgCl and InCl₃, however, optical measurements were complicated by the formation of Ag colloids due to decomposition of AgCl at high temperature to Ag metal. The observation of Ag metal is confirmed by WAXS measurements in Figure 2-10.

2.3.2 Characterization

In the case of the AgInSe₂ QDs WAXS patterns it was not possible to distinguish between orthorhombic and hexagonal phases due to the small (3-6 nm) crystalline coherence lengths (Figure 2-10). It should be noted that the assignment of the 3 nm QDs cannot be distinguished between a tetragonal, hexagonal, or orthorhombic phase due to the broadened reflections due to the 3 nm crystalline coherence lengths. In the bulk, AgInSe₂ occurs primarily in the tetragonal phase, and the orthorhombic or hexagonal phases observed in this work are consistent with previously synthesized AgInSe₂ nanorods which have been reported to occur in an orthorhombic phase unique to nanocrystalline AgInSe₂.^[17] The 6 nm AgInSe₂ QDs are slightly ellipsoidal along the (002) axis, as evidenced by the increased intensity of the (002) peak observed in the WAXS patterns.

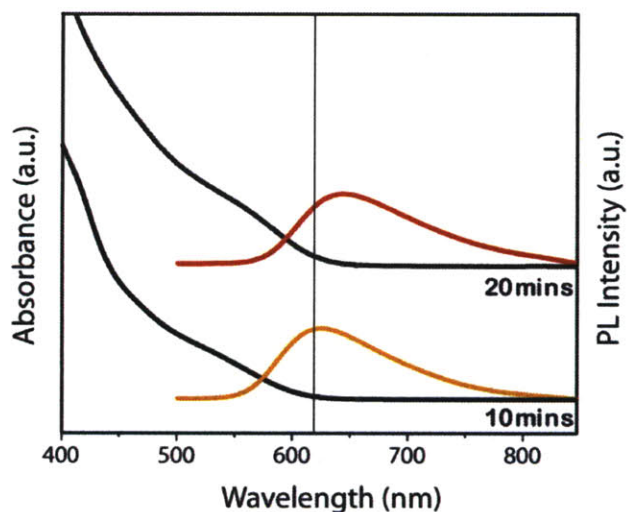


Figure 2-9. Absorbance and PL of AgInSe₂ QDs. Growth of AgInSe₂ QDs. Injection of precursors took place at 280 °C with subsequent growth at 210 °C. The AgInSe₂ QDs exhibit orange to red PL with ~15% QYs.

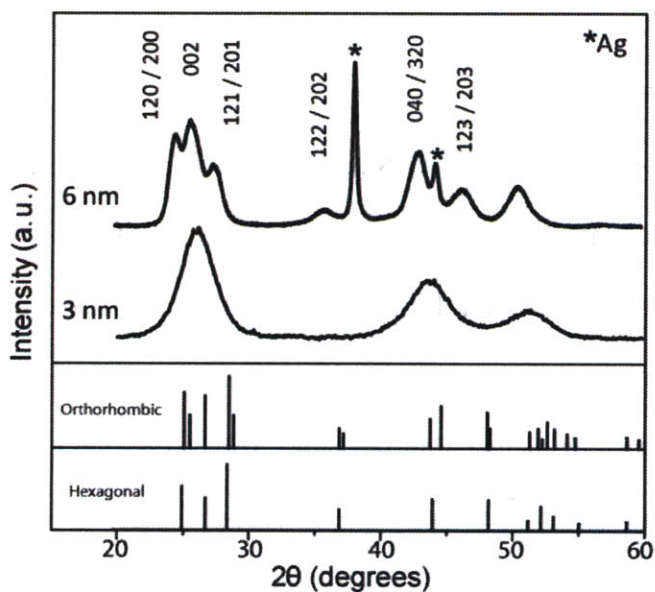


Figure 2-10. WAXS of 3 nm and 6 nm AgInSe₂ QDs. Orthorhombic and hexagonal bulk AgInS₂ reflections are overlaid. The observed reflections occur at a smaller 2θ than the bulk lines, as the AgInSe₂ unit cell is larger than the AgInS₂ unit cell. The observed reflections are labeled with orthorhombic reflections. Asterisks indicate Ag metal.

2.4 Cu-In-Zn-S and Ag-In-Zn-S Quantum Dots

The synthetic method for Cu-In-Se and Ag-In-Se QDs is modular, and can be extended to the Cu-In-Zn-S and Ag-In-Zn-S QD materials systems. By replacing bis(trimethylsilyl) selenide with bis(trimethylsilyl) sulfide, the complementary sulfide particles can be easily synthesized. However, in the case of the sulfide systems, zinc was incorporated into the core materials to enhance quantum yields. Sulfide QDs grown without the incorporation of zinc showed little to no photoluminescence.

The peak photoluminescence can be tuned by zinc content. Increasing zinc content results in the blue shifting of the photoluminescence peak. Green to NIR can be achieved with Cu-In-Zn-S QDs. Blue to red photoluminescence can be achieved with Ag-In-Zn-S QDs (Figure 2-11). The fwhm of the quaternary QD samples is quite broad (> 100 nm) this is likely the result of a combination of heterogeneous distributions in both of Zn incorporation and QD size distributions.

The bulk bandgap of CuInS_2 ($E_g = 1.5$ eV) and AgInS_2 ($E_g = 1.8$ eV), while ZnS has a bandgap of ($E_g = 3.54$ eV).^[18, 19] Therefore, it is likely that as Zn is incorporated into the core lattice, a blue shifting of the bandgap occurs. This is observed in our work, as well as previous work on Cu-In-Zn-S and Ag-In-Zn-S materials.^[10] The incorporation of Zn was also observed to increase the quantum yields of the QD samples. The brightest Cu-In-Zn-S QDs reached quantum yields of 30%, while the Ag-In-Zn-S quantum yields reached 15%. The growth of core-shell materials was complicated by the tendency of Zn to alloy into the QD core, instead of forming an epitaxial ZnS shell.

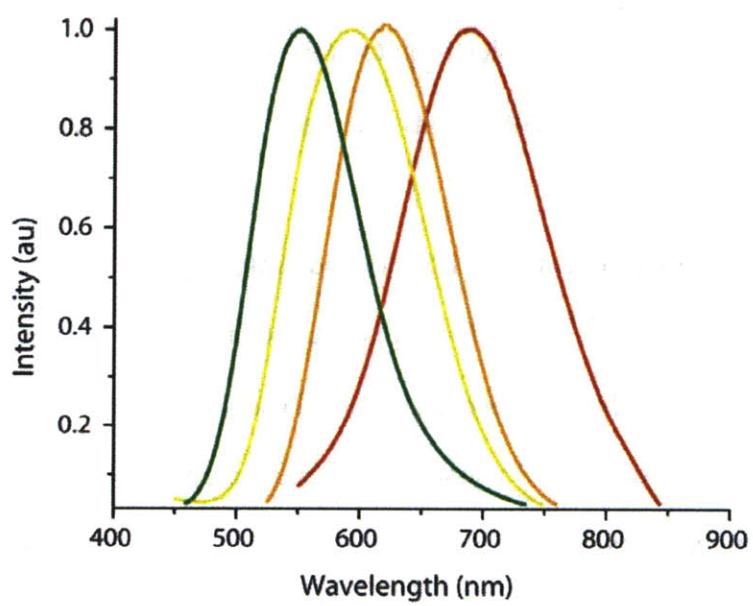
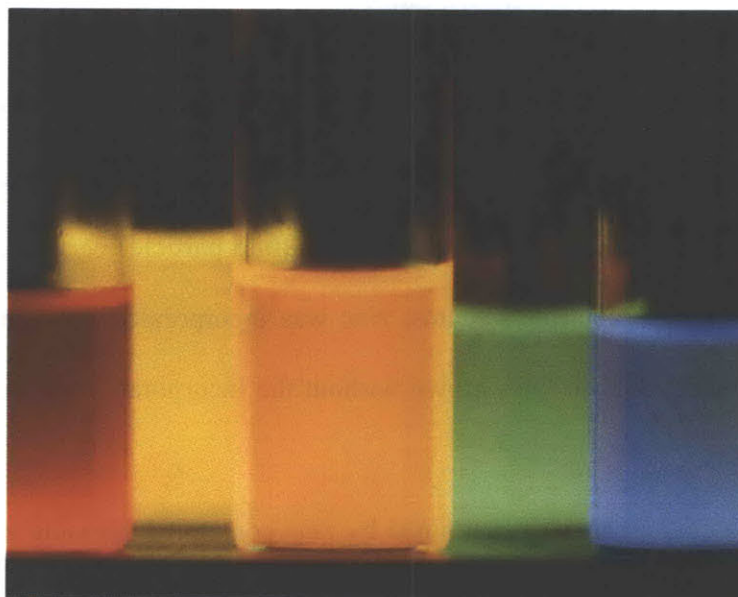


Figure 2-11. Emission spectra of Cu-In-Zn-S QDs and Ag-In-Zn-S QDs.

2.5 Conclusions

In the bulk, CuInSe_2 , CuIn_3Se_5 , and CuIn_5Se_8 have been reported with E_g values of 1.04 eV, 1.21 eV, and 1.15 eV, respectively.¹⁸ The E_g of CIS QDs has been tuned from 1.3–1.9 eV (corresponding to 975–650 nm), which is to the blue of the bulk E_g values. We conclude that quantum confinement plays a significant role in determining the E_g of CIS QDs,^[20] while differing elemental compositions may contribute additional but small E_g energy variations similar to those seen in bulk CIS.

The range of E_g values demonstrated by the CIS QDs in this work is comparable to the range attainable by thin film copper indium gallium selenide semiconductors (1.0–1.7 eV), which are used in photovoltaic devices.^[21] In addition, the small size and NIR emission of CIS QDs make them desirable for biological imaging applications.⁵ The growth of a ZnS shell around the CIS QDs could enable surface ligand modifications.

We have developed a modular hot injection synthetic method for ternary and quaternary QDs, composed of commercially available precursors. This synthetic method has the potential to be extended to other QDs composed of I-III-VI semiconductors, allowing for further exploration of the elemental compositions and electronic properties in QD materials.

2.6 Procedures

Materials: Stock solutions of metal halides were produced by combining two of the following complementary metal halides: CuCl, InCl₃, ZnI₂, CuI, AgI, or InI₃ (99.999%, Alfa Aesar) in tri-n-octylphosphine (97%, Strem) or oleyl amine (97%, Acros Organics) and heating to 90 °C under magnetic stirring for several hours in an inert glove box. All metal halide solutions were stored in the dark under an inert atmosphere. Tri-n-butylphosphine 99% was obtained from Strem. Bis(trimethylsilyl) selenide was obtained from Gelest. Methanol, Butanol, Hexanes, Toluene, and Pyridine (Anhydrous, Sigma) were used in the isolation of QD samples. All chemicals were used without further purification. All manipulations were carried out in an inert glove box or on a N₂ schlenk line using standard air free procedures.

CuIn₅Se₈ QDs: The CuIn₅Se₈ QDs were synthesized by injecting a solution of (Me₃Si)₂Se (0.15 mmol) in 2 ml of TOP into a round bottom flask containing OA (1.5 ml), TOP (3 ml), CuI (0.012 mmol), and InI₃ (0.060 mmol) stirring rapidly at 280 °C. The temperature was allowed to drop to 210 °C, when heating was restored for QD growth. Prolonged growth times can result in etching of the QDs.

CuIn_{2,3}Se₄ QDs: The CuIn_{2,3}Se₄ QDs were synthesized by injecting a solution of (Me₃Si)₂Se (0.25 mmol) in 2.5 ml of TOP into a round bottom flask containing OA (3 ml), TOP (2.5 ml), CuCl (0.25 mmol), and InCl₃ (0.25 mmol) stirring rapidly at 280 °C. The temperature was allowed to drop to 210 °C, when heating was restored for QD growth.

CuIn_{1,5}Se₃ QDs: The CuIn_{1,5}Se₃ QDs were synthesized identically to CuIn_{2,3}Se₄ QDs, with the exception of an injection temperature of 350 °C and a growth temperature of 280 °C.

AgInSe₂ QDs: The AgInSe₂ QDs were synthesized by injecting a solution of (Me₃Si)₂Se (0.15 mmol) in 2 ml of TOP into a round bottom flask containing OA (1.5 ml), TOP (3 ml), AgI (0.05 mmol), and InI₃ (0.05 mmol) stirring rapidly at 280 C. The temperature was allowed to drop to 210 C, when heating was restored for QD growth.

Cu-In-Zn-S QDs: The Cu-In-Zn-S QDs were synthesized by injecting a solution of (Me₃Si)₂S (0.10-0.20 mmol) in 2 ml of TOP into a round bottom flask containing OA (1.5 ml), TOP (3 ml), CuI (0.05 mmol), ZnI₂ (0.0-0.20 mmol), and InI₃ (0.05 mmol) stirring rapidly at 280 °C. The temperature was allowed to drop to 210 °C, when heating was restored for QD growth.

Ag-In-Zn-S QDs: The Ag-In-Zn-S QDs were synthesized by injecting a solution of (Me₃Si)₂S (0.10-0.20 mmol) in 2 ml of TOP into a round bottom flask containing OA (1.5 ml), TOP (3 ml), AgI (0.05 mmol), ZnI₂ (0.0-0.20 mmol), and InI₃ (0.05 mmol) stirring rapidly at 280 °C. The temperature was allowed to drop to 210 °C, when heating was restored for QD growth.

Isolation of QDs: QDs were isolated by several cycles of precipitation through the addition of butanol and methanol followed by centrifugation for five minutes at 3900 rpm. This procedure is first performed on the growth solution and then performed subsequently upon QDs dispersed in hexane.

Transmission Electron Microscopy (TEM): TEM samples were prepared by placing one drop of a dilute dispersion of QDs in pyridine onto an ultrathin carbon film 400 mesh copper grid

(Ted Pella). After one minute the excess solvent was wicked away. TEM measurements were collected on a JEOL 200CX operated at 200 kV.

Wide Angle X-ray Scattering (WAXS): WAXS samples were prepared by dropping concentrated QD solutions out of pyridine or hexane onto a zero background substrate, leaving a film of QDs. WAXS data was collected on a Rigaku 185mm operating at 50 kV with a 300 milliamp flux.

X-Ray Photoelectron Spectroscopy (XPS): Several monolayers of QDs were spin cast from chloroform onto a silicon substrate for XPS analysis. A Kratos AXIS Ultra Imaging X-ray Photoelectron Spectrometer with an Al Ka source was used for XPS measurements. Binding energies determined by XPS were consistent with literature values for Cu(I) in a chalcogenide matrix (Figure S5).^[22]

Elemental Analysis: Wavelength Dispersive Spectroscopy (WDS) was used to determine the elemental composition of the QD inorganic core. Dried QD samples were placed onto a silicon wafer and coated with amorphous carbon to prevent charging during measurements. Samples were then analyzed by WDS on a JEOL 733 scanning electron microscope (SEM). All measurements were taken in triplicate (Table S1). Due to the high percentage of surface atoms on the QDs, the selective termination of the surface by either copper or indium could potentially bias the elemental analysis. Elemental analysis for nitrogen and phosphorous was performed by Desert Analytics. As each capping ligand contains either one nitrogen atom (OA) or one phosphorous atom (TOP), the ratio of OA to TOP on the surface of the QDs can be quantitatively determined. The ratio of OA to TOP was found to be 20 to 1.

2.7 References

- [1] C. B. Murray, D. J. Norris, M. G. Bawendi, *J. Am. Chem. Soc.* **1993**, *115*, 8706.
- [2] A. A. Guzelian, U. Banin, A. V. Kadavanich, X. Peng, A. P. Alivisatos, *Appl. Phys. Lett.* **1996**, *69*, 1432.
- [3] S. Hinds, S. Myrskog, L. Levina, G. Koleilat, J. Yang, S. O. Kelley, E. H. Sargent, *J. Am. Chem. Soc.* **2007**, *129*, 7218.
- [4] W. U. Huynh, J. J. Dittmer, A. P. Alivisatos, *Science* **2002**, *295*, 2425.
- [5] J. P. Zimmer, S. W. Kim, S. Ohnishi, E. Tanaka, J. V. Frangioni, M. G. Bawendi, *J. Am. Chem. Soc.* **2006**, *128*, 2526.
- [6] C. Shigefusa, *Appl. Phys. Lett.* **1997**, *70*, 1840.
- [7] M. A. Malik, P. O'Brien, N. Revaprasadu, *Adv. Mater.* **1999**, *11*, 1441.
- [8] S. L. Castro, S. G. Bailey, R. P. Raffaele, K. K. Banger, A. F. Hepp, *Chem. Mater.* **2003**, *15*, 3142.
- [9] H. Zhong, Y. Li, M. Ye, Z. Zhu, Y. Zhou, C. Yang, Y. Li, *Nanotechnology* **2007**, *18*, 025602.
- [10] H. Nakamura, W. Kato, M. Uehara, K. Nose, T. Omata, S. Otsuka-Yao-Matsuo, M. Miyazaki, H. Maeda, *Chem. Mater.* **2006**, *18*, 3330.
- [11] T. Torimoto, T. Adachi, K. i. Okazaki, M. Sakuraoka, T. Shibayama, B. Ohtani, A. Kudo, S. Kuwabata, *J. Am. Chem. Soc.* **2007**, *129*, 12388.
- [12] W. G. Courtney, *J. Phys. Chem.* **1956**, *60*, 1461.
- [13] R. L. Wells, C. G. Pitt, A. T. McPhail, A. P. Purdy, S. Shafieezad, R. B. Hallock, *Chem. Mater.* **1989**, *1*, 4.
- [14] B. Schumann, A. Tempel, G. Kühn, *Cryst. Res. Technol.* **1988**, *23*, 3.
- [15] S. B. Zhang, S.-H. Wei, A. Zunger, H. Katayama-Yoshida, *Phys. Rev. B* **1998**, *57*, 9642.
- [16] S. M. Wasim, C. Rincon, G. Marin, J. M. Delgado, *Appl. Phys. Lett.* **2000**, *77*, 94.
- [17] M. T. Ng, C. B. Boothroyd, J. J. Vittal, *J. Am. Chem. Soc.* **2006**, *128*, 7118.
- [18] L. I. Berger, *Handbook of Chemistry and Physics* **2008**, 77.
- [19] T. Torimoto, T. Adachi, K.-i. Okazaki, M. Sakuraoka, T. Shibayama, B. Ohtani, A. Kudo, S. Kuwabata, *Journal of the American Chemical Society* **2007**, *129*, 12388.

[20] L. E. Brus, *J. Chem. Phys.* **1984**, *80*, 4403.

[21] K. Ramanathan, G. Teeter, J. C. Keane, R. Noufi, *Thin Sol. Films* **2005**, *480-481*, 499.

[22] Y. Xie, X. Zheng, X. Jiang, J. Lu, L. Zhu, *Inorg. Chem.* **2002**, *41*, 387.

Chapter 3. InAs(ZnCdS) Quantum Dots for Biological Imaging in the Near-Infrared

3.1 Introduction

The near-infrared (NIR) region is of particular interest for *in vivo* biological imaging applications. An optical window exists from roughly 700-900 nm where the major components of tissue and serum absorb minimally (Figure 3-1). In addition, the NIR is a region of low auto-fluorescence which results in increased contrast for biological imaging agents. In this Chapter, we present the synthesis of core-shell InAs(ZnCdS) quantum dots (QDs) with bright and stable emission in the NIR region for biological imaging applications. We demonstrate how NIR QDs can image tumor vasculature, *in vivo*, with superior depth and contrast when compared to visible QDs. Targeted *in vitro* cellular labeling is also presented and may be useful for multiplexed and low auto-fluorescence biological imaging.^[1, 2]

The push for smaller and smaller QDs has motivated the selection of InAs as the core material for NIR emitting QDs. Exceedingly small InAs cores (1.4 nm diameter) emit light at 1.78 eV (700 nm) in the heart of the NIR window.^[3] This is the result of a narrow bulk band gap of $E_g = 0.37$ eV and an extremely light electron effective mass, resulting in strong confinement of the carriers.^[4, 5] This fortunate combination of physical properties allows for the synthesis of semiconductor nanocrystals composed of approximately eight unit cells!

Previous work on InAs core-shell QDs has primarily focused on shell materials based on the selenides, specifically ZnSe and CdSe.^[3, 6, 7] Selenium is prone to surface oxidation in QDs,^[8] which may hinder stability and surface modifications. InAs core-shell materials based on the air-stable sulfides have been limited to the highly lattice mismatched (10.71%) ZnS shell.^[9, 10]

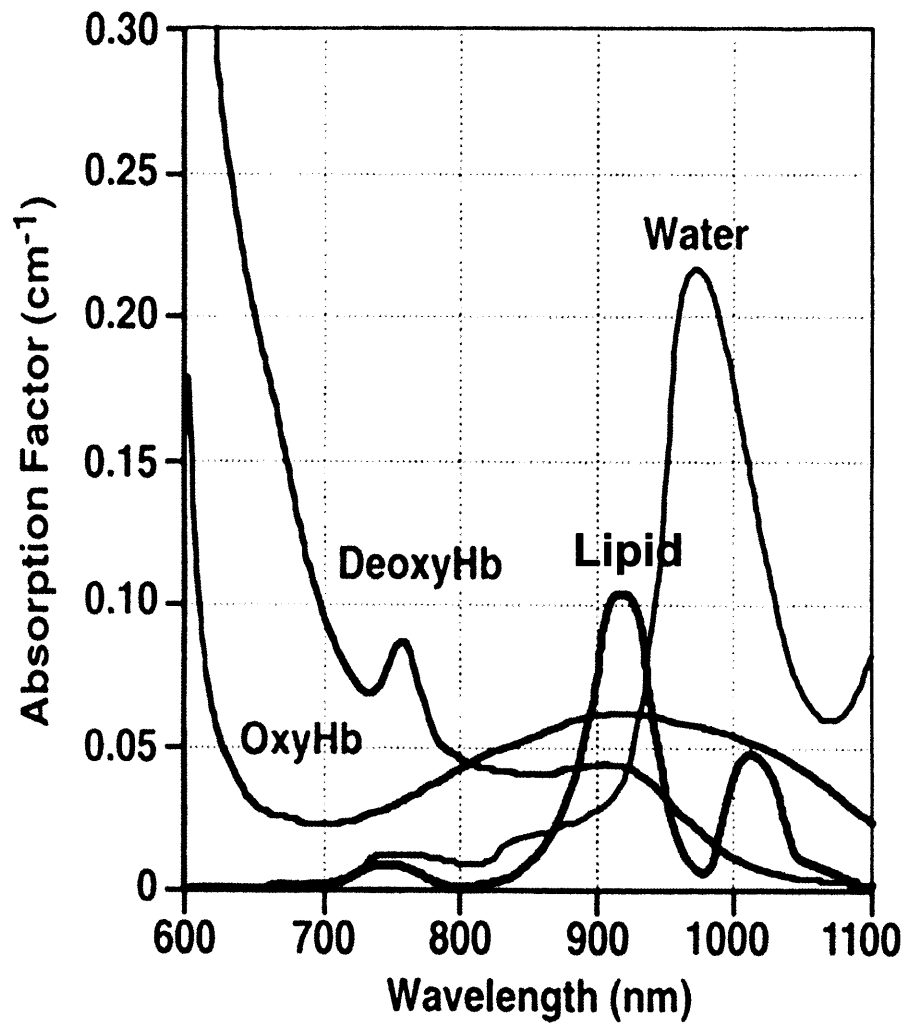


Figure 3-1. Near-infrared window for biological imaging.

3.2 InAs(ZnCdS) Quantum Dots

3.2.1 Synthesis

Previous literature claims have propagated a belief that III-V QDs suffer from low quantum yields (QYs), however a physical reason that III-V QDs should be ‘darker’ than their II-VI counterparts is not discussed.^[7, 11] The previously observed low QYs in III-V QDs likely arises from surface oxidation of the QDs or poor core-shell interfaces opening up non-radiative pathways. If a high quality core-shell material can be synthesized, there is no fundamental reason that III-V QDs cannot rival their II-VI counterparts.

In order to improve photoluminescence quantum yields (QYs) and the long term stability of InAs QDs we have looked to the well-studied CdSe QD system for inspiration on robust shell materials. As the CdSe ($a = 6.05 \text{ \AA}$, zinc blende) lattice parameters are nearly identical to those of InAs ($a = 6.058 \text{ \AA}$),^[12] we hypothesized similar shell materials would be transferable between the two systems. CdSe(CdS) and CdSe(ZnCdS) core-shell QDs have been shown to provide a robust QD surface that can withstand the conditions of ligand exchange, a necessary criterion for compact water soluble QDs.^[13, 14] A shell of CdS or the alloy ZnCdS has not been previously reported on InAs QDs. The reduction of lattice mismatch (CdS, 3.73%)^[12] between the core and shell semiconductors and the use of an air-stable sulfide based shell is necessary for QD stability during ligand exchange.^[13] The growth of a pure CdS shell onto InAs QDs results in red shifting of emission past the 800 nm window before even one monolayer (ML) is grown. While a pure ZnS shell confines the electron and hole to the InAs core (minimal red shifting)^[9] the high lattice mismatch of ZnS is not ideal for ligand exchange. We have found a ZnCdS alloy provides a shell with reduced lattice mismatch and moderate confinement of the hole and electron to the InAs core for wavelength targeting (Figure 3-2).

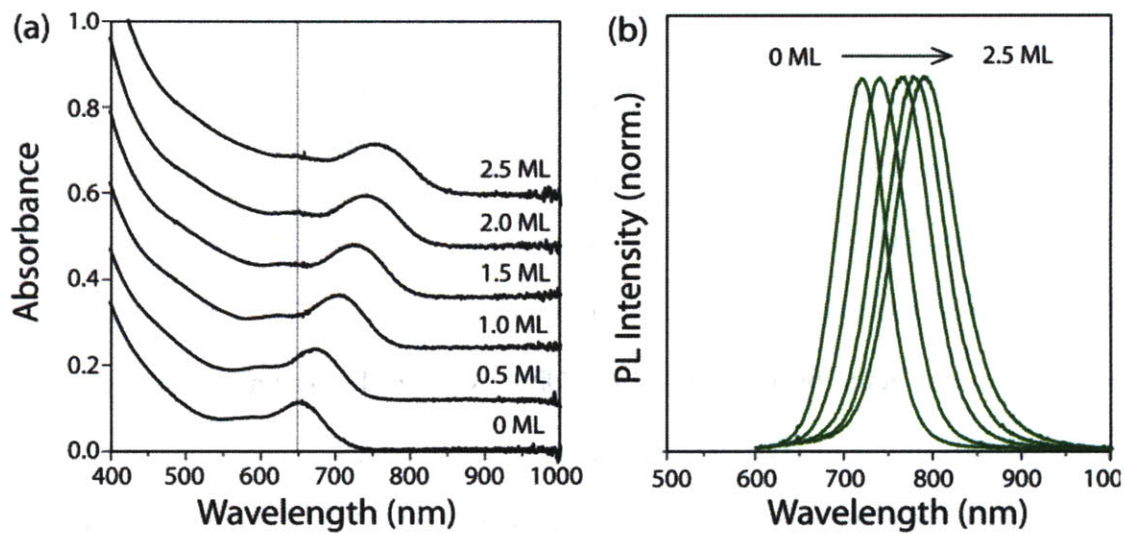


Figure 3-2. Absorbance and PL of InAs(ZnCdS) QDs. (a-b) Absorbance and PL of InAs(Zn_{0.7}Cd_{0.3}S) during shell growth from 0-2.5 monolayers (MLs).

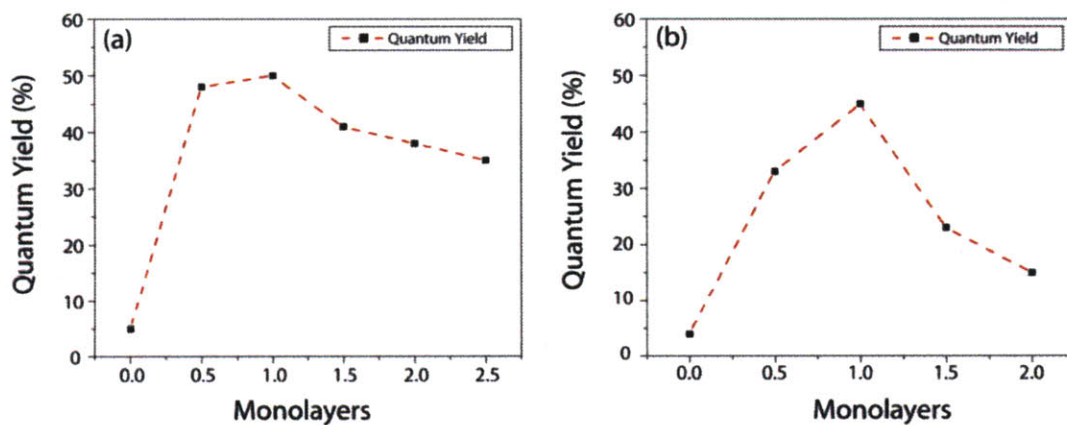


Figure 3-3. Quantum Yields during InAs(ZnCdS) shell growth. (a) Quantum yields as a function of ZnCdS shell growth on InAs cores with the addition of oleyl amine and (b) the growth of a ZnCdS shell without the addition of oleyl amine.

The synthesis of small InAs cores (1.4 nm inorganic diameter) was carried out in a mixture of octadecene, tri-*n*-octyl phosphine (TOP), tris(trimethylsilyl) arsine, and indium myristate using a slightly modified version of the synthesis reported by Xie and Peng.^[3] The addition of oleyl amine prior to shell growth was found to significantly improve quantum yields during the over-coating process (Figure 3-3). Also, the addition of oleyl amine serves to dilute the reaction solution, which was found to promote homogeneous shell growth. The ZnCdS QD shell was grown over several hours by the drop-wise addition of dimethyl cadmium, diethyl zinc, and bis(trimethylsilyl) sulfide in TOP. The shell thickness and ZnCdS composition can be precisely tuned by reaction time and reagent concentrations. We found 2.5 MLs of Zn_{0.7}Cd_{0.3}S to provide small QDs (2.9 nm inorganic diameter) with emission at 800 nm (QYs 35-50%, Figure 3-2) that retain high QYs when ligand exchanged.

3.2.2 Ligand Exchange

Figure 3-4 demonstrates water solubilization of InAs(ZnCdS) QDs through ligand exchange with a polymeric imidazole ligand (PIL). The native organic capping ligands, in this case a mixture of myristate and oleyl amine, are displaced by the imidazole groups of the PIL polymer. Poly(amino-PEG₁₁)_{25%}-PIL is a random co-polymer built on an acrylic acid backbone incorporating poly(ethylene) glycol (PEG₁₂) groups for water solubility (25 mol %), amino-PEG₁₁ groups for conjugation chemistry (25 mol %), and imidazole groups for QD binding (50 mol %), the detailed synthesis and characterization of these polymers can be found elsewhere.^[14] The resulting aqueous QDs have a hydrodynamic diameter (HD) of <10 nm. The QYs of ligand exchanged QDs were typically 25% and are stable under ambient conditions on the order of months. This high degree of stability is essential for biological collaborations, as synchronizing

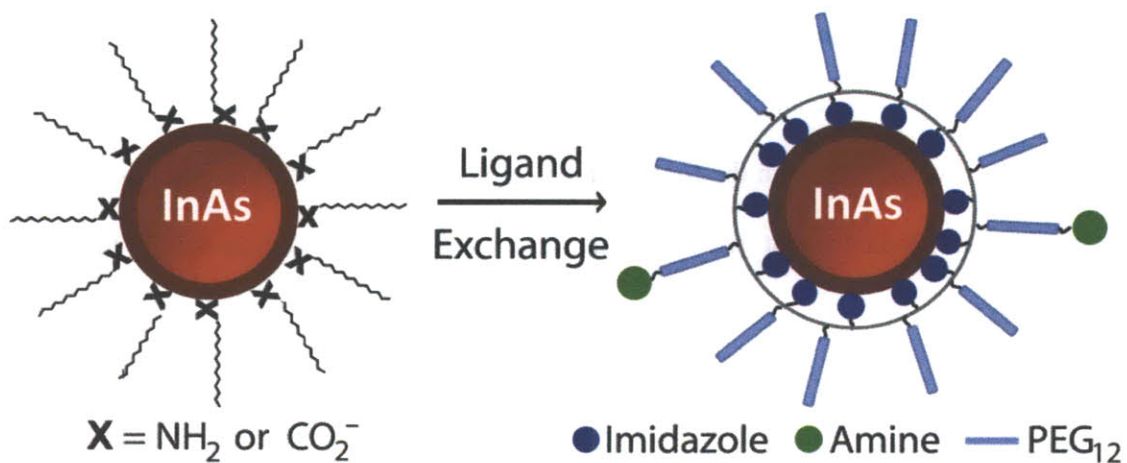


Figure 3-4. Schematic of ligand exchange. Ligand exchange of organic soluble QDs with poly(amino-PEG₁₁)-PIL to enable water solubilization.

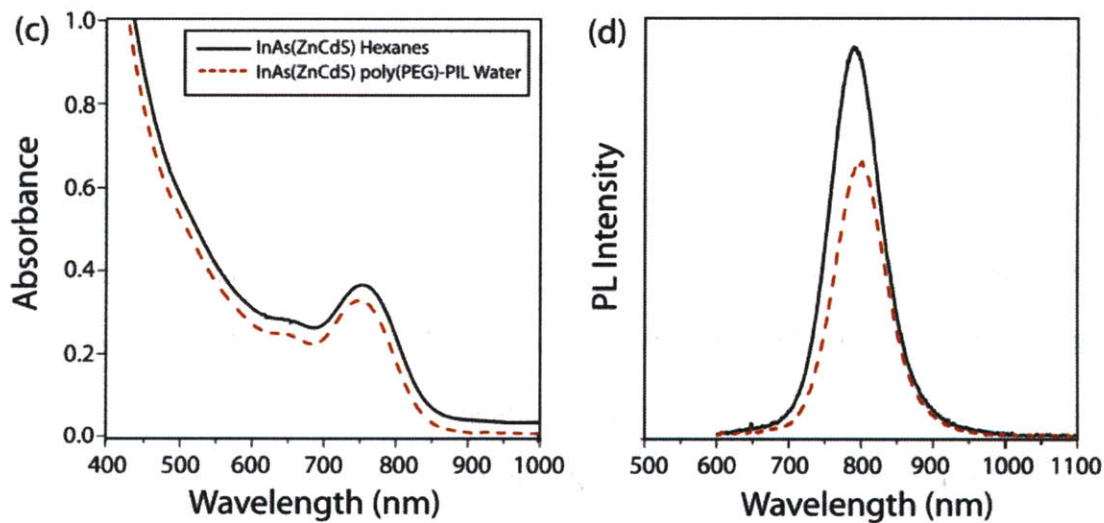


Figure 3-5. Absorbance and PL of InAs(Zn_{0.7}Cd_{0.3}S) QDs. (c-d) in hexanes (black) and after ligand exchange with poly(PEG₁₂)-PIL (red) in PBS at pH 7.4.

ligand exchanges with animal preparation is exceedingly difficult. Figure 3-5 demonstrates that the absorption spectrum remains identical before and after ligand exchange, and the small decrease in PL is consistent with the formation of a high quality shell. The percentage decrease in quantum yield is consistent with the quantum yield decreases observed in high quality CdSe(ZnCdS) QDs.^[13]

3.2.3 Characterization

The growth of a ZnCdS shell on the InAs core can be thoroughly characterized by a combination of TEM and elemental analysis. The TEM image serves a tool for determining the size and shape of the inorganic particle. TEM sizing is slightly complicated by the small <3 nm QDs characterized in this work (Figure 3-6.a). In order to aid analysis, a complementary measure of the elemental composition is essential in determining the number of monolayers of shell material grown over the core material.

The initial inorganic diameter is determined by its first absorption feature, and compared to previous reports in the literature.^[3] We begin with a 1.4 nm inorganic diameter InAs core and then grow a ZnCdS shell. The elemental composition of the InAs(ZnCdS) QDs is depicted in Figure 3-7. By comparing the experimentally determined values for elemental composition with the predicted values for various numbers of ZnCdS MLs the shell thickness can be quantified, and the InAs(ZnCdS) QDs in this work were found to have ~2.5 MLs of ZnCdS.

In order to determine the hydrodynamic diameter of the poly(PEG₁₂)-PIL QDs, gel filtration chromatography (GFC) was performed. The GFC column was calibrated using protein standards of known molecular weights and hydrodynamic diameters. The poly(PEG₁₂)-PIL InAs(ZnCdS) QDs were found to elute at 4.1 minutes, corresponding to a hydrodynamic diameter of <10 nm

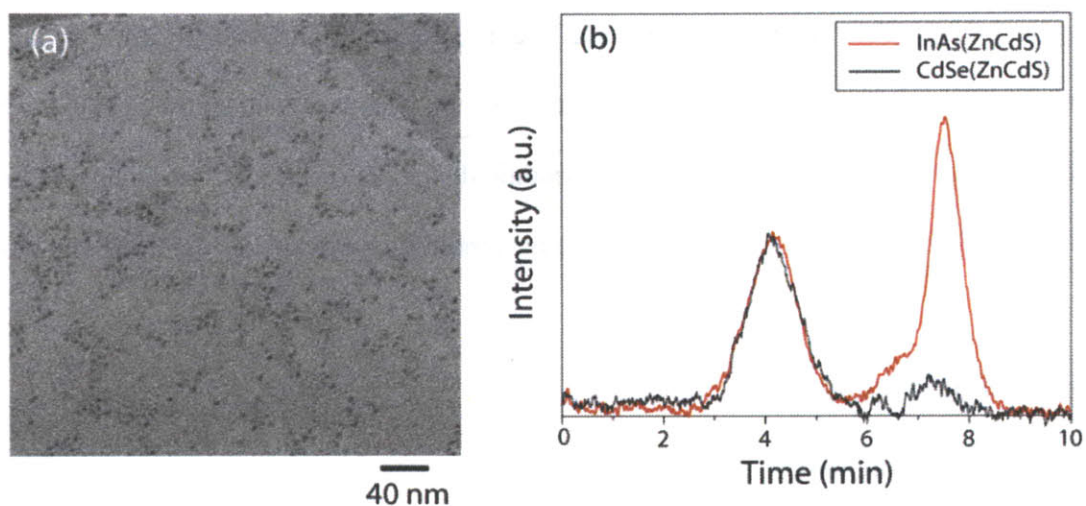


Figure 3-6. TEM and GFC of poly(PEG₁₂)-PIL InAs(ZnCdS) QDs. (a) TEM of InAs(ZnCdS) QDs with inorganic size ~2.9 nm drop-cast from water. (b) GFC of InAs(ZnCdS) poly(PEG₁₂)-PIL (red) QDs with a retention time of 4.17 minutes corresponding to a HD of <10 nm (the peak at 7.5 minutes corresponds to free poly(PEG)-PIL ligand) and CdSe(CdS) poly(PEG₁₂)-PIL (black) QDs with a retention time of 4.10 minutes or a HD of <10 nm.

(a) InAs(ZnCdS) Experimental Shell Growth

QD	Size (Diameter)	S/As Ratio
InAs(ZnCdS)	2.9 +/- 0.3 nm (TEM)	7.1 +/- 0.1 (WDS)

(b) InAs(ZnCdS) WDS Atomic %

In	As	Cd	Zn	S
6.4 +/- 0.2 %	5.6 +/- 0.2 %	15.0 +/- 0.3 %	32.8 +/- 0.7 %	39.8 +/- 0.8 %

Figure 3-7. WDS and TEM of InAs(ZnCdS) QDs. (a) The experimental values (with rms standard deviations) for the inorganic diameter of InAs(ZnCdS) by TEM and the S/As ratio as determined by wavelength dispersive spectroscopy (WDS). (b) Average of five WDS measurements (with rms standard deviations) for the elemental composition of the as synthesized InAs(ZnCdS) QDs.

(Figure 3-6.b). This indicates that the PEGylated shell contributes significantly to the overall diameter of the QDs. In order to further decrease the size, small molecule ligands such as D-penicillamine were used to achieve hydrodynamic diameters down to <5 nm. These ultra small InAs(ZnCdS) QDs were utilized for the imaging a multiple lymph nodes in pig animal models.

3.3 Biological Imaging

3.3.1 Cellular Labeling

In order to illustrate the utility of InAs(ZnCdS) QDs as targeted *in vitro* biological labels we ligand exchanged the QDs with the amine functionalized poly(amino-PEG₁₁)_{25%}-PIL polymer. The primary amines allow for streptavidin to be coupled to the QDs by a 1-ethyl-3-(3-dimethylaminopropyl) carbodiimide (EDC) coupling scheme to create a streptavidin-QD construct. We then transfected HeLa cells with a plasmid for yellow fluorescent protein (YFP), bound to an extracellular acceptor peptide (AP) tag^[15] and a transmembrane domain (TM) for cell surface targeting (AP-YFP-TM), as well as with a plasmid for endoplasmic reticulum-localized biotin ligase (BirA).^[14, 16, 17] The AP tag is specifically biotinylated by the co-expressed BirA and displayed on the cell surface as a fusion to YFP and the TM domain. Figure 3-8.a demonstrates that no non-specific cell interactions occur when biotin blocked streptavidin-QD conjugates are incubated with HeLa cells. In Figure 3-8.b co-localization of the YFP and NIR streptavidin-QD signal was observed, indicating targeting of streptavidin-QDs to the biotin presented at the cell membrane.

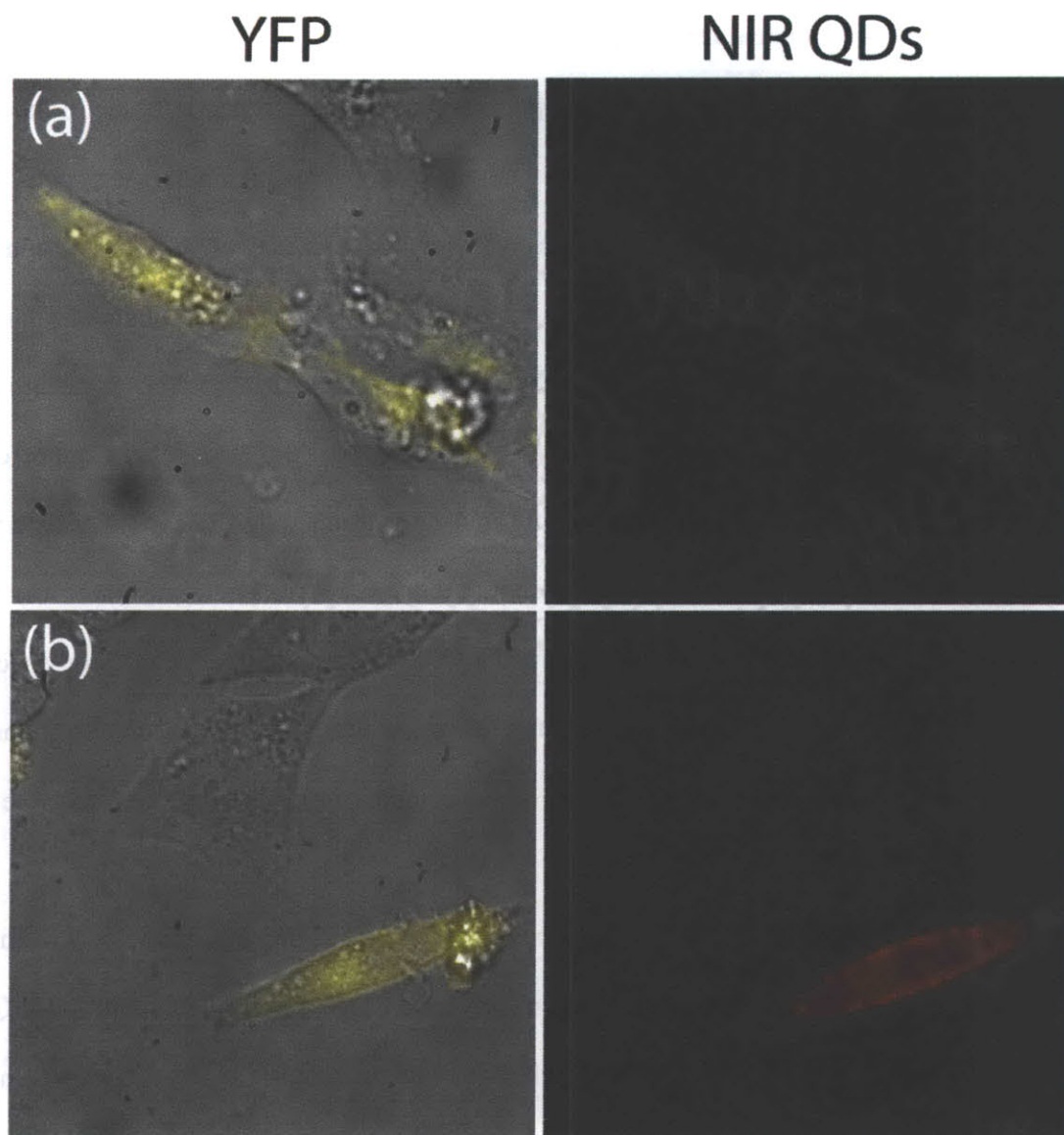


Figure 3-8. Cellular labeling. HeLa cells expressing yellow fluorescent protein (YFP) fused to a biotinylated peptide presented on the extracellular membrane. (a) Streptavidin-QDs pre-blocked with biotin did not bind to the cell surface whereas (b) non-blocked streptavidin-QDs are bound to the surface of YFP-expressing cells. (Figure courtesy J. M. Lee and W. Liu)

3.3.2 Multi-photon Biological Imaging

For *in vivo* applications, the minimal absorption and auto-fluorescence in tissue in the NIR region suggest utility for NIR QDs in intra-vital microscopy as high-contrast probes. We compared the effectiveness of green visible CdSe(CdS) and NIR InAs(ZnCdS) QDs as contrast agents for fluorescent angiography, *in vivo*, in a mouse model. We implanted mammary fat pad window chambers in female SCID mice to facilitate fluorescence microscopy in living mammary tissue using multi-photon microscopy (MPM).^[18] We implanted E0771 mammary tumor cells and allowed the tumors to grow to a diameter of 3 mm prior to imaging. Each QD sample was ligand exchanged with poly(PEG₁₂)-PIL, a polymer composed of PEG₁₂ (50 mol %) and imidazole (50 mol %), to achieve a HD <10 nm and a PEGylated surface to prevent non-specific binding (Figure 3-5).^[14] Using MPM, we adjusted the green and NIR QDs to concentrations of equal PL intensities *in vitro* and injected 200 μ L of this solution intravenously into the mouse via a bolus retro-orbital injection.

For comparative study, we collected grayscale images of a mammary tumor *in vivo* thirty minutes after intravenous injection of the green and NIR QDs (Figure 3-9). The NIR QDs clearly image deep vasculature up to 200 μ m, while the visible emitting QDs produce an image with poor vascular contrast and low PL intensity. Figure 3-9.a portrays a region of the tumor with low levels of auto-fluorescence and demonstrates rapidly decreasing vascular intensity with imaging depth for visible QDs, while the NIR QDs are intense even at 200 μ m as the emitted NIR light is absorbed less by the tissue than visible light. Figure 3-9.b is a region of the tumor where high levels of auto-fluorescence resulted in poor contrast even at superficial depths for the visible QDs while the NIR QDs show excellent contrast at all depths.

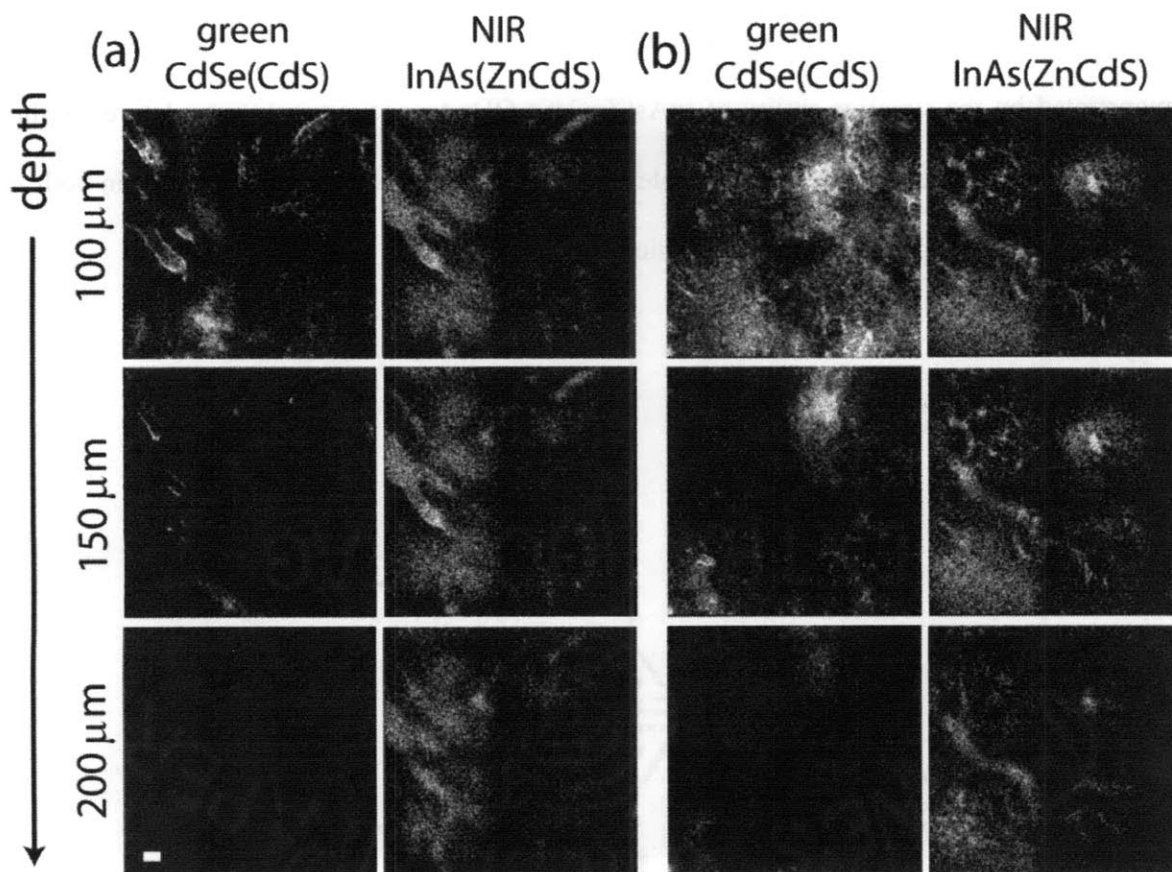


Figure 3-9. In vivo vasculature imaging. In vivo grayscale MPM images (a-b) of the vasculature in a mammary tumor in a mouse with CdSe(CdS) (green channel) and InAs(ZnCdS) (NIR channel) poly(PEG12)-PIL QDs injected intravenously and imaged simultaneously (scale bar, 100 μm). (Figure courtesy V. P. Chauhan)

3.4 Conclusions

In conclusion, we have prepared water soluble InAs(ZnCdS) QDs with bright and stable emission in the NIR. The NIR QDs can be functionalized to enable imaging of specific cellular proteins. In addition, the utility of the NIR region for *in vivo* biological imaging is clearly demonstrated by the superior ability of InAs(ZnCdS) QDs to image tumor vasculature. In this chapter, we have presented a compact, stable NIR QD fluorophore of potential utility in both *in vivo* and *in vitro* biological imaging applications.

3.5 Procedures

Materials: Indium acetate (99.99, Alfa Aesar), octadecene (90%, Sigma), myristic acid (Sigma), diethyl zinc (Strem), dimethyl cadmium (Strem), bis(trimethylsilyl)sulfide (Fluka), tris(trimethylsilyl)arsine (Nanomeps, France), tri-n-octylphosphine (97%, Strem), oleyl amine (Acros Organics), and all other reagents were obtained from Sigma. All solvents were spectrophotometric grade and purchased from EMD Biosciences. Oleyl amine was degassed under vacuum at 120 °C for two hours prior to use and stored over molecular sieves. Dimethyl cadmium and diethyl zinc were passed through a 20 nm filter prior to use. QD synthesis was performed using standard air free techniques on a nitrogen filled schlenk line. All glove-box manipulations were performed in an mBraun box (<0.1ppm oxygen).

InAs Core Synthesis: Prepared similarly as previously reported by Xie and Peng.^[3] 0.15 mmol of indium acetate, 0.45 mmol of myristic acid, and 3 ml of octadecene were added to a four neck 25 ml round bottom flask. The solution was heated to 100 °C under vacuum for one hour. The reaction mixture was then placed under nitrogen and heated to 150 °C. A solution of 0.125 mmol of tris(trimethylsilyl)arsine and 0.75 ml of tri-n-octylphosphine was prepared (under minimal lighting) in a nitrogen filled glovebox. This solution was then swiftly injected into the reaction flask and the temperature was increased to 230 °C for twenty minutes.

InAs(ZnCdS) Synthesis: After the synthesis of the InAs cores, the reaction flask was cooled to 170 °C and 3 ml of dry oleyl amine was injected (addition of over-coating precursors began *immediately* after the injection of amines. Caution must be exercised in the addition of primary

amines in III-V QD syntheses as primary amines have been shown to promote In_2O_3 formation at elevated temperatures when combined with Indium carboxylates).^[19] For shell growth, solution A was prepared by adding 1 mmol of bis(trimethylsilyl)sulfide to 10 ml of tri-n-octyl phosphine. Solution B was prepared by adding 0.34 mmol of dimethyl cadmium and 0.66 mmol of diethyl zinc to 10 ml of tri-n-octyl phosphine. Solution A and B were added simultaneously via syringe pump to the reaction flask at the rate of 1.5 ml/hour. The reaction was stopped when the peak photoluminescence reached ~ 800 nm.

CdSe(CdS) Synthesis: CdSe cores were synthesized according to previously reported procedures^[20-22] and were overcoated with a CdS shell. For pure CdS shells, we developed a successive ion layer adsorption and reaction (SILAR) procedure that is modified from those reported by Peng et al and Mews et al.^[23, 24] Briefly, CdSe cores with a first exciton feature at 491 nm were synthesized by heating a mixture of trioctylphosphine (TOP), trioctylphosphine oxide (TOPO), CdO (0.9 mmol), and tetradecylphosphonic acid (TDPA, 2.0 mmol) to 340 °C under nitrogen, removing evolved water *in vacuo* at 160 °C, re-heating to 360 °C under nitrogen, and rapidly introducing trioctylphosphine selenide (TOPSe, 3.4 mmol) in trioctylphosphine (TOP), followed by cooling to room temperature. Cores isolated by repeated precipitations from hexane with acetone were brought to 180 °C in a solvent mixture of oleylamine (3 mL) and octadecene (6 mL). Aliquots of Cd and S precursor solutions were then introduced alternately starting with the metal (Cd), waiting 15 min between the start of each addition. The Cd precursor consisted of 0.6 mmol Cd-oleate and 1.2 mmol decylamine in a solvent mixture of octadecene (3 mL) and TOP (3 mL). The S precursor consisted of 0.6 mmol hexamethyldisilathiane $[(\text{TMS})_2\text{S}]$ in 6 mL TOP. The dose of each over-coating precursor aliquot was calculated to provide a single

monolayer of ions to the QD surface. Addition of a total of 4 aliquots each of Cd and S yielded QDs with emission at 562 nm and a QY close to unity when diluted in hexane.^[14]

Synthesis of polymer ligands: The synthesis of the poly(PEG₁₂)-PIL and poly(aminoPEG₁₁)_{25%}-PIL ligands are reported in detail elsewhere.^[14]

Ligand exchange with poly(PEG₁₂)-PIL: QDs (2 nmol) were precipitated 1x using a mixture of acetone and butanol and brought into 50uL of CHCl₃. The QD stock solution was added to a solution of poly(PEG)-PIL (5 mg) in CHCl₃ (30uL), and stirred for 10 min at RT, after which 30 uL of MeOH was added followed by stirring for an additional 40 min. QD samples were precipitated by the addition of EtOH (30 μL), CHCl₃ (30 μL), and excess hexanes. The sample was centrifuged at 4000 g for 2 min, the supernatant discarded, and the pellet precipitated once more by the addition of EtOH, CHCl₃, and excess hexanes. After centrifugation and removal of the supernatant, the pellet was dried *in vacuo*, and PBS (500 μL, pH 7.4) was added, followed by filtration through a 0.2 μm filter.^[14]

Covalent conjugation of streptavidin to poly(aminoPEG₁₁)_{25%}. Commercial SA (50 uL, 10 mg/mL) was activated in MES buffer (pH 6.5) using Sulfo-NHS and EDC (20 eq.) for 20 min at RT. The activated SA was mixed with poly(aminoPEG₁₁)_{25%} QDs in sodium bicarbonate buffer at pH 8.4 at a SA:QD ratio of 5:1 and allowed to react for 1 hr. The samples were dialyzed 2x through a 50kDa MW cut-off spin concentrator and then used for labeling experiments.^[14]

Quantum Yields: QY of 800 nm emitting InAs(ZnCdS) QDs was measured relative to 1,1',3,3',3',3'-hexamethylindotrycarbocyanine iodide (HITC, QY = 26%) ($\lambda_{ex} = 680$ nm). Solutions of QDs in PBS and dye in methanol were optically matched at the excitation wavelength. QYs were calculated from the following expression: $QY_{QD} = QY_{Dye} \times (\text{Absorbance}_{dye} / \text{Absorbance}_{QD}) \times (\text{Peak Area}_{QD} / \text{Peak Area}_{Dye}) \times (n_{QD \text{ solvent}})^2 / (n_{Dye \text{ solvent}})^2$.

Transmission Electron Microscopy (TEM): TEM measurements were performed on a JEOL200CX microscope. The InAs(ZnCdS) QDs in water were dropped onto a Ted Pella ultra-thin carbon type A grid.

Wavelength Dispersive Spectroscopy (WDS): Samples were prepared by precipitating the QDs from solution three times with a mixture of hexanes, butanol, and acetone. The QDs were drop-cast onto doped silicon substrates and analyzed on a JEOL 8200 scanning electron microscope.

Gel Filtration Chromatography (GFC): GFC was performed using an ÄKTAprime Plus chromatography system from Amersham Biosciences equipped with a self-packed Superdex 200 10/100 column. PBS (pH 7.4) was used as the mobile phase with a flow rate of 1.0 mL/min. Detection was achieved by measuring the absorption at 280 nm.

Cell Labeling: HeLa cells were grown in DMEM (Mediatech) with 10% Fetal Bovine Serum (Invitrogen), 50 U/mL penicillin and 50 μ g /mL streptomycin (Invitrogen). Transfection plasmids were a kind gift from A.Ting (MIT, US). The cells were transfected using 1 μ l Lipofectamine 2000 (Invitrogen), 0.2 μ g of BirA-ER and 0.2 μ g of AP-YFP-TM per well of an

8-well chamber slide (LabTek). 1 mM biotin was added to the media during plasmid expression. Cells were imaged under 4°C PBS the day after transfection. 1% Bovine Serum Albumin (Sigma) was added to block non-specific binding during specific binding studies of ligand-coated quantum dots. Commercial BSA is known to contain biotin, and the stock BSA solution was dialyzed with a 3 kDa cutoff dialysis tube three times for 8 h in PBS pH 7.4, in 4°C. ^[14-17]

Intravital Microscopy: *In vivo* imaging was carried out using a custom-built multiphoton microscope (Olympus) with a Ti:Sapphire excitation laser (Mai-Tai HP, Spectra-Physics) and a 20x 0.95 NA water-immersion lens (Olympus). Mammary fat pad window chambers were implanted in female SCID mice as described previously E0771 mammary tumors were implanted in the mammary fat pad in these chambers, and were allowed to grow for two weeks until the tumors were roughly 3 mm in diameter and well-vascularized. ^[25] To determine appropriate concentrations for equal photoluminescence intensity for green visible CdSe(CdS) and NIR InAs(ZnCdS) QDs in solution, multiphoton imaging of mixed solutions of these QDs in glass microslides (VitreCom) was conducted. A mixture at these concentrations was then prepared, and 200uL of this solution was injected intravenously into the mouse via a bolus retro-orbital injection. An image mosaic was then collected for the entire tumor, at depths from 0-200 um into the tissue.

3.6 References

- [1] S. Kim, Y. T. Lim, E. G. Soltész, A. M. De Grand, J. Lee, A. Nakayama, J. A. Parker, T. Mihaljevic, R. G. Laurence, D. M. Dor, L. H. Cohn, M. G. Bawendi, J. V. Frangioni, *Nat Biotech* **2004**, *22*, 93.
- [2] M. Stroh, J. P. Zimmer, D. G. Duda, T. S. Levchenko, K. S. Cohen, E. B. Brown, D. T. Scadden, V. P. Torchilin, M. G. Bawendi, D. Fukumura, R. K. Jain, *Nat. Med.* **2005**, *11*, 678.
- [3] R. Xie, X. Peng, *Angew. Chem.* **2008**, *47*, 7677.
- [4] L. E. Brus, *J. Chem. Phys.* **1984**, *80*, 4403.
- [5] L. I. Berger, *Handbook of Chemistry and Physics* **2008**, 77.
- [6] A. Aharoni, T. Mokari, I. Popov, U. Banin, *J. Am. Chem. Soc.* **2005**, *128*, 257.
- [7] J. P. Zimmer, S. W. Kim, S. Ohnishi, E. Tanaka, J. V. Frangioni, M. G. Bawendi, *J. Am. Chem. Soc.* **2006**, *128*, 2526.
- [8] B. O. Dabbousi, J. Rodriguez-Viejo, F. V. Mikulec, J. R. Heine, H. Mattoussi, R. Ober, K. F. Jensen, M. G. Bawendi, *J. Phys. Chem. B* **1997**, *101*, 9463.
- [9] H. S. Choi, B. I. Ipe, P. Misra, J. H. Lee, M. G. Bawendi, J. V. Frangioni, *Nano Letters* **2009**, *9*, 2354.
- [10] Cao, U. Banin, *J. Am. Chem. Soc.* **2000**, *122*, 9692.
- [11] S.-W. Kim, J. P. Zimmer, S. Ohnishi, J. B. Tracy, J. V. Frangioni, M. G. Bawendi, *Journal of the American Chemical Society* **2005**, *127*, 10526.
- [12] D. R. Lide, *Vol. 84th ed. [Online]*, CRC Press: Boca Raton, FL, **2009**.
- [13] W. Liu, H. S. Choi, J. P. Zimmer, E. Tanaka, J. V. Frangioni, M. G. Bawendi, *J. Am. Chem. Soc.* **2007**, *129*, 14530.
- [14] W. Liu, A. B. Greytak, J. Lee, C. R. Wong, J. Park, L. F. Marshall, W. Jiang, A. Y. Ting, D. G. Nocera, D. Fukumura, R. K. Jain, M. G. Bawendi, *J. Am. Chem. Soc.* **2009**.
- [15] M. Howarth, K. Takao, Y. Hayashi, A. Y. Ting, *Proc Natl Acad Sci USA.* **2005**, *102*, 7583.
- [16] M. Howarth, A. Y. Ting, *Nature Protocols* **2008**, *3*, 534.
- [17] M. Howarth, W. Liu, S. Puthenveetil, Y. Zheng, L. F. Marshall, M. M. Schmidt, K. D. Wittrup, M. G. Bawendi, A. Y. Ting, *Nat Meth* **2008**, *5*, 397.

- [18] E. B. Brown, R. B. Campbell, Y. Tsuzuki, L. Xu, D. Carmeliet, D. Fukumura, R. K. Jain, *Nat. Med.* **2001**, *7*, 864.
- [19] M. Protiere, P. Reiss, *Chem. Commun.* **2007**, 2417.
- [20] C. B. Murray, D. J. Norris, M. G. Bawendi, *J. Am. Chem. Soc.* **1993**, *115*, 8706.
- [21] P. T. Snee, Y. Chan, D. G. Nocera, M. G. Bawendi, *Adv. Mater.* **2005**, *17*, 1131.
- [22] W. Liu, M. Howarth, A. B. Greytak, Y. Zheng, D. G. Nocera, A. Y. Ting, M. G. Bawendi, *J. Am. Chem. Soc.* **2008**, *130*, 1274.
- [23] R. Xie, U. Kolb, J. Li, T. Basche, A. Mews, *J. Am. Chem. Soc.* **2005**, *127*, 7480.
- [24] J. J. Li, Y. A. Wang, W. Z. Guo, J. C. Keay, T. D. Mishima, M. B. Johnson, X. G. Peng, *Journal of the American Chemical Society* **2003**, *125*, 12567.
- [25] B. J. Vakoc, R. M. Lanning, J. A. Tyrrell, T. P. Padera, L. A. Bartlett, T. Stylianopoulos, L. L. Munn, G. J. Tearney, D. Fukumura, R. K. Jain, B. E. Bouma, *Nat. Med.* **2009**, *advance online publication*.

Chapter 4. Control of Carrier Type in InAs Quantum Dots

4.1 Introduction

The doping of quantum dots has been an ongoing challenge in the field of colloidal QDs. A principle barrier is the so called ‘self-purifying’ mechanisms that occur during quantum dot growth.^[1-3] The difficulty of incorporating impurities into small crystals was theoretically explored by Turnbull as early as 1950.^[4] The difficulty of incorporating defects into QDs is due to the migration of impurities to grain boundaries, which in this case is the nanocrystal surface. As many quantum dots have diameters on the order of 2-10 nm, the diffusion of impurities along this length scale creates the ‘self-purification’ process. In addition, the introduction of a single impurity into a nanocrystal corresponds to a doping density of $\sim 10^{19}$ atoms/cm³, which corresponds to a very heavily doped bulk semiconductor.^[1]

Several synthetic approaches have been used to incorporate dopants in QDs. The precursors can be introduced during the core growth event in order to incorporate dopant atoms, and one of the earliest examples of this was Mn:ZnS nanocrystals.^[5] The dopant can also be introduced in the process of core-shell growth, and this has been demonstrated for Co:CdS diluted magnetic nanocrystals.^[6] Another approach is the post synthetic addition of fatty acid salts containing the dopant, the dopant atom is then incorporated into the nanocrystal core crystal lattice during a subsequent annealing step.^[7, 8] The presence of dopants in the QD crystal lattice has been confirmed by x-ray absorption fine structure measurements, magnetic circular dichroism, and electron paramagnetic resonance measurements.^[9-11]

The ability to control the carrier type and concentration in bulk semiconductors with high spatial resolution is necessary for creating functional semiconductor junctions, such as a p-n junction. The approach to doping bulk semiconductors is the introduction of impurities into the

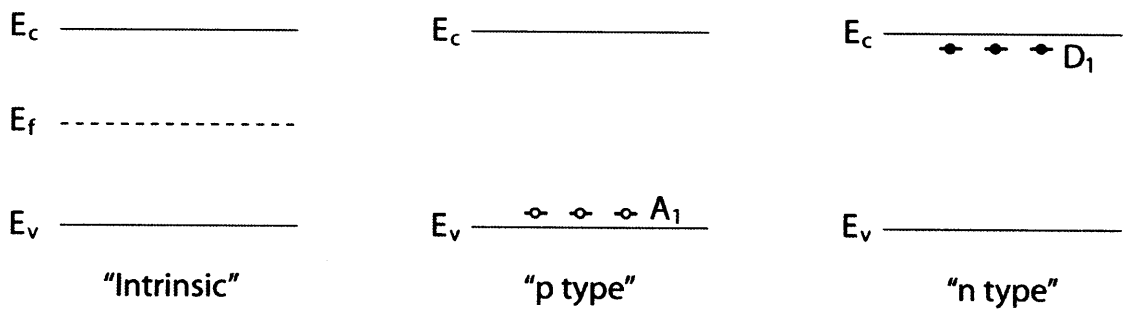


Figure 4-1. Schematic for donor and acceptor doping.

crystal lattice that act as either shallow acceptors (p type) or shallow donors (n type), as depicted in Figure 4-1. However, most QD devices are determined by the intrinsic carrier type and concentration in the as synthesized QDs. The most prominent junction used in QD photovoltaic devices is a simple Schottky junction between lead chalcogenide QDs and a metal contact.^[12-14] The control of carrier type and density in colloidal QDs remains a longstanding challenge, and a significant bottleneck in the development of QD devices.^[1]

Charge carriers to have been added to nanocrystal films by several previously reported methods.^[15-19] Cyclic voltammetry has been used to directly inject charges into films of nanocrystals.^[18, 19] Molecular sources of reactive sodium atoms have been added in the source of sodium biphenyl to CdSe nanocrystals, however the charge is reversible upon exposure to air.^[15, 20] Nanocrystal films of PbSe have been treated with hydrazine to switch the QDs from p to n type conductivity, however this carrier control is reversible upon evaporation of hydrazine from the particle surface.^[16] Remote doping of nanocrystal films has been achieved through binary superlattices of Ag₂Te and PbTe.^[17] However, none of these methods have produced a stable (pre-deposition) method to control carrier type and concentration in QDs.

In this Chapter, we seek to incorporate cadmium as an acceptor dopant into InAs nanocrystals. Through a solution based synthetic method we are able to add Cd, utilizing cadmium oleate [Cd(OA)₂], to the InAs QD surface. A high temperature annealing step (270 °C) is used to promote diffusion of the cadmium atoms into the crystal lattice. After annealing with Cd, the QDs were cast onto field effect transistor devices. We have observed the ability to switch InAs NC films from n-type to p-type conduction through the incorporation of Cd. The addition of Cd acceptor states may lead to a partially compensated semiconductor where the number of acceptors is greater than the number of donors, creating p type conductivity.

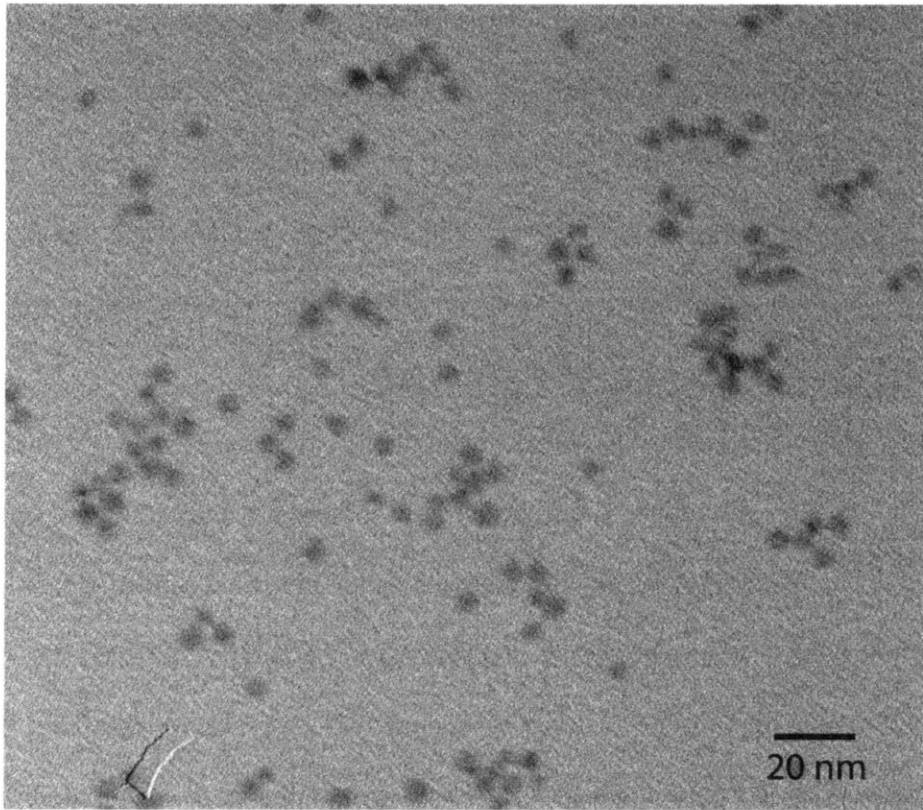


Figure 4-2. Transmission electron microscopy of 4 nm InAs QDs.

4.2 Cd Doped InAs Quantum Dots

4.2.1 Synthesis of InAs QDs

In Chapter 3, small InAs QDs were synthesized using indium myristate and tris(trimethylsilyl) arsine in a non-coordinating solvent of octadecene. In order to grow larger InAs cores, we adapted a synthetic method from work by the Alivisatos group utilizing indium chloride and tris(trimethylsilyl) arsine [(Me₃Si)₃As] in tri-n-octylphosphine (TOP).^[21] The initial core size is similar between the indium myristate [In(MA)₃] and the indium chloride (InCl₃) syntheses, however the indium chloride synthetic route has been previously shown to accommodate multiple injections of (Me₃Si)₃As.

The synthesis of InAs QDs is dominated by the ripening of InAs clusters and nanocrystals, as the molecular (Me₃Si)₃As precursor quantitatively reacts at room temperature with InCl₃ to form InAs clusters and trimethylsilyl chloride. At elevated temperatures these InAs clusters ripen into a moderately narrow size distribution of InAs QDs, as shown by TEM in Figure 4-2, and a well defined first absorption feature in Figure 4-3. It should be noted that the In(MA)₃ synthetic route can also be modified to accommodate multiple injections to grow larger InAs QDs (Figure 4-4). In order to prevent inhomogeneous growth of the QDs, the reaction must be thermally cycled. The reaction flask was cooled to room temperature for each subsequent (Me₃Si)₃As injections, and this was done drop-wise with rigorous stirring. The reaction flask was then heated to 300 °C for ripening of the InAs nanocrystals.

Larger InAs cores were targeted to facilitate the transport of charge in nanocrystal films. In addition, narrower bandgap InAs QDs that absorb light in the infrared region are of potential utility as photodectors or photovoltaics.

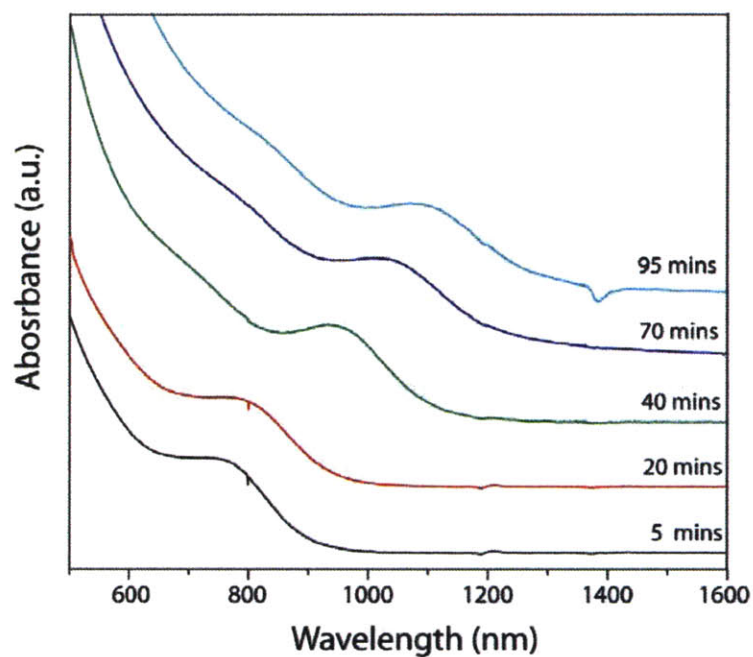


Figure 4-3. Growth of InAs QDs with multiple injections from InCl_3 and $(\text{Me}_3\text{Si})_3\text{As}$.

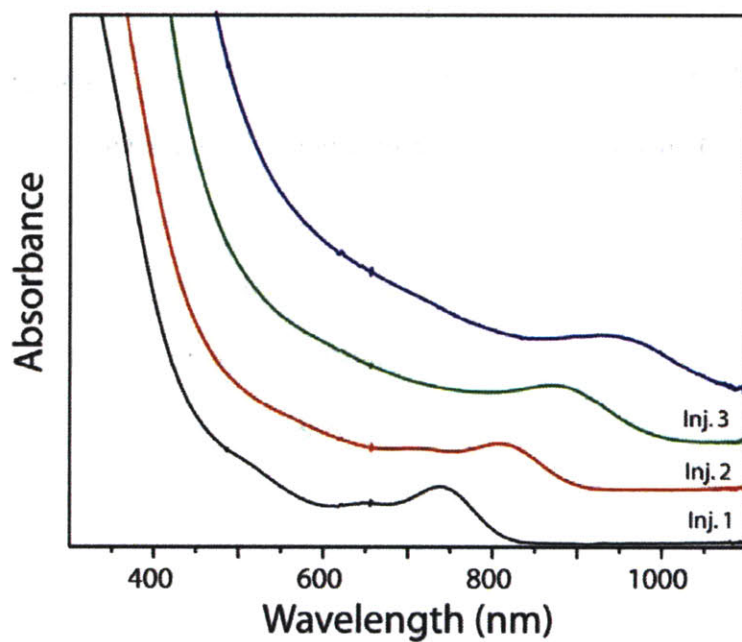


Figure 4-4. Growth of InAs QDs with multiple injections from $\text{In}(\text{MA})_3$ and $(\text{Me}_3\text{Si})_3\text{As}$.

4.2.2 Synthesis of Cd:InAs QDs

The introduction of Cd onto the InAs QD surface is performed as a two step process. The InAs cores are first purified by precipitation in an inert glovebox with anhydrous solvents. The InAs cores are then dispersed into a mixture of oleyl amine and octadecene. Cadmium oleate [Cd(OA)₂] is then introduced to the reaction mixture at a concentration corresponding to one monolayer of cadmium atoms on the nanocrystal surface. After adding the Cd(OA)₂ an increase in photoluminescence is observed, likely due to the passivation of surface traps. The QDs are then thermally annealed by gradually heating to 270 °C. At elevated temperature the Cd atoms likely begin to diffuse into the InAs lattice, as depicted in Figure 4-5. The synthetic approach of adding dopant atoms in the form of carboxylates, to the QD surface, has been successfully used to synthesize Cu:InP and Mn:ZnSe QDs previously.^[8, 22]

4.2.3 Optical Properties

Figure 4-6 is the absorption spectra of Cd:InAs QDs as a function of annealing temperature. At temperatures below 200 °C, the absorption features are identical to those of the InAs core QDs. As the temperature is raised above 250 °C, the first absorption feature begins to broaden. A bleach of the first absorption feature has been previously observed in heavily doped CdSe QDs.^[15] We do not observe a dramatic bleaching event, however the broadening of the electronic transitions may correlate with the introduction of acceptor dopants into the crystal lattice, as is observed in the p type behavior in the following field effect transistors (FETs). The red shift with addition of Cd at high temperature has been previously observed by the Banin group, and they have shown this red shift is not due to a ripening of the size distribution.^[23]

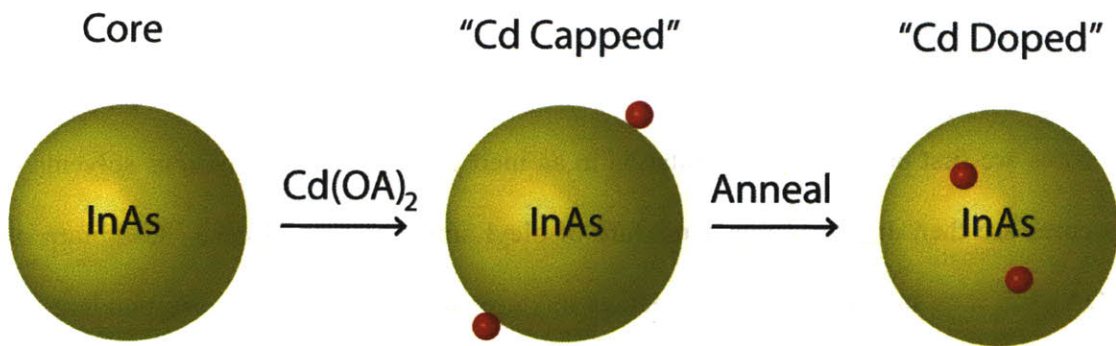


Figure 4-5. Schematic for doping InAs QDs with Cd.

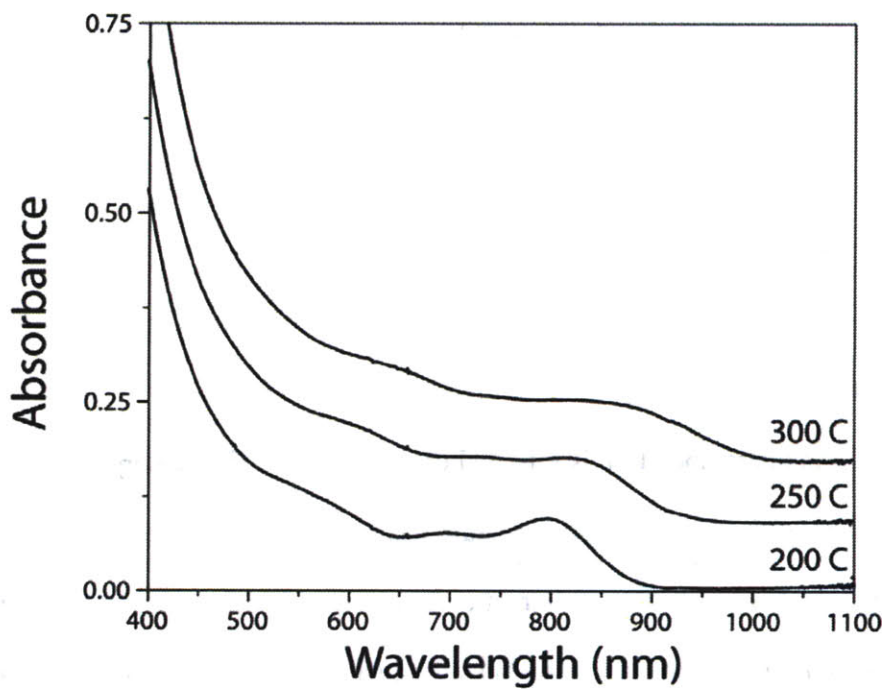


Figure 4-6. Absorbance spectra of InAs QDs with Cd(OA)_2 as a function of temperature.

4.2.4 Field Effect Transistors

In the bulk, InAs is typically n type due to surface state pinning of the Fermi level above the conduction band.^[24] In addition, the surface states also lead to a Fermi level pinning at the metal contact, resulting in the formation of ohmic contacts between InAs many different electrode metals. Passivation of the surface by sulfur containing molecules has been previously shown to reduce contact resistance and improve mobility in InAs nanowires.^[25] For these reasons, ethanedithiol was used as a post deposition ligand treatment.^[26-28]

While operating in a FET geometry, the as grown InAs QDs exhibit n type conductivity, as indicated in Figure 4-7.a-b. The switch to p type conductivity is observed in the Cd:InAs QDs as shown in Figure 4-7.c-d. This behavior is attributed to the generation of excess acceptor states through the incorporation of Cd. The explanation most consistent with bulk semiconductor physics is that the Cd is occupying an In lattice position (Cd_{In}) and acting as an acceptor defect, causing the material to have p-type carriers. An alternate explanation is that the Cd atoms act to alter the surface states of the InAs QDs, such that the surface states begin to act as acceptors rather than donors. As QDs have exceedingly large surface areas, the contribution of surface states in the observed conductivity behavior cannot be overlooked, and the modulation of surface states may also provide effective routes to controlling carrier type and concentration.

EDS and ICP-AES were used to determine the amount of Cd present in the purified InAs:Cd QDs. These measurements gave relative concentrations of In:As:Cd of 2.0:2.2:1.0 and 1.9:2.4:1 respectively. From the lattice constant of InAs and the 4 nm diameter of the QDs, we estimate that there are ~600 In and ~600 As atoms per NC, and that a monolayer of Cd atoms on the surface of the NC would add ~320 Cd atoms. This gives a relative concentration of 1.9:1.9:1, in good agreement with the observed ratios if an As rich surface is assumed.^[23]

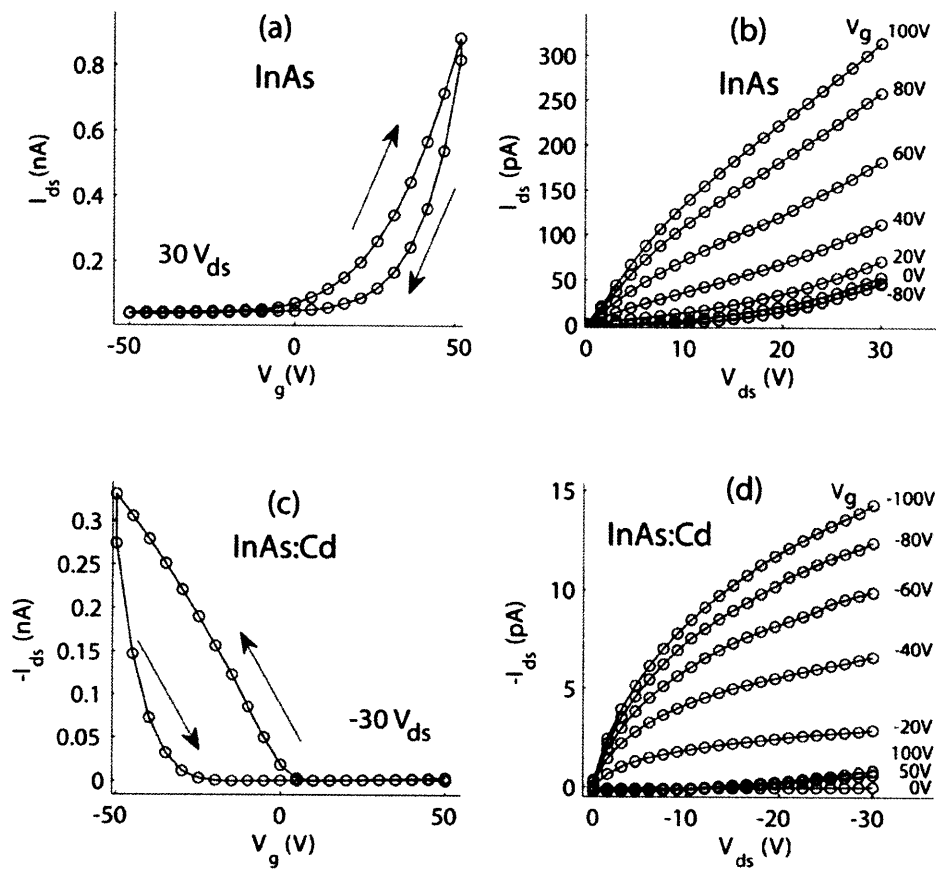


Figure 4-7. FET devices for InAs and InAs:Cd QDs. (figure courtesy S. Geyer)

4.3 p-n Hetero-junction Quantum Dot Device

As discussed in the introduction, the most prominent junction used in QD photovoltaic devices is a simple Schottky junction between lead chalcogenide QDs and a metal contact.^[12-14] However, a Schottky device geometry is typically not utilized for functional photovoltaic or LED devices.^[29-31] Of the most widely utilized QDs in devices, CdSe is typically intrinsic (no free carriers), and the lead chalcogenides are typically p type.^[32, 33] The n type behavior of InAs QDs opens up the possibility for forming p-n junctions in combination with p type QD materials. The use of p type Cd:InAs QDs to form a p-n homo-junction would be the ideal device geometry. However, as can be observed in Figure 4-7.d, the Cd:InAs QD films do not exhibit substantial conductivity at $V_g = 0$ V. The low conductivity of the Cd:InAs QD films complicates the fabrication of p-n homo-junction device.

For the reasons discussed above, we have pursued the fabrication of p-n hetero-junction device between p type PbS and n type InAs QDs. The electrode contact for PbS QDs was selected as indium tin oxide (ITO) as this has been previously shown to form ohmic contacts with PbS QDs.^[12] The electrode contact for InAs QDs was selected as aluminum, as InAs typically forms ohmic contacts with metal electrodes as previously discussed. The p-n junction lies at the interface of the p type PbS QDs and the n type InAs QDs (Figure 4-8).

The current-voltage (I-V) characteristics in Figure 4-9 indicate diode behavior in the dark I-V sweeps. When run under illumination, the device exhibits a turn on voltage of 0.33 V and short circuit current density of 0.0273 mA/cm^2 . The current levels are likely limited by the InAs QD layer, as the conductivity in the InAs QD films is far less than in PbS films.

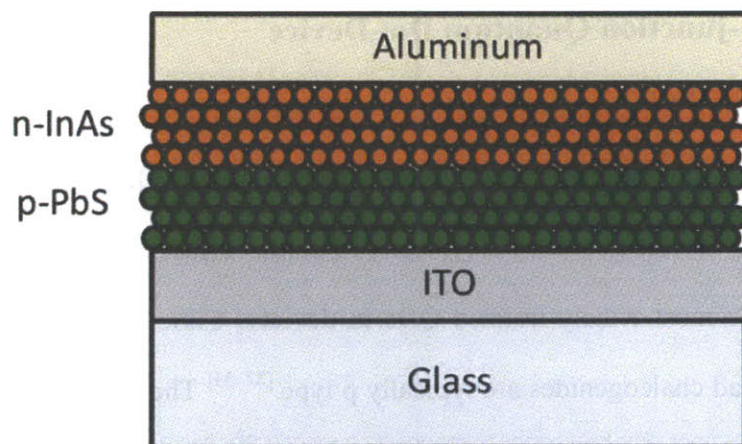


Figure 4-8. InAs (Orange) and PbS (Green) heterostructure device.

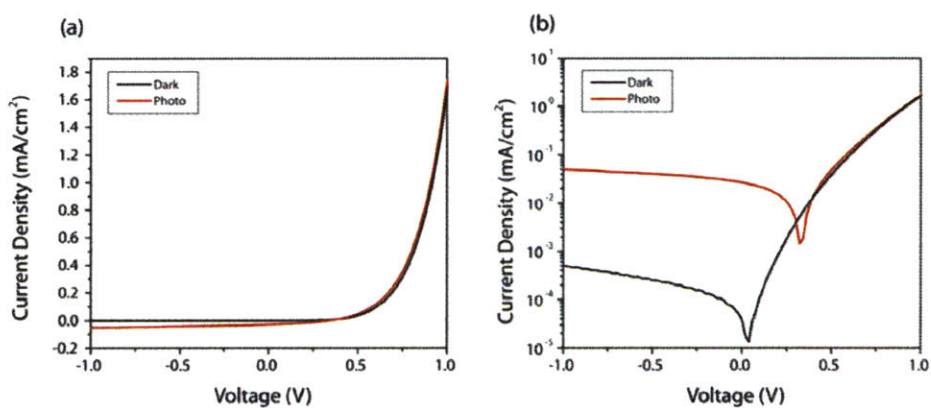


Figure 4-9. I-V Characteristics of PbS/InAs heterostructure device. (a) I-V plot demonstrating diode behavior in the dark and photo currents and (b) log-linear plot demonstrating that the $V_{oc} = 0.33$ V.

4.4 Implications for Quantum Dot Devices

The current limitations in bilayer (analogous to a thin film device) QD photovoltaics can be discussed in the context of two challenges (1) is the formation of large built in electric field gradients for the separation of charge and (2) is the subsequent transport of charge across the QD film. The first challenge will likely not be solved through a continuation of fabricating Schottky based devices. The cutting edge Schottky devices have utilized impractical metal contacts (such as calcium) in an effort to create large built in potentials, however even these electrodes produce depletion widths of less than a few hundred microns.^[12] In order to create larger depletion widths for efficient charge separation, more traditional junctions (such as a p-n junction) may provide a solution. The second challenge in QD device operation is the transport of free carriers, which is a very significant issue as QD films are currently have exceedingly low carrier mobilities. Recent developments, such as the use of compact inorganic zintl ions as surface ligands have produced QD films with increased mobilities.^[33] However, the chalcogenide zintl surface ligands leave behind a thin inorganic film, such as SnS₂, and the effects of such an inorganic impurity on device operation has yet to be explored.

In order to address the current challenges in fabricating QD thin film devices, aggressive efforts in the synthetic development of new QD materials, new QD surface ligands, and alternative device geometries must be explored in order to potentially provide device solutions.

4.5 Methods

Chemicals: tri-n-octylphosphine (97%, Strem), tris(trimethylsilyl)arsine (Nanomeps, France), Indium chloride (99.999%, alfa aesar), oleic acid (alfa aesar), octadecene (90%, Sigma), diethyl zinc (Strem), cadmium oxide (alfa aesar), oleyl amine (Acros Organics). All manipulations were performed in a nitrogen filled glovebox or schlenk line using standard air-free procedures.

InAs Core Synthesis: A stock solution of InCl_3 in tri-n-octylphosphine (TOP) was prepared by adding 3 grams of InCl_3 to 10 ml of TOP and heating to 270 °C for one hour. To 1 ml of the InCl_3 stock solution was added 100 mg of tris(trimethylsilyl)arsine $[(\text{TMS})_3\text{As}]$, the resulting solution was injected into a rapidly stirring solution of 3.5 ml TOP at 300 °C. The temperature was lowered to 270 °C for growth of the InAs cores and subsequent injections. Secondary injections took place at 25 minutes, 50 minutes, and 75 minutes. Each secondary injection consisted of 100 mg of $(\text{TMS})_3\text{As}$ in 1 ml of TOP.

Cd:InAs Synthesis: 2 ml of growth solution from the InAs core synthesis was purified by addition of anhydrous butanol and ethanol and subsequent centrifugation in an inert glove box. The InAs cores were redispersed in 2 ml of anhydrous hexanes. The solution of InAs cores was injected into a dry solution of 4 ml octadecene and 1.5 oleyl amine. This solution was degassed at 60 °C for 30 minutes and then degassed at 100 °C for one hour. A stock solution of 0.04M cadmium oleate in octadecene was injected into the reaction mixture and the solution was subsequently heated to 270 °C for one hour.

4.6 References

- [1] D. J. Norris, A. L. Efros, S. C. Erwin, *Science* **2008**, *319*, 1776.
- [2] G. M. Dalpian, J. R. Chelikowsky, *Physical Review Letters* **2006**, *96*, 226802.
- [3] S. C. Erwin, L. Zu, M. I. Haftel, A. L. Efros, T. A. Kennedy, D. J. Norris, *Nature* **2005**, *436*, 91.
- [4] D. Turnbull, *Journal of Applied Physics* **1950**, *21*, 1022.
- [5] R. N. Bhargava, D. Gallagher, X. Hong, A. Nurmikko, *Physical Review Letters* **1994**, *72*, 416.
- [6] P. V. Radovanovic, D. R. Gamelin, *Journal of the American Chemical Society* **2001**, *123*, 12207.
- [7] N. Pradhan, X. Peng, *Journal of the American Chemical Society* **2007**, *129*, 3339.
- [8] R. Xie, X. Peng, *Journal of the American Chemical Society* **2009**, *131*, 10645.
- [9] D. M. Hoffman, B. K. Meyer, A. I. Ekimov, I. A. Merkulov, A. L. Efros, M. Rosen, G. Couino, T. Gacoin, J. P. Boilot, *Solid State Communications* **2000**, *114*, 547.
- [10] D. J. Norris, N. Yao, F. T. Charnock, T. A. Kennedy, *Nano Letters* **2000**, *1*, 3.
- [11] D. Chen, R. Viswanatha, G. L. Ong, R. Xie, M. Balasubramanian, X. Peng, *Journal of the American Chemical Society* **2009**, *131*, 9333.
- [12] J. M. Luther, M. Law, M. C. Beard, Q. Song, M. O. Reese, R. J. Ellingson, A. J. Nozik, *Nano Letters* **2008**, *8*, 3488.
- [13] T. S. Mentzel, V. J. Porter, S. Geyer, K. MacLean, M. G. Bawendi, M. A. Kastner, *Physical Review B (Condensed Matter and Materials Physics)* **2008**, *77*, 075316.
- [14] E. H. Sargent, *Nat Photon* **2009**, *3*, 325.
- [15] M. Shim, P. Guyot-Sionnest, *Nature* **2000**, *407*, 981.
- [16] D. V. Talapin, C. B. Murray, *Science* **2005**, *310*, 86.
- [17] J. J. Urban, D. V. Talapin, E. V. Shevchenko, C. R. Kagan, C. B. Murray, *Nature Materials* **2007**, *6*, 115.
- [18] D. Yu, C. J. Wang, P. Guyot-Sionnest, *Science* **2003**, *300*, 1277.
- [19] B. L. Wehrenberg, P. Guyot-Sionnest, *Journal of the American Chemical Society* **2003**, *125*, 7806.

- [20] J. Bang, B. Chon, N. Won, J. Nam, T. Joo, S. Kim, *Journal of Physical Chemistry C* **2009**, *113*, 6320.
- [21] A. A. Guzelian, U. Banin, A. V. Kadavanich, X. Peng, A. P. Alivisatos, *Appl. Phys. Lett.* **1996**, *69*, 1432.
- [22] N. Pradhan, D. Goorskey, J. Thessing, X. Peng, *Journal of the American Chemical Society* **2005**, *127*, 17586.
- [23] S. M. Geyer, P. M. Allen, L. Y. Chang, T. P. Osedach, N. Zhao, V. Bulovic, M. G. Bawendi, **2010**, *Manuscript submitted*.
- [24] M. Noguchi, K. Hirakawa, T. Ikoma, *Physical Review Letters* **1991**, *66*, 2243.
- [25] Q. Hang, F. Wang, P. D. Carpenter, D. Zemlyanov, D. Zakharov, E. A. Stach, W. E. Buhro, D. B. Janes, *Nano Letters* **2007**, *8*, 49.
- [26] P. Guyot-Sionnest, C. Wang, *The Journal of Physical Chemistry B* **2003**, *107*, 7355.
- [27] M. V. Jarosz, V. J. Porter, B. R. Fisher, M. A. Kastner, M. G. Bawendi, *Physical Review B* **2004**, *70*.
- [28] E. J. D. Klem, D. D. MacNeil, P. W. Cyr, L. Levina, E. H. Sargent, *Applied Physics Letters* **2007**, *90*, 183113.
- [29] K. Ramanathan, G. Teeter, J. C. Keane, R. Noufi, *Thin Sol. Films* **2005**, *480-481*, 499.
- [30] T. Buonassisi, A. A. Istratov, M. A. Marcus, B. Lai, Z. Cai, S. M. Heald, E. R. Weber, *Nat Mater* **2005**, *4*, 676.
- [31] A. Tsukazaki, A. Ohtomo, T. Onuma, M. Ohtani, T. Makino, M. Sumiya, K. Ohtani, S. F. Chichibu, S. Fuke, Y. Segawa, H. Ohno, H. Koinuma, M. Kawasaki, *Nat Mater* **2005**, *4*, 42.
- [32] K. S. Leschkies, T. J. Beatty, M. S. Kang, D. J. Norris, E. S. Aydil, *ACS Nano* **2009**, *3*, 3638.
- [33] M. V. Kovalenko, M. Scheele, D. V. Talapin, *Science* **2009**, *324*, 1417.

Chapter 5. Mechanistic Insights into the Formation of InP Quantum Dots

5.1 Introduction

In this chapter, we present a mechanistic exploration of colloidal III-V InP quantum dot (QD) syntheses.^[1-3] InP QDs are of increasing technological interest as a replacement for CdSe QDs in visible light applications. However, the synthetic methodology for InP QDs has not produced QDs with narrow size distributions relative to CdSe and PbSe QDs.^[1-6] Studies of the molecular mechanisms involved in the formation of QDs have only recently been reported for II-VI CdSe and IV-VI PbSe QDs.^[7, 8] As for InP QDs, the molecular mechanisms underlying QD formation are essentially unknown. We investigated the reactions involved in InP QD formation in order to understand the broad size distributions in current InP QD syntheses.

In a simplified view of the formation of monodisperse colloids two general events should occur; (i) an initial nucleation of colloids followed by (ii) subsequent growth of these nuclei from molecular precursors.^[9, 10] Studies on the growth of CdSe and PbSe QDs have shown these systems fulfill (i) and (ii).^[7, 8] For InP QDs, we have found that molecular phosphorus precursors are completely depleted following InP nucleation, indicating that subsequent QD growth is due exclusively to ripening from non-molecular InP species. The inability of InP QD syntheses to satisfy (ii), due to depletion of molecular precursors, may explain the broad size distributions of InP QDs relative to CdSe or PbSe QDs.

Colloidal InP QDs are synthesized by the injection of precursors into a hot solution of surfactants, or by mixing precursors at room temperature (RT) followed by heating.^[1-3] In these reactions, indium myristate $[\text{In}(\text{MA})_3]$ reacts with tris(trimethylsilyl) phosphine $[(\text{TMS})_3\text{P}]$ to produce TMS-myristate (TMS-MA) and InP QDs (Figure 5-1, overall). By operating at

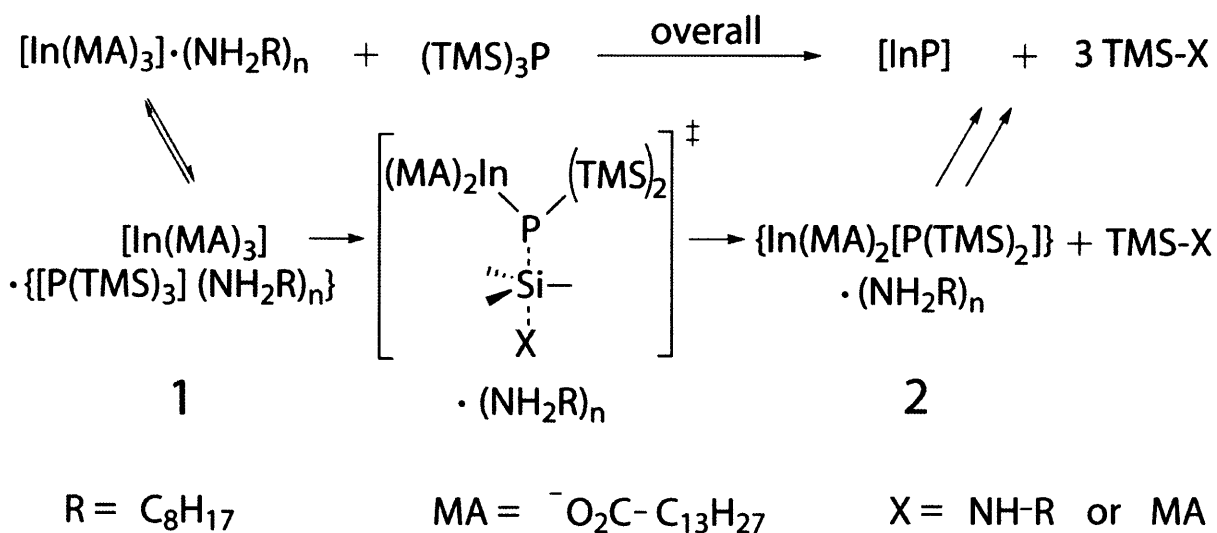


Figure 5-1. Proposed mechanistic pathway for amine-inhibited InP synthesis.

reduced temperatures, with amines, it is possible to monitor the evolution of molecular species during InP formation. We have found that primary amines inhibit the rate of $(\text{TMS})_3\text{P}$ depletion, contrary to previous claims.^[2, 11-14]

5.2 Mechanistic Studies

5.2.1 Proposed Mechanism

Figure 5-1 presents the proposed reaction mechanism for an amine-inhibited InP QD synthesis. Initially, $\text{In}(\text{MA})_3$ is coordinated to the Lewis base octylamine (OA). The approach of $(\text{TMS})_3\text{P}$ is depicted in the first step equilibrium of the octylamine coordinated indium species and the $(\text{TMS})_3\text{P}$ coordinated indium species, labeled complex 1. 1 goes on to lose a myristate ligand and subsequently forms an In-P bond while losing a TMS group, potentially forming the proposed molecular intermediate labeled complex 2. The molecular In and P species react further to form [InP] nanocrystals, and there may be other reaction pathways to [InP] not depicted in this scheme. Experimental evidence supporting this proposed mechanism is presented in the following sections.

5.2.2 ^1H NMR Studies for Literature Reports

In order to probe the evolution of molecular species during InP QD synthesis, we utilized ^1H NMR spectroscopy to investigate species containing trimethylsilyl (TMS) groups. Under the reported reaction conditions, the TMS group is the most probable ligand for molecular phosphines. Therefore, the high ^1H NMR sensitivity of the TMS groups permits the facile observation of any P-containing molecules or decomposition products present at relatively significant concentrations. Reactions were performed in J-young NMR tubes containing $\text{In}(\text{MA})_3$, $(\text{TMS})_3\text{P}$, octylamine, and diphenylmethane as an internal standard, in dry toluene- d_8 .

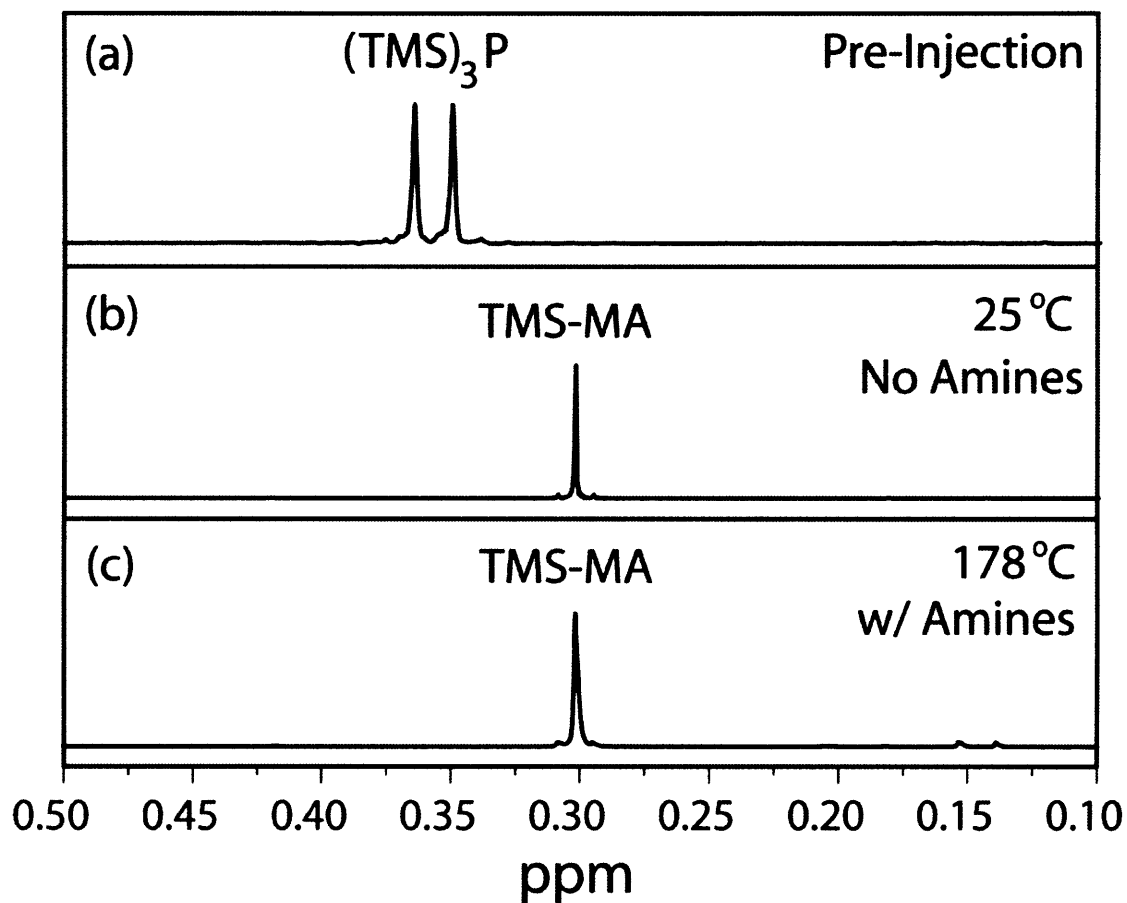


Figure 5-2. ^1H NMR spectra of (a) $(\text{TMS})_3\text{P}$ at 20 °C before injection, (b) reaction mixture of $\text{In}(\text{MA})_3$ and $(\text{TMS})_3\text{P}$ in toluene- d_8 three minutes after mixing at 25 °C, and (c) reaction mixture of $(\text{TMS})_3\text{P}$ and 6:1 octylamine: $\text{In}(\text{MA})_3$ in 1,2-dichlorobenzene- d_4 after heating at 178 °C for one minute. Both (b) and (c) demonstrate quantitative conversion of $(\text{TMS})_3\text{P}$ to TMS-MA shortly after the reactions are initiated.

In the absence of octylamine, a ^1H NMR spectrum taken within three minutes of mixing $\text{In}(\text{MA})_3$ and $(\text{TMS})_3\text{P}$ at $25\text{ }^\circ\text{C}$ showed quantitative conversion of $(\text{TMS})_3\text{P}$ to TMS-MA (Figure 5-2.a-b). The rapid decomposition of $(\text{TMS})_3\text{P}$ is likely due to the direct approach of $(\text{TMS})_3\text{P}$ to the In center, circumventing the octylamine-indium equilibrium en route to the production of a stable Si-O bond (TMS-MA). The fast conversion of $(\text{TMS})_3\text{P}$ to TMS-MA at $25\text{ }^\circ\text{C}$ occurs on a time-scale that is not practical for monodisperse QD synthesis or kinetic analysis by NMR.^[7-10]

For literature procedures at elevated temperatures containing octylamine, we find no molecular precursors remain shortly after reaction initiation at high temperature. A sealed NMR tube with a composition similar to those previously reported was heated at the published reaction temperature ($178\text{ }^\circ\text{C}$)^[2] and showed no $(\text{TMS})_3\text{P}$ after 1 minute (Figure 5-2.c). Our findings, with and without octylamine, demonstrate that previously reported reaction conditions for InP QDs are based on ripening of non-molecular InP species, similar to those used for InAs,^[15] and do not fulfill the requirements for the formation of monodisperse colloids.

5.2.3 ^1H NMR Molecular Precursor Evolution

When octylamine containing InP reaction mixtures were run at reduced temperatures ($<75\text{ }^\circ\text{C}$), the reaction proceeded sufficiently slow to allow kinetic analysis. From the time-resolved ^1H NMR spectra in Figure 5-3.a, four species account for 100% of all TMS groups. $(\text{TMS})_3\text{P}$ and TMS-MA together account for over 90% of all TMS groups; the remaining TMS groups are either associated with the intermediate **2** (Figure 5-3.a, inset) or the silylated octylamine (TMS-OA) that occurs with $< 5\%$ yield. The relative rates of $(\text{TMS})_3\text{P}$ depletion and of TMS-MA growth are consistent with the near quantitative conversion of $(\text{TMS})_3\text{P}$ to TMS-MA (Figure 5-3.b), indicating this is the dominant reaction pathway to the formation of InP QDs.

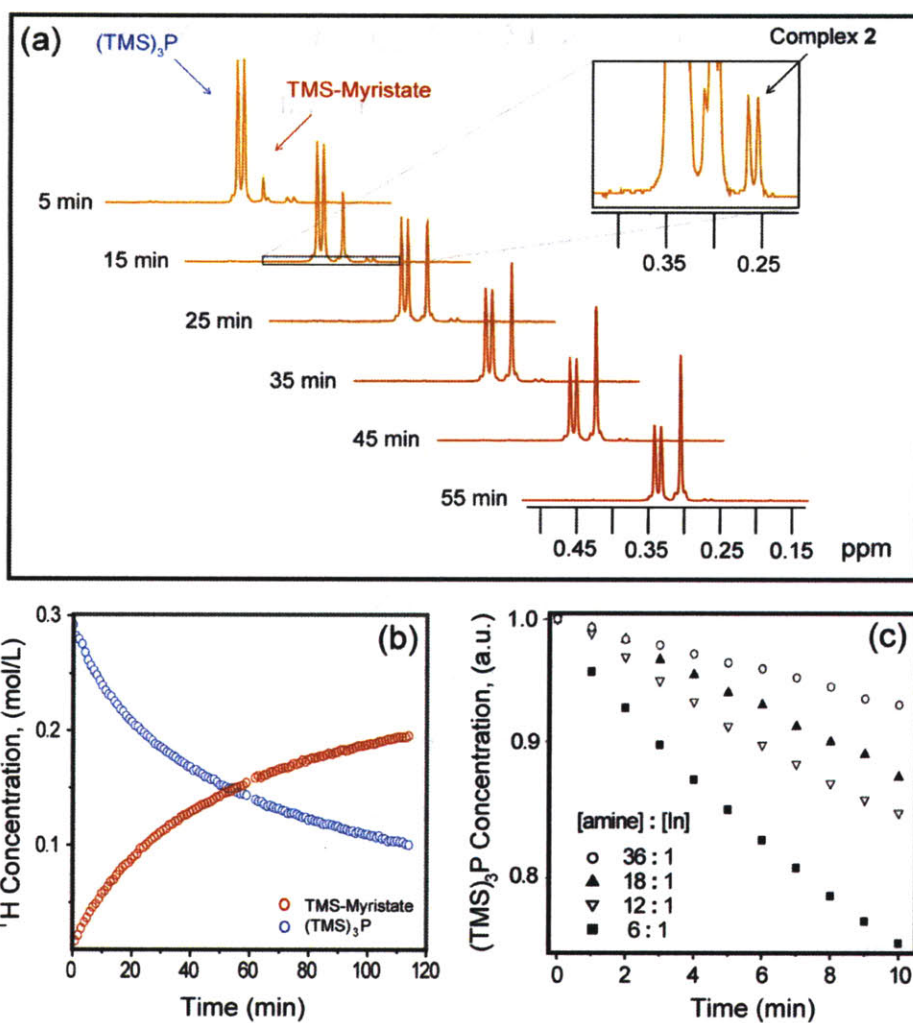


Figure 5-3. (a) Time-resolved ^1H NMR spectra at 40°C , showing evolution of $(\text{TMS})_3\text{P}$ and TMS-myristate (TMS-MA) resonances during standard conditions for InP QD synthesis with amines. Inset: Detail of 15-minute ^1H NMR spectrum. We propose the doublet at 0.26 ppm corresponds to 2. (b) Concentration profiles of $(\text{TMS})_3\text{P}$ and TMS-MA protons, determined with one minute resolution via the integration of spectra represented in (a). (c) Concentration profiles of $(\text{TMS})_3\text{P}$ for InP QD syntheses with varying amine concentrations at 40°C , normalized at initial time. The reaction rate decreases with increasing amine concentration. The reactions without amines reached completion too rapidly to be resolved by ^1H NMR.

We propose that the doublet at $\delta = 0.26$ ppm in the ^1H NMR corresponds to **2** as noted above. The doublet is split by 4.4 Hz (consistent with ^{31}P - ^1H 3-bond coupling),^[16] which suggests a P-containing species that retains at least one TMS group. The ^1H NMR resonance of **2** has a line-width comparable to that of molecular $(\text{TMS})_3\text{P}$ and TMS-MA, indicating that the species has a distinct molecular structure. In addition, the time evolution of **2** shows the characteristic growth and depletion of an intermediate (Figure 5-5).

Upon increasing the octylamine concentration from 6:1 to 18:1 the rate of $(\text{TMS})_3\text{P}$ depletion continued to decrease (Figure 5-3.c); thus amines inhibit, rather than activate,^[2, 11-14] InP synthesis. As a change in amine ratio influences the rate even at high concentrations, and as the rates do not have a clear power dependence on octylamine concentration in either this or prior studies,^[14] the amine likely does not have a well-defined stoichiometry during the rate-determining step. At octylamine:In ratios greater than 18:1 we observed a diminishing change in the rate with added amine. The high octylamine content reactions also yielded an increase in the TMS-OA product, complicating kinetic analysis.

No evidence was found for the formation of significant quantities of other molecular phosphorus species, such as P-H containing species. Only two resonances were detected by ^{31}P NMR, and these resonances correspond to $(\text{TMS})_3\text{P}$ and **2** (Figure 5-4). When monitoring the depletion of $(\text{TMS})_3\text{P}$ at various octylamine concentrations, we observe no doublets in the ^1H NMR that would indicate the formation of P-H species, indicating the formation of P-H species is not a significant pathway in the decomposition of $(\text{TMS})_3\text{P}$. The formation of P-H species, and accelerated decomposition of [InP] clusters was previously observed with the addition of methanol and this finding has been assumed to also occur with the addition of primary amines in the literature; however, we do not observe this to be a significant pathway.^[2, 11-14]

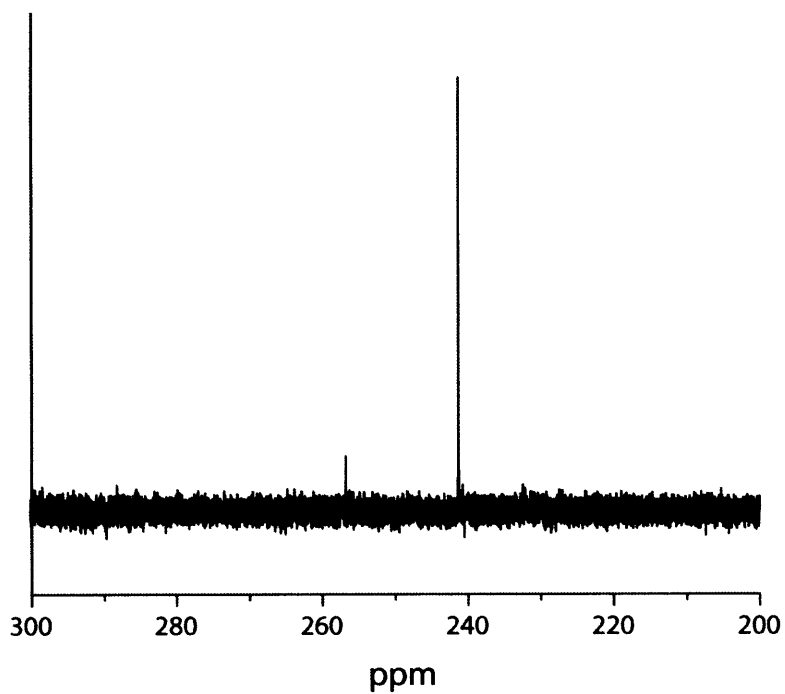


Figure 5-4. ^1H -decoupled ^{31}P spectrum for the InP reaction mixture after 30 min at 25 °C. Only resonances for $(\text{TMS})_3\text{P}$ (241.3 ppm) and **2** (256.8 ppm) are visible. Chemical shifts are referenced to 85% H_3PO_4 (0 ppm).

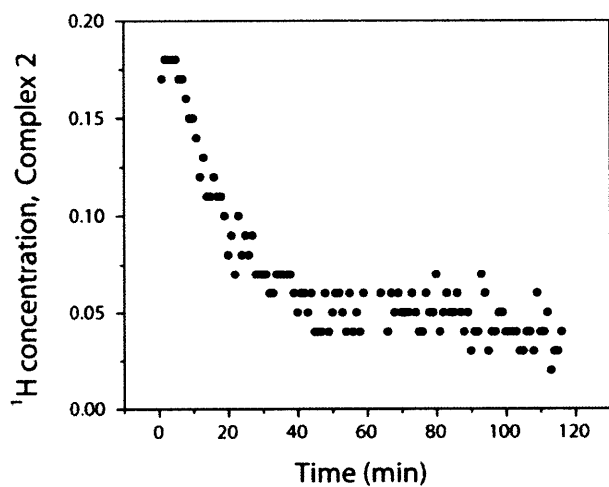


Figure 5-5. ^1H NMR concentration of complex **2** during synthesis at 40 °C. The rise and fall of Complex **2** over time is consistent with the assignment of complex **2** as an intermediate in the formation of InP QDs.

5.2.4 Eyring Analysis

In order to probe the reaction mechanisms of amine inhibition we measured the initial reaction rate at various temperatures, and these data are summarized on an Eyring plot (Figure 5-6). The large negative activation entropy indicates that the reaction proceeds via a highly ordered transition state. The activation enthalpy ($\Delta H^\ddagger = 51.9 \pm 1.3 \text{ kJ mol}^{-1}$) is about 10 kJ mol^{-1} less than that measured by Liu et al. for CdSe nanocrystal formation,^[8] which is consistent with the enhanced rate of precursor depletion in InP QD synthesis.

The amine inhibition of InP synthesis likely results from the solvation of In species during the steps that lead to the formation of TMS-MA. With an increase in the concentration of octylamine, the probability of forming complex 1 is decreased (as can be seen in the equilibrium step in Figure 5-1) and as a result the rate of $(\text{TMS})_3\text{P}$ depletion decreases.

The large negative $\Delta S^\ddagger = -126 \pm 4 \text{ J mol}^{-1} \text{ K}^{-1}$ and the large decrease in rate upon addition of amines is also consistent with solvation changes during nucleophilic substitution.^[17] The large negative entropy of activation indicates a highly ordered transition state, likely involving the arrangement of two or more species. We have proposed a potential transition state in Figure 5-1. It should be noted that a similar transition state is proposed in the synthesis of CdSe QDs, as a similarly large negative entropy of activation was reported.^[8] In addition to octylamine decreasing the probability of forming 1, the presence of octylamine may also result an increase in the activation energy of the transition state, by stabilizing the enthalpy of precursors (increasing ΔH^\ddagger), in addition, primary amines may also influence the activation entropy by hindering the formation of the highly ordered transition state, this would result in the observed decrease in the rate of $(\text{TMS})_3\text{P}$ depletion with increasing amine concentrations.

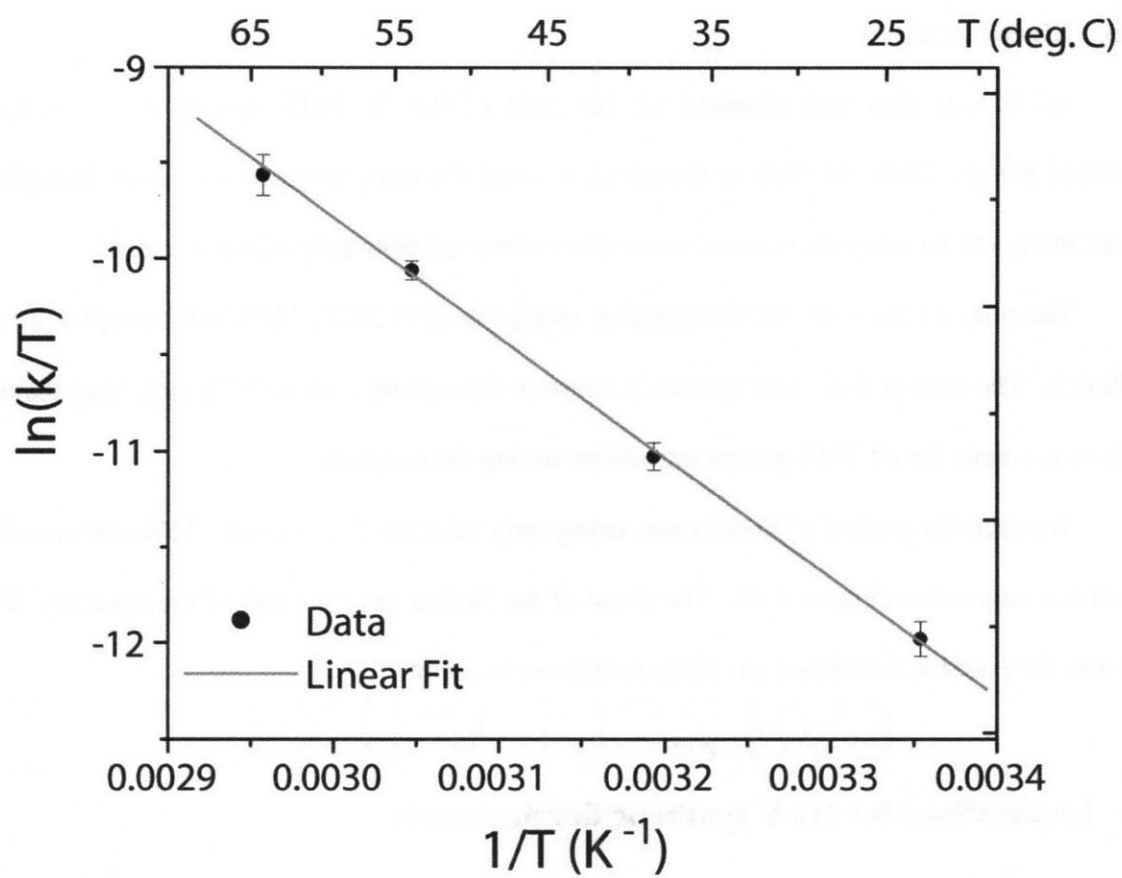


Figure 5-6. Eyring plot for amine-based synthesis of colloidal InP QDs, with $\Delta H^\ddagger = 51.9 \pm 1.3 \text{ kJ mol}^{-1}$ and $\Delta S^\ddagger = -126 \pm 4 \text{ J mol}^{-1} \text{ K}^{-1}$. Each point was taken in triplicate.

5.2.5 Kinetic Analysis

All kinetic data was obtained via integrals of the ^1H NMR spectra of the samples described above. Each spectrum in the series retained the same integration interval throughout for all times, and all integrals were referenced to an internal diphenylmethane standard.

The only identifiable TMS-containing species are $(\text{TMS})_3\text{P}$, TMS-MA, complex **2**, and TMS-OA. The sum of these four species is constant throughout (Figure 5-7), indicating that our analysis accounts for all TMS groups introduced during the reaction.

We used the method of initial rates, using early time reaction data at < 15% conversion to fit a linear regression (Figure 5-8). The slope of the fit line gave the rate of the reaction. This rate was then used to determine an experimental rate constant.

5.3 Implications for III-V synthetic developments

In conclusion, we find that currently-reported InP QD syntheses are based on non-molecular ripening processes. We have found that amines inhibit precursor decomposition. It is apparent that the challenges in the synthesis narrow size distributions of III-V QDs result from the depletion of molecular precursors following QD nucleation in current III-V QD syntheses. In order to produce InP or InAs QDs with narrow size distributions, less reactive precursors must be explored. The introduction of pnictide precursors that gradually decompose at elevated temperatures (150-300 °C) to controllably generate monomers would fulfill the criteria for a monodisperse QD synthesis (as defined in this chapter), and could potentially form InP and InAs QDs with size distributions that rival their CdSe and PbSe counterparts.

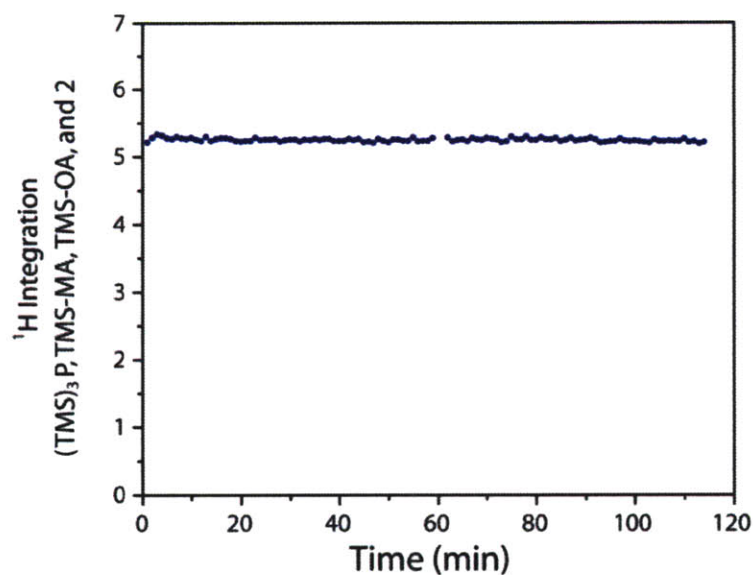


Figure 5-7. ^1H NMR integration of all identifiable TMS-containing species throughout the reaction. The overall concentration of TMS protons does not change during the course of the reaction.

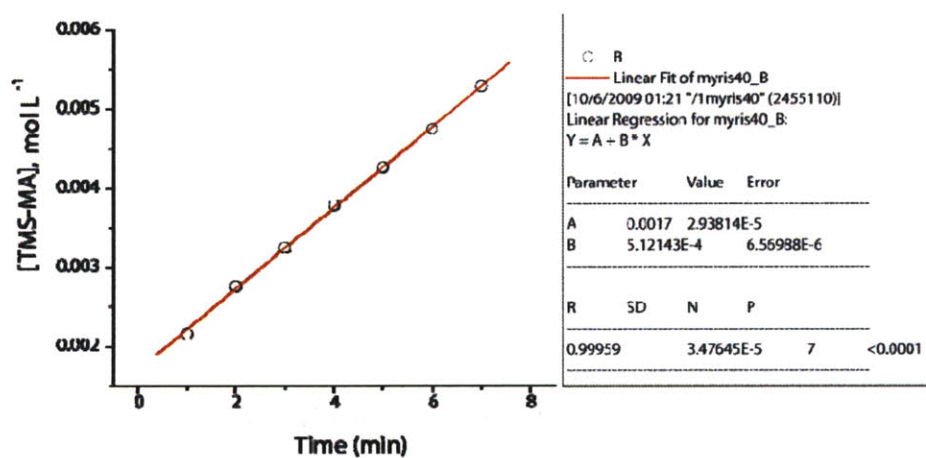


Figure 5-8. Evolution of TMS-MA concentration vs. time measured for <15% conversion as described above. This is an example of a 40 °C data set used for the Eyring analysis. At early times, the slope is the rate of reaction.

5.4 Procedures

Reagents: Octylamine (Fluka, 99%, dried over calcium hydride), Toluene d-8 (Cambridge Isotope Labs), 1,2-dichloromethane (Cambridge Isotope Labs), and diphenylmethane (Sigma, >99%, degassed) were placed into a nitrogen filled glovebox and stored over 4 Å molecular sieves prior to use. Myristic acid (Sigma, >99%), 1-octadecene (Tech grade, Sigma), hexanes (anhydrous, Acros) and Indium acetate (99.99%, Alfa Aesar) were used to synthesize Indium(III) myristate [In(MA)₃]. Trimethylsilyl chloride (Fluka, 99%, re-distilled) was used to synthesize TMS-OA and TMS-MA NMR reference compounds. Tris(trimethylsilyl) phosphine [(TMS)₃P, *caution pyrophoric*] was obtained from Strem and used as received. J-young NMR tubes (Chemglass, 600 mhz) were dried at 120 °C prior to use. All other glassware was dried at 180 °C. All samples were prepared under minimal lighting in a nitrogen filled glovebox (mBraun, <0.1 ppm oxygen).

Synthesis of In(MA)₃: The synthesis of In(MA)₃ was performed as previously reported.^[18] All solutions containing In(MA)₃ were additionally dried for two days over 4 Å molecular sieves to remove residual water.

NMR Solutions: Example of a typical solution preparation for OA:In (6 :1): Solution (A) 0.24 mmol of In(MA)₃, 1.44 mmol of OA, and 0.36 mmol of diphenylmethane were mixed to a volume of 6 ml in toluene-d₈. In(MA)₃ dissolves readily in the presence of amines. Without amines, the solution was heated to 60 °C to produce a homogeneous solution. The solutions were stored over 4 Å molecular sieves for two days prior to use. Solution (B) 0.12 mmol of (TMS)₃P and 6 ml toluene-d₈ were combined and stored in the dark at -35 °C prior to use.

NMR Reaction Tubes: In a typical reaction 0.35 ml of solution (A) and 0.35 ml of solution (B) were injected into a J-young NMR tube in the glovebox. The NMR tube was then immediately transferred for NMR measurements. All samples were handled under minimal lighting to prevent decomposition of $(\text{TMS})_3\text{P}$.

NMR Spectroscopy: All spectra were taken on 300 MHz or 500 MHz Varian INOVA NMR spectrometers using either a variable temperature broadband switchable probe or a variable temperature indirect detection probe.

Synthesis of TMS-MA: 10 mg of trimethylsilyl chloride was added to a stirred solution of 60 mg of myristic acid and 50 mg of tri-n-octylphosphine in 1 ml of toluene- d_8 and heated to 60 °C. ^1H NMR (500 mhz, toluene- d_8), δ (ppm) 0.303 (s, 9H).

Synthesis of TMS-OA: 10 mg of trimethylsilyl chloride was added to a stirred solution of 75 mg of octylamine (OA) in 1 ml of toluene- d_8 . The solution was filtered to remove the OA-HCl salt prior to ^1H NMR analysis. ^1H NMR (500 mhz, toluene- d_8), δ (ppm) 0.132 (s, 9H).

Author Contributions

This chapter is an equal contribution from Brian J. Walker (B.J.W.) and Peter M. Allen (P.M.A.). The experiments were designed and conceived by P.M.A and B.J.W. P.M.A. is responsible for the synthetic aspects of the work, and B.J.W. is responsible for NMR data collection and analysis.

5.5 References

- [1] D. Battaglia, X. Peng, *Nano Letters* 2002, 2, 1027.
- [2] R. Xie, D. Battaglia, X. Peng, *J. Am. Chem. Soc.* 2007, 129, 15432.
- [3] L. Li, P. Reiss, *J. Am. Chem. Soc.* 2008, 130, 11588.
- [4] C. B. Murray, D. J. Norris, M. G. Bawendi, *J. Am. Chem. Soc.* 1993, 115, 8706.
- [5] X. Peng, J. Wickham, A. P. Alivisatos, *J. Am. Chem. Soc.* 1998, 120, 5343.
- [6] A. A. Guzelian, J. E. B. Katari, A. V. Kadavanich, U. Banin, K. Hamad, E. Juban, A. P. Alivisatos, R. H. Wolters, C. C. Arnold, J. R. Heath, *J. Phys. Chem.* 1996, 100, 7212.
- [7] J. S. Steckel, B. K. H. Yen, D. C. Oertel, M. G. Bawendi, *J. Am. Chem. Soc.* 2006, 128, 13032.
- [8] H. Liu, J. S. Owen, A. P. Alivisatos, *J. Am. Chem. Soc.* 2007, 129, 305.
- [9] V. K. LaMer, R. H. Dinegar, *J. Am. Chem. Soc.* 1950, 72, 4847.
- [10] J. Y. Rempel, M. G. Bawendi, K. F. Jensen, *J. Am. Chem. Soc.* 2009, 131, 4479.
- [11] O. I. Micic, S. P. Ahrenkiel, A. J. Nozik, *Appl. Phys. Lett.* 2001, 78, 4022.
- [12] M. Protiere, P. Reiss, *Chem. Commun.* 2007, 2417.
- [13] S. Xu, S. Kumar, T. Nann, *J. Am. Chem. Soc.* 2006, 128, 1054.
- [14] R. Xie, Z. Li, X. Peng, *J. Am. Chem. Soc.* 2009.
- [15] R. Xie, X. Peng, *Angew. Chem.* 2008, 47, 7677.
- [16] C. Brevard, P. Granger, *Handbook of High Resolution Multinuclear NMR*, Wiley, New York, 1981.
- [17] C. Reichart, *Solvents and Solvent Effects in Organic Chemistry*, Wiley, Weinheim, 2003.

- [18] F. Wang, H. Yu, J. Li, Q. Hang, D. Zemlyanov, P. C. Gibbons, Wang, D. B. Janes, W. E. Buhro, *J. Am. Chem. Soc.* 2007, 129, 14327.

Chapter 6. Electrically Controlling and Monitoring InP Nanowire Growth

6.1 Introduction

Indium phosphide nanowires are of significant technological interest for applications ranging from single junction solar cells to high speed electronics. However, the efficient placement and integration of nanowires into devices remains a significant challenge. Here we extend the technique of electrically controlled solution-liquid-solid (EC-SLS) catalytic nanowire growth to indium phosphide. We are able to control the amount of nanowire growth by varying the bias voltage between the electrodes in solution, and to monitor nanowire bridging across the electrodes, by recording the conductivity as a function of growth time. The as-grown indium phosphide nanowires exhibit n-type conductivity as was determined by the in-situ integration of nanowires into a field effect transistor geometry. The ability to monitor nanowire growth and electrically control nanowire placement are valuable tools for fabricating nanowire devices. The EC-SLS process has the potential to aid in the fabrication of nanowire devices that could find applications in nanoelectronics, and as electrodes in solar cells and batteries.

Indium phosphide nanowires have been grown from catalyst particles using laser ablation^[1], metal organic chemical vapor deposition (MOCVD)^[2-4], and the solution-liquid-solid (SLS) process.^[5-11] In the SLS process^[5], precursors in solution are delivered to heated catalyst particles, which serve as seeds for nanowire growth (Figure 6-1). Solution phase synthesis is potentially more cost-effective than vapor phase techniques, because no expensive vacuum equipment is needed. In addition, the lower growth temperatures, typically below 300 °C,^[12] make solution phase synthesis attractive for semiconductor processes not compatible with higher temperatures.



Figure 6-1. Solution-liquid-solid synthesis of InP nanowires.

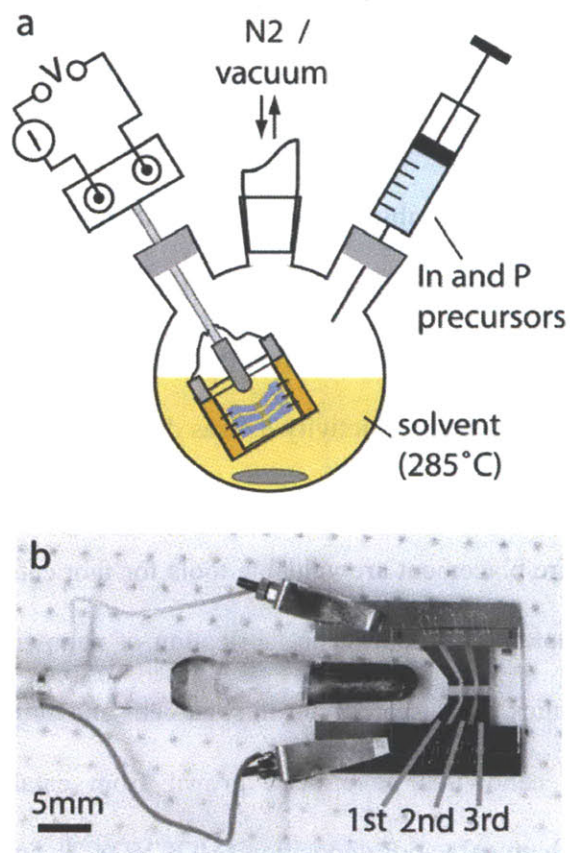


Figure 6-2. Experimental Setup. (a) Schematic of the setup used to grow InP nanowires off Bi catalyst particles on Pt electrodes in solution. The temperature of the solution was monitored with a thermocouple inserted through a fourth neck (not shown). (b) Optical image of the sample holder, scale bar: 5mm. Three interdigitated electrodes labeled 1st, 2nd, and 3rd can be biased in parallel, allowing for three separate devices to be fabricated simultaneously.

A recent report has demonstrated that CdSe nanowires can be controllably grown between two electrodes via the electrically controlled solution-liquid-solid (EC-SLS) method by varying the electrochemical potential of the catalyst seed particles.^[13] The EC-SLS method enables the simultaneous synthesis and integration of nanowires into device geometries. In this article, we extend the EC-SLS technique to the growth of InP nanowires. An important new aspect is our ability to observe nanowire bridging, *in situ*, by measuring the conductivity across the biased electrodes during nanowire growth. In addition, we demonstrate the ability to directly integrate InP nanowires into devices by growing InP nanowires in a field effect transistor geometry. Structures fabricated using the EC-SLS scheme could be applied to nanoelectronics^[1, 14, 15], light emitting diodes,^[16-18] solar cells,^[19-24] and batteries.^[25]

6.2 InP Nanowires

6.2.1 Experimental Setup

A schematic of the experimental setup used to grow InP nanowires using the EC-SLS method is shown in Figure 6-2.a. In order to make the substrate and mount resistant to the reaction conditions, only chemically inert and heat resistant materials such as glass, stainless steel, and teflon were used. An optical image of a sample can be seen in Figure 6-2.b. The samples consisted of fused silica substrates with three pairs of interdigitated electrodes composed of a 5 nm titanium adhesion layer, a 75 nm platinum layer and a 20 nm bismuth layer. The bismuth layer de-wets and forms islands with diameters of roughly 50-100 nm, that serve as catalyst particles^[13, 26]. The channel length of each electrode pair was ~55mm and the gap width was ~10 μ m (Figure 6-3.a). The sample was immersed in a tri-n-octylphosphine (TOP) solvent at a temperature of 285 °C . Next, a bias voltage was applied and a precursor solution

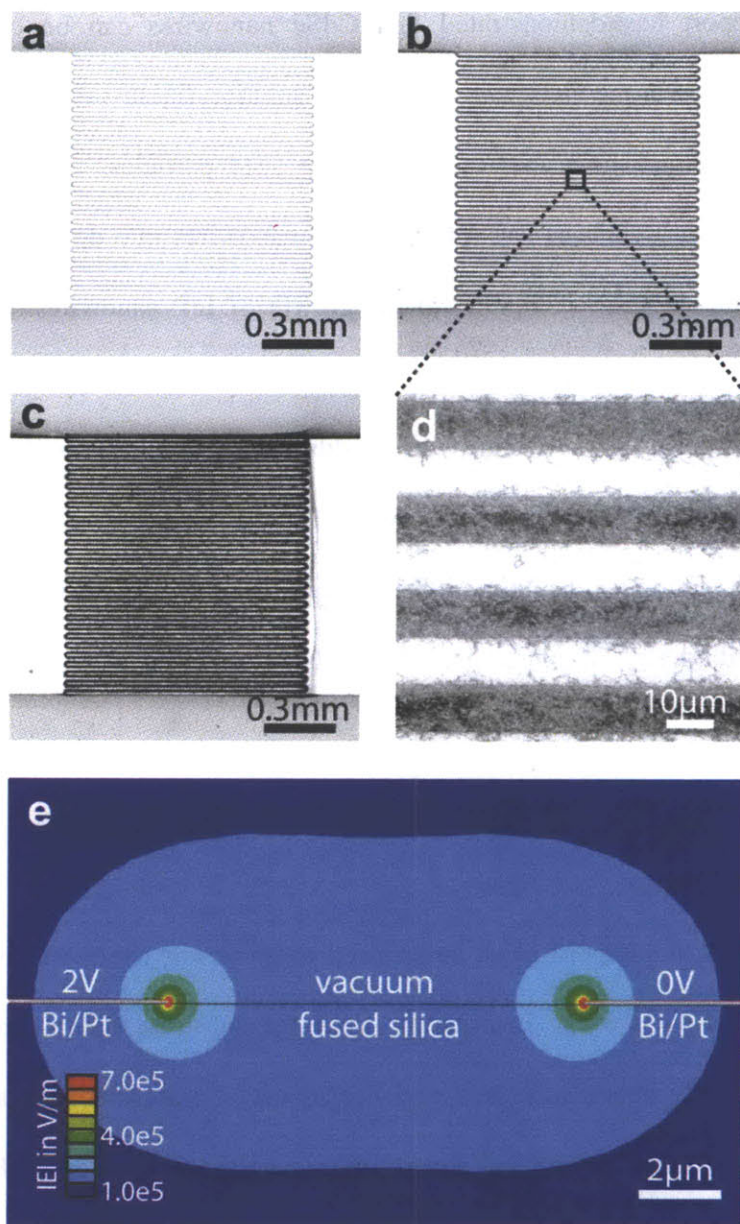


Figure 6-3. InP nanowire growth as a function of bias voltage. (a) Optical image of a pair of interdigitated electrodes without nanowires. (b) same geometry as in a) after InP nanowire growth at a bias of 0.5V, and (c) after growth at a bias of 2.0V. The scale bars in a) to (c) are 0.3mm. (d) highlighted region in (b) at higher magnification, scale bar: 10µm. (e) Schematic of the cross-section of two adjacent electrode edges (to scale), including a simulation of the absolute magnitude of the electric field at a bias of 2V, scale bar: 2µm.

containing indium(III)-iodide and tris(diethylamino) phosphine in oleyl amine was injected dropwise over the course of 3 minutes. After precursor injection, the samples were left in solution under constant temperature and bias voltage for another 2 minutes, before being withdrawn from the growth-solution.

Optical images of the interdigitated electrode geometry before and after growth at 0.5V and 2V can be seen in Figure 6-3.a-c respectively. The nanowires are almost completely confined to the gaps between the electrodes, indicating that growth emanates from the electrode edges and is guided across the gap by the electric field. The correlation between electric field strength and, hence, surface charge density on the electrode and the focusing of nanowire growth along the electrode edges is supported by the simulation of the electric field strength in Figure 6-3.e.^[27] In particular, the well known effect of electric field bunching at the edges of thin metal sheets is easily seen.^[28] As in the case of CdSe,^[13] InP nanowire growth is promoted on the low potential electrode.

6.2.2 Characterization of InP Nanowires

Characterization of the InP nanowires was carried out by scanning electron microscopy (SEM), high resolution transmission electron microscopy (HRTEM) and scanning transmission electron microscopy (STEM). An SEM image of a sample grown at a bias of 2V is shown in Figure 6-4.a. Nanowire growth is almost exclusively limited to a narrow region within 200 nm of the electrode edge, and bismuth islands showing no nanowire growth are clearly visible farther away from the electrode edge. The focusing of nanowire growth along the electrode edges correlates well with the magnitude of the electric field in the simulation (Figure 6-3.e). As can be seen in the HRTEM image in Figure 6-4.b, the nanowires tend to be polycrystalline, as could be

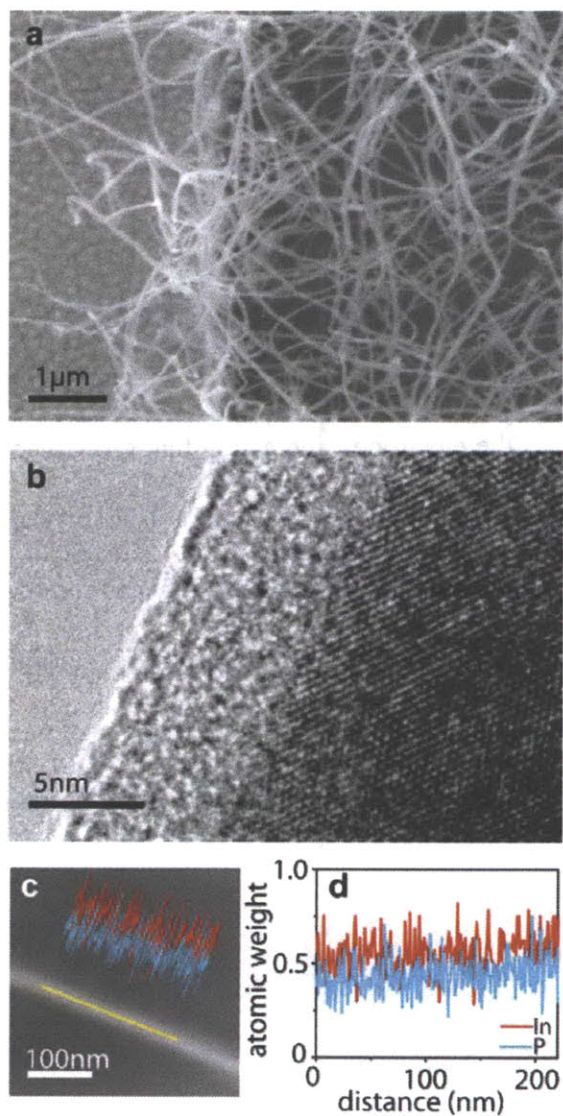


Figure 6-4. InP nanowire characterization. (a) Scanning electron microscope image of InP nanowires grown of the edge of a platinum electrode with bismuth beads on the surface, scale bar: 1 μm . (b) High resolution transmission electron microscope image of an InP nanowire, scale bar: 5 nm. (c) Scanning transmission electron microscope image of an InP nanowire used for elemental analysis, scale bar: 100 nm. (d) Relative atomic weight of indium and phosphorous as a function of position along the line highlighted in (c), obtained from energy dispersive x-ray spectroscopy.

expected from the frequent changes in wire-shape and direction seen in Figure 6-4.a. This behavior could be related to the zinc-blende crystal structure of InP and the twinning behavior observed in MOCVD grown InP nanowires by Woo et al.^[29] In contrast, CdSe nanowires grown by the EC-SLS technique show a high degree of crystallinity owing to their preferred growth direction along the (001) axis of the wurtzite crystal lattice.^[13] We attribute the approximately 5nm thick amorphous outer layer to the formation of a native oxide layer. Figure 6-4.c highlights the line-scan along the wire used for elemental analysis by STEM shown in Figure 6-4.d. The higher average atomic percentage of indium, 56%, relative to phosphorous, 44%, can be attributed to the indium rich native oxide layer typically observed on InP^[30].

6.2.3 Monitoring of InP Nanowire Growth

The current across three electrode pairs, connected in parallel, during the growth of InP nanowires at a constant bias of 1V is plotted in Figure 6-5. The pure TOP solution is relatively insulating with a conductivity below 3 μ S. Drop-wise injection of the indium and phosphorus precursors begins at 100s and the growth-solution maintains its low initial conductivity until the current begins to rapidly increase at ~200s. The rapid increase in current slows down at ~260s and precursor injection is completed at 280s. The current then shows a slow linear increase over the period from 280s to 400s, while the sample remains in solution under constant bias. When the sample is withdrawn from the solution around 400s the current shows a sharp decrease.

We interpret the rapid increase in current at ~200s as the onset of InP nanowires bridging the electrode gap. If the increase in current were solely due to an increase in conductivity of the growth solution as the indium and phosphorous precursors are added, the current increase could be expected to set in immediately after precursor injection begins around 100s. We also

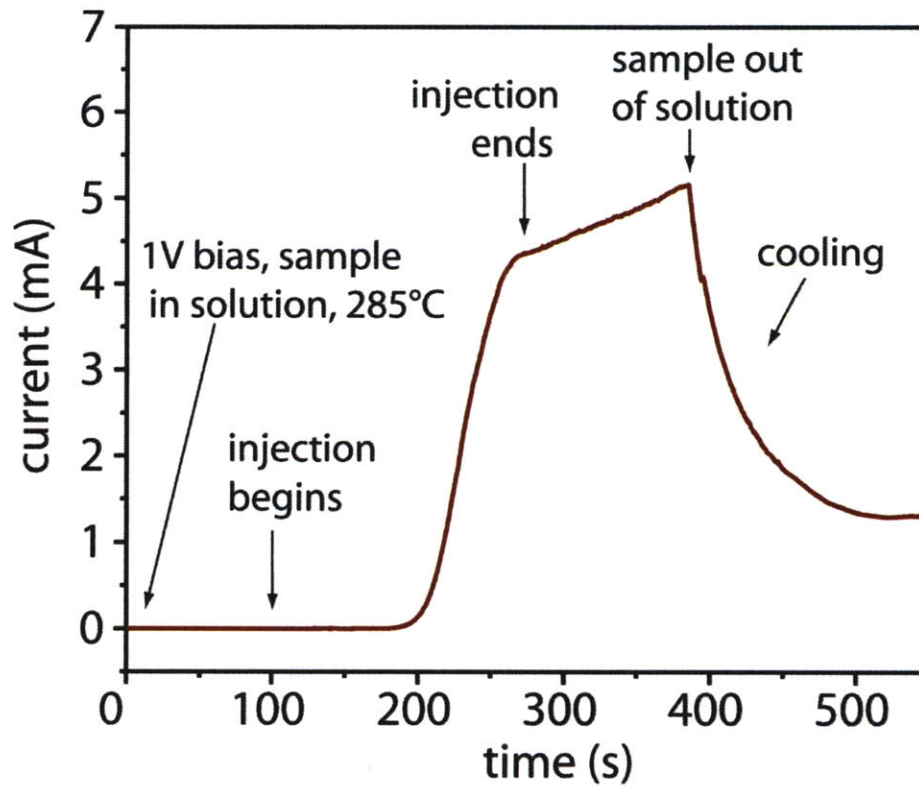


Figure 6-5. Current sensing across the electrode gap during the InP nanowire growth process as a function of time and at a constant bias of 1V.

measured the conductivity of the indium and phosphorous precursors by only injecting one of the two precursors under otherwise identical synthesis conditions. In both cases the conductivity remained below $3\mu\text{S}$ during the entire run, more than a factor of 1,000 below the peak conductivity value in Figure 6-5. This indicates that the observed increase in current at $\sim 200\text{s}$ results from InP nanowires bridging the electrode gap. We interpret the nearly 100s delay between the beginning of precursor injection and the rapid increase in current as the time it takes the InP nanowires to grow across the $10\ \mu\text{m}$ wide electrode gap. The slow increase in current after precursor injection ends at 280s could be due to additional bridging events resulting from wire growth from residual precursors in solution. However, chemical effects related to doping or better contact formation at the nanowire/electrode interface could also be responsible for the increase in current. The sharp decrease in current when the sample is withdrawn from the growth solution at 400s can be attributed to a decrease in the number of thermally activated charge carriers as the sample cools. This suggests that monitoring the conductivity during the EC-SLS growth process may serve as a useful tool for assessing *in situ* device formation.

The conductivity at 5V of a series of devices grown at different bias voltages is plotted in Figure 6-6. The measurements were taken in a probe station under ambient conditions after removing the samples from solution and rinsing them with hexanes. When both electrodes were grounded during growth, only a small amount of wire growth resulting in a relatively low conductivity was observed. As in the case of CdSe, InP wire growth is inhibited at zero bias when the bismuth catalyst particles are in contact with the platinum electrodes. This is probably due to electron depletion of the bismuth particles by the platinum substrate resulting from the difference in work function between the two metals.^[31] Applying a voltage reverses this effect on

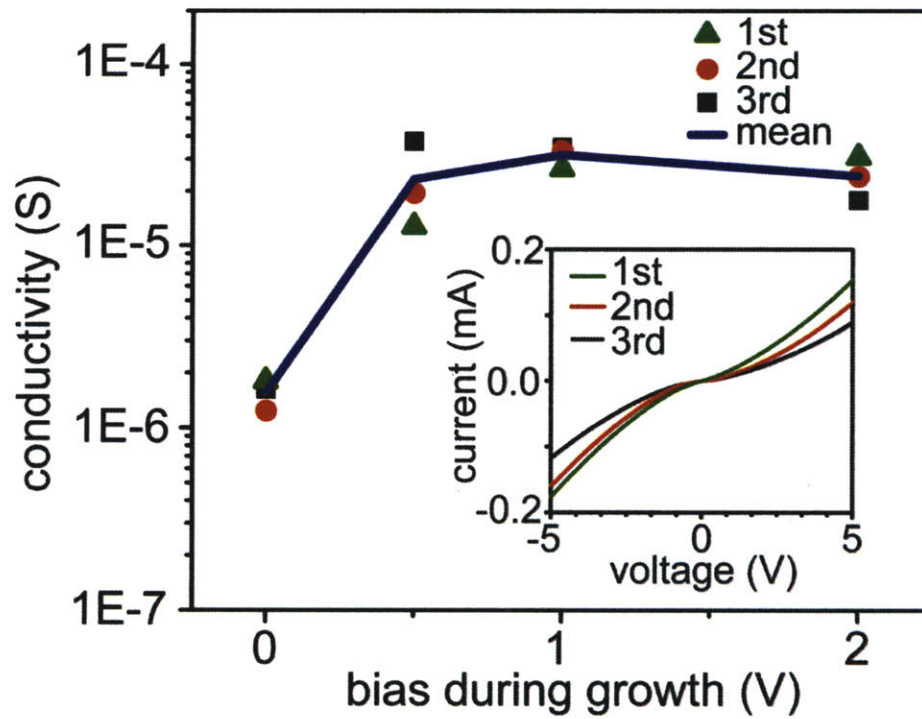


Figure 6-6. Conductivity as a function of bias voltage during growth. The conductivity, measured at a bias of 5V, for three devices fabricated in parallel under the same conditions is plotted as a function of growth voltage. The inset shows the I/V-curves of three devices grown in parallel at a bias of 2V.

the low potential electrode by inducing a negative surface charge and hence compensating for electron depletion by the platinum substrate. However, chemical effects on the platinum surface or at the solution-catalyst interface could also play an important role. The small amount of InP nanowire growth, even at zero bias, could be related to the titanium adhesion layer that is exposed at the electrode edges. When a growth bias of 0.5V is applied, the average device conductivity increases by over an order of magnitude to about $2 \cdot 10^{-5}$ S and a similar conductivity is observed for devices grown at 1V and 2V. The saturation in conductivity as a function of growth voltages is surprising since there is a clear increase in wire material as a function of growth voltage as can be seen in Figure 6-3.a-c. An explanation could be that the number of active catalyst seed particles at the electrode edges is similar for different growth voltages. The difference in overall wire material would then arise from an increase in wire length as a function of growth voltage, with a similar number of bridging nanowires largely independent of growth voltage. However, processes at the nanowire-electrode contacts and more complex electrochemical effects may also be involved. The inset in Figure 6-6 shows the IV-curves of three devices grown in parallel at 2V. The conductivity suppression around zero bias is typical for Schottky barrier formation in metal-semiconductor-metal contacts.

6.2.4 Field Effect Transistors

In order to determine the majority charge carrier type, we grew InP nanowire mats in a field effect transistor using the EC-SLS technique (Figure 6-7.a). Nanowire growth was carried out with one electrode grounded and the counter electrode and doped silicon back gate held at +0.5V in order to promote nanowire growth along the substrate surface. An SEM image of InP nanowires grown in transistor geometry is shown in Figure 6-7.b. Current traces as a function of

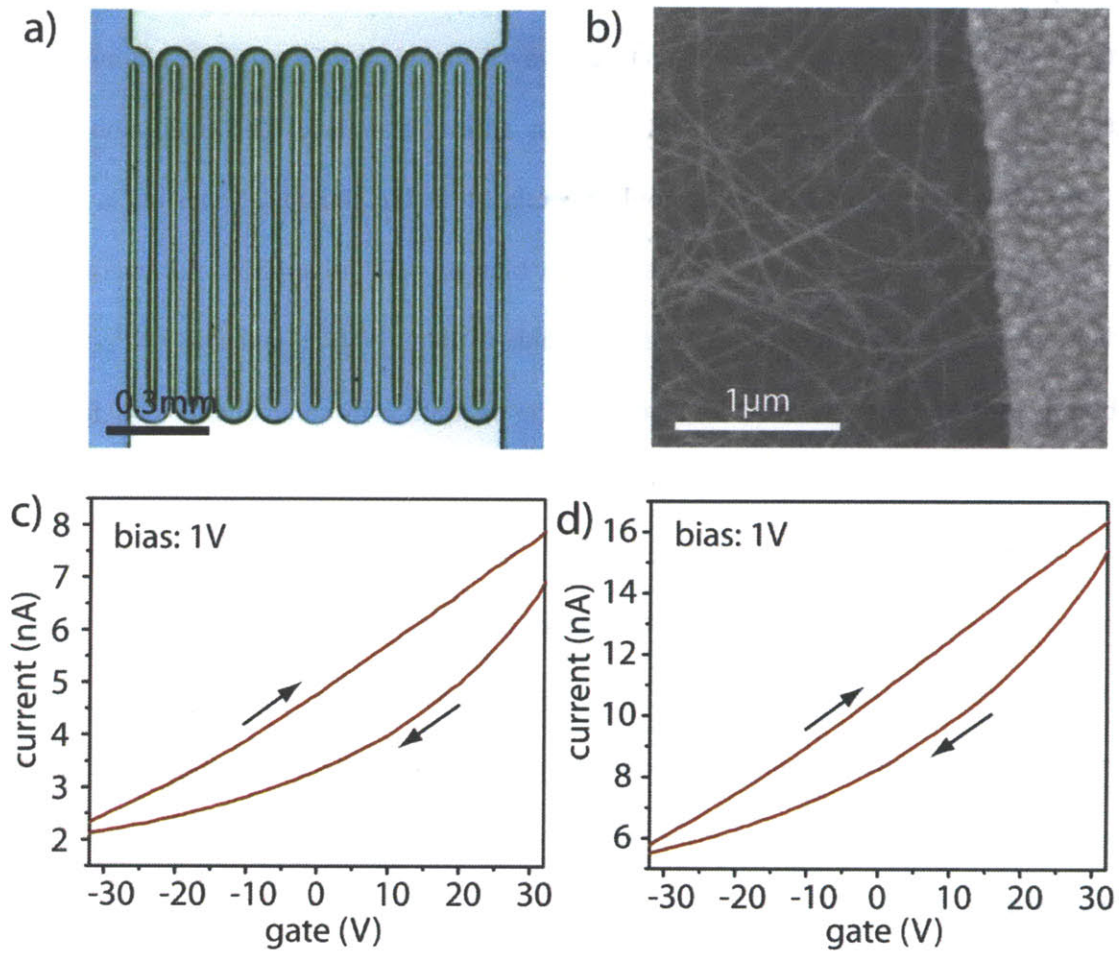


Figure 6-7. InP nanowire mats grown in a field effect transistor geometry. (a) Optical image of the InP nanowire field effect transistor device. (b) Scanning electron microscope image of a region of the device shown in (a). (c-d) Current as a function of back gate voltage at a constant electrode bias of 1V for two devices.

back gate voltage, at a constant bias of 1V, are shown for two devices in Figure 6-7.c-d. The observed hysteretic behavior may be related to trapping of charge carriers by the native oxide layer. The gating characteristics of both devices indicate that the majority charge carriers in our EC-SLS grown InP nanowire mats are n-type.

6.3 Conclusions

In conclusion, we have demonstrated the electrically controlled solution-liquid-solid (EC-SLS) process for InP nanowires. A particularly attractive feature is our ability to monitor the bridging of nanowires across the electrode gap during the growth process, by simultaneously measuring the conductivity. Nanowire growth by the EC-SLS process has been shown to be a versatile and general process and could facilitate the direct integration of a wide variety of solution processed nanowires^[32] and oriented nanowire heterostructures^[26] into functional device geometries.

6.4 Procedures

The experimental setup is shown in Figure 6-2, additional details can be found in Ref. 13.

Sample preparation: Interdigitated electrodes (5 nm titanium adhesion layer, 75 nm platinum layer, 20 nm bismuth catalyst layer, thermally evaporated) with a channel length of about 55 mm and a width of about 10 μ m were defined on fused silica substrates (12.5mmx12.5mmx0.5mm, MTI Corp.) by optical lithography. Samples used for the field effect transistor geometry consisted of interdigitated electrodes with a channel width of 50 μ m on degenerately doped silicon substrates with a 300 nm layer of insulating thermal oxide. As before, the electrodes consisted of a 5 nm Ti layer, a 75 nm Pt layer and a 20 nm Bi layer.

Synthesis: A four neck reaction flask was filled with 45ml of tri-n-octylphosphine (Strem, 97%) under air-free conditions and heated to 285 °C. A stock solution of 0.25M InI₃ (Alfa Aesar, 99.999%) in oleyl amine (Acros Organics, previously degassed under vacuum at 120 °C for 2h) was prepared under nitrogen atmosphere. 2ml of the 0.25M InI₃ stock solution were then added to 500mg of tris(diethylamino)phosphine (Alfa Aesar). The resulting precursor solution was injected dropwise over the course of three minutes into the reaction flask containing the biased electrodes immersed in TOP at 285 °C.

Author Contributions

This chapter is an equal contribution between August Dorn (A.D.) and Peter M. Allen (P.M.A.). A.D. is responsible for the fabrication and electrical measurements involving the EC-SLS devices. P.M.A. is responsible for the synthetic aspects of this work.

6.5 References

- [1] X. F. Duan, Y. Huang, Y. Cui, J. F. Wang, C. M. Lieber, *Nature* **2001**, *409*, 66.
- [2] S. Bhunia, T. Kawamura, Y. Watanabe, S. Fujikawa, K. Tokushima, *Applied Physics Letters* **2003**, *83*, 3371.
- [3] S. Bhunia, T. Kawamura, S. Fujikawa, K. Tokushima, Y. Watanabe, *Physica E-Low-Dimensional Systems & Nanostructures* **2004**, *21*, 583.
- [4] M. T. Borgstrom, E. Norberg, P. Wickert, H. A. Nilsson, J. Tragardh, K. A. Dick, G. Statkute, P. Ramvall, K. Deppert, L. Samuelson, *Nanotechnology* **2008**, *19*.
- [5] T. J. Trentler, K. M. Hickman, S. C. Goel, A. M. Viano, P. C. Gibbons, W. E. Buhro, *Science* **1995**, *270*, 1791.
- [6] T. J. Trentler, S. C. Goel, K. M. Hickman, A. M. Viano, M. Y. Chiang, A. M. Beatty, P. C. Gibbons, W. E. Buhro, *Journal of the American Chemical Society* **1997**, *119*, 2172.
- [7] J. F. Wang, M. S. Gudiksen, X. F. Duan, Y. Cui, C. M. Lieber, *Science* **2001**, *293*, 1455.
- [8] D. D. Fanfair, B. A. Korgel, *Crystal Growth & Design* **2005**, *5*, 1971.
- [9] F. Wang, H. Yu, J. Li, Q. Hang, D. Zemlyanov, P. C. Gibbons, L. W. Wang, D. B. Janes, W. E. Buhro, *Journal of the American Chemical Society* **2007**, *129*, 14327.
- [10] T. Strupeit, C. Klinke, A. Kornowski, H. Weller, *Acs Nano* **2009**, *3*, 668.
- [11] Z. P. Liu, K. Sun, W. B. Jian, D. Xu, Y. F. Lin, J. Y. Fang, *Chemistry-a European Journal* **2009**, *15*, 4546.
- [12] W. E. Buhro, K. M. Hickman, T. J. Trentler, *Advanced Materials* **1996**, *8*, 685.
- [13] A. Dorn, C. R. Wong, M. G. Bawendi, *Advanced Materials* **2009**, *21*.

- [14] S. De Franceschi, J. A. van Dam, E. Bakkers, L. F. Feiner, L. Gurevich, L. P. Kouwenhoven, *Applied Physics Letters* **2003**, *83*, 344.
- [15] Y. J. Doh, S. De Franceschi, E. Bakkers, L. P. Kouwenhoven, *Nano Letters* **2008**, *8*, 4098.
- [16] M. S. Gudiksen, L. J. Lauhon, J. Wang, D. C. Smith, C. M. Lieber, *Nature* **2002**, *415*, 617.
- [17] E. D. Minot, F. Kelkensberg, M. van Kouwen, J. A. van Dam, L. P. Kouwenhoven, V. Zwiller, M. T. Borgstrom, O. Wunnicke, M. A. Verheijen, E. Bakkers, *Nano Letters* **2007**, *7*, 367.
- [18] V. Zwiller, N. Akopian, M. van Weert, M. van Kouwen, U. Perinetti, L. Kouwenhoven, R. Algra, J. G. Rivas, E. Bakkers, G. Patriarche, L. Liu, J. C. Harmand, Y. Kobayashi, J. Motohisa, *Comptes Rendus Physique* **2008**, *9*, 804.
- [19] A. Heller, R. G. Vadimsky, *Physical Review Letters* **1981**, *46*, 1153.
- [20] K. P. Jayadevan, T. Y. Tseng, *Journal of Nanoscience and Nanotechnology* **2005**, *5*, 1768.
- [21] C. J. Novotny, E. T. Yu, P. K. L. Yu, *Nano Letters* **2008**, *8*, 775.
- [22] O. L. Muskens, J. G. Rivas, R. E. Algra, E. Bakkers, A. Lagendijk, *Nano Letters* **2008**, *8*, 2638.
- [23] J. Kupec, B. Witzigmann, *Optics Express* **2009**, *17*, 10399.
- [24] H. Goto, K. Nosaki, K. Tomioka, S. Hara, K. Hiruma, J. Motohisa, T. Fukui, *Applied Physics Express* **2009**, *2*.
- [25] M. Kishore, U. V. Varadaraju, *Journal of Power Sources* **2006**, *156*, 594.
- [26] L. Ouyang, K. N. Maher, C. L. Yu, J. McCarty, H. Park, *Journal of the American Chemical Society* **2007**, *129*, 133.
- [27] *Maxwell®*, 2D electromagnetic field simulator, Ansoft LLC, Pittsburgh, PA, **2005**.
- [28] J. D. Jackson, *Classical Electrodynamics*, John Wiley and Sons, **1975**.
- [29] R. L. Woo, R. Xiao, Y. Kobayashi, L. Gao, N. Goel, M. K. Hudait, T. E. Mallouk, R. F. Hicks, *Nano Letters* **2008**, *8*, 4664.
- [30] N. Shibata, H. Ikoma, *Japanese Journal of Applied Physics Part 1-Regular Papers Short Notes & Review Papers* **1992**, *31*, 3976.

- [31] M. T. Paffett, C. T. Campbell, T. N. Taylor, *Journal of Chemical Physics* **1986**, *85*, 6176.
- [32] M. Kuno, *Physical Chemistry Chemical Physics* **2008**, *10*, 620.

Acknowledgements

This thesis is the result of inspiration and input from colleagues, scientific collaborations, and the support of family and friends. I am grateful for all of the opportunities I have been given that have led to the production of a somewhat intelligible body of work.

My introduction to research began at UC Santa Barbara in Professor Alison Butler's lab. Without Alison's enthusiasm for science and her tremendous support, I would never have made it to MIT. While at Santa Barbara, I also had the pleasure of spending many afternoons talking about science and life with Professor Peter Ford. He has always been my inspiration to one day (maybe) apply to be a professor myself. My introduction to inorganic materials chemistry occurred in the lab of Professor Ram Seshadri my final year at Santa Barbara, and this research experience played a major role in my decision to have Mounji Bawendi as my Ph.D. advisor.

I would truly like to thank my research advisor, Mounji, for providing an excellent environment for carrying out research. Mounji has always encouraged me to pursue my personal research interests, which has made graduate school an immensely rewarding intellectual experience. Mounji has kept his office door open for discussions ranging from scientific musings to meticulous paper revisions. His way of quietly demanding only the highest caliber research has shaped me as an independent and critical scientist.

The Bawendi lab has been a welcoming and open environment, and I credit this environment as one of the primary reasons that graduate school has been both enjoyable and productive. I have had the pleasure of collaborating with many scientists from different backgrounds ranging from physical chemistry, physics, to engineering and materials science. This unique composition created an environment where we understood what significant scientific questions to ask.

My office mates have made coming into the basement of building 18 bearable even in the coldest of winter months. I have been sitting next to Hee-Sun Han for my entire PhD, and she has always had a smile on her face! I have immense respect for her drive and depth of understanding in physical chemistry. Brian Walker has been a friend and collaborator since our first day at MIT, and we have long joked about how fun it would be to one day be 'professor buddies.' Dr. Jongnam Park has reminded me how carefree graduate school is when compared to the real world, and this wisdom has improved my outlook while in graduate school. August Dorn re-introduced me to the sport of tennis after a several year hiatus, as well as introduced me to the world of semiconductor nanowires. Numpon Insin has been a fellow Inorganic chemist, and his way of quietly working has reminded me to have patience and be calm. During my third year I finally discovered the downtown Boston nightlife with Wenhao Liu, and I think we could write a Nature Protocols on how to live the high life in Boston for less than \$20 a night. I wish Wen the best as he starts a new career with QDVision, I am sure we will be seeing QDs powering the planet before too long.

All of the Bawendi lab members have been a big part of my time at MIT. It has taken me the entirety of my PhD to fully grasp Gautham Nair's uncompromising approach to science, and he has challenged me to be a more rigorous scientist. Outside of the lab, Gautham and I explored the world of power lifting and peak blasting. Andrew Greytak has always been eager to discuss

QD synthesis, and has been a breath of fresh air when others have overlooked the significance of synthesis in our field. Lisa Marshall spent some patient afternoons with me trying to look at single QDs. In the world of 'charge transport' Scott Geyer and Liang-yi Chang have been very influential in my understanding of things such as photovoltaics and photo detectors. I have also had the privilege to collaborate with them making QD devices, and they are responsible for greatly broadening my interests and knowledge in all the great things that can be accomplished with semiconductor devices.

The lab has recently grown with a new generation of young scientists, and I hope that they will take advantage of the freedom and opportunities of the Bawendi lab to embark on exciting new research projects. Daniel Harris is taking on the next generation of quantum dot synthetic projects, and I hope to see him have a productive time at MIT.

I would never have managed to make it here without the love and support of my parents, who have always put family first, and this body of work is for them.

PETER M. ALLEN

PERSONAL

Born on July 14, 1984 in Upland, California.

EDUCATION

4/2010 Ph.D. Inorganic Chemistry, Massachusetts Institute of Technology

6/2006 B.S. Chemistry, University of California Santa Barbara (Highest Honors)

PROFESSIONAL AFFILIATIONS

American Chemical Society, Materials Research Society.

AWARDS

Morse Travel Grant (2009), Materials Research Society Graduate Student Award (2008), Merck Index Award (2006), Princeton Environmental Institute Undergraduate Fellow (2004), Ralph Kilb Undergraduate Fellow (2003).

PRESENTATIONS

Allen PM, Walker BJ, and Bawendi MG. ACS Spring **2010**, San Francisco, CA.
“Mechanistic Insights into the Formation of InP Quantum Dots”

Allen PM, Liu W, and Bawendi MG. ACS Fall **2009**, Washington D.C.
“InAs(ZnCdS) Quantum Dots Optimized for Biological Imaging in the Near-Infrared”

Allen PM, Liu W, and Bawendi MG. MRS Fall **2009**, Boston, MA.
“InAs(ZnCdS) Quantum Dots Optimized for Biological Imaging in the Near-Infrared”

Allen PM, Nair G, and Bawendi MG. MRS Fall **2008**, Boston, MA. (Award Symposium)
“Ternary I-III-VI Quantum Dots Luminescent in the Red to Near Infrared”

PATENTS

Allen PM, Liu W, and Bawendi MG. **2009**, Provisional Patent Submitted.
“Materials and Methods for Biological Imaging”

Liu W, Allen PM, Insin N, and Bawendi MG. **2009**, Provisional Patent Submitted.
“Co-polymer Associated Nanomaterials”

Allen PM and Bawendi MG. **2009**, PCT/US2009/000406.
“Semiconductor Nanocrystals”

PUBLICATIONS

Allen PM, Liu W, Chauhan VP, Lee J, Ting AY, Fukumura D, Jain RK, and Bawendi MG. *Journal of the American Chemical Society*, **2010**, 132, 470-471.

“InAs(ZnCdS) Quantum Dots Optimized for Biological Imaging in the Near-Infrared”

Allen PM, Walker BJ, and Bawendi MG. *Angewandte Chemie*, **2010**, 49, 760-762. (Equal Authorship)

“Mechanistic Insights into the Formation of InP Quantum Dots”

Dorn A, Allen PM, and Bawendi MG. *ACS Nano*, **2009**, 3, 3260-3265. (Equal Authorship)

“Electrically Controlling and Monitoring InP Nanowire Growth from Solution”

Allen PM and Bawendi MG. *Journal of the American Chemical Society*, **2008**, 130, 9240-9241.

“Ternary I-III-VI Quantum Dots Luminescent in the Red to Near-Infrared”